

Nat.Lab. Unclassified report 000/99

*Date of issue: 10/02*

## **The integration of an optical and a thermal model for applications in optical recording**

J.H. Brusche

**Company Confidential till 200210**

© Philips Electronics Nederland BV 2002

Authors' address data: J.H. Brusche WY08; brusche@natlab.research.philips.com

©Philips Electronics Nederland BV 2002  
All rights are reserved. Reproduction in whole or in part is  
prohibited without the written consent of the copyright owner.

---

**Unclassified report:** 000/99

**Title:** The integration of an optical and a thermal model for applications in optical recording

**Author(s):** J.H. Brusche

---

**Part of project:** Speed race CD/DVD R/RW

**Customer:** Erwin Meinders

---

**Keywords:** phase-change recording, dye recording, diffraction, polarization, Cyclop, heat diffusion, finite element method.

**Abstract:** We consider optical disks consisting of several stacked layers, one of which is a recording layer which consists of a dye (for write once disks) or a phase-change material (for rewritable disks). Due to the illumination by a laser spot the temperature increases locally in the disk. The pulsing laser spot writes marks in the recording layer that represent the digitally encoded data. To guide the laser spot, the structure of the disks is grooved. Due to these grooves, the incident light of the spot is scattered.

With the existing finite element program Cyclop, electromagnetic diffraction problems in two-dimensional periodic structures can be solved rigorously for three-dimensional incident fields, such as the laser spot used in optical recording.

A three-dimensional finite element method code exists in Philips Research to simulate the heat diffusion during the recording. The optical and thermal models and codes are integrated for a more accurate simulation of the recording process.

The integration of the models has been tested on a planar geometry. Finally, thermal simulations are run for stationary and moving predominantly TE- and TM-polarized spots that are focused on the center groove of a Blu-ray disk.

---

**Conclusions:** With the integration of the optical and the thermal model a tool has been developed with which several phenomena, such as polarization effects and the influence of changing the geometry and properties of the stack, can be simulated accurately. The results of such simulations will give insight in the optimization of groove geometry, stack design and the effects of for instance optical and thermal cross-track cross talk.



# Contents

<b>1</b>	<b>Introduction</b>	<b>3</b>
1.1	Brief history of optical recording . . . . .	3
1.2	Dye and Phase-change recording . . . . .	4
1.3	Motivation for this research project . . . . .	5
1.4	Objective of this research project . . . . .	7
1.5	Acknowledgements . . . . .	7
1.6	About this report . . . . .	8
<b>2</b>	<b>The heat diffusion model</b>	<b>9</b>
2.1	Current model . . . . .	9
2.2	Solving the heat diffusion equation by using Sepran . . . . .	10
2.3	Integration of the thermal model with Cyclop . . . . .	11
<b>3</b>	<b>Overview of the optical model</b>	<b>12</b>
3.1	Optical reading and writing . . . . .	12
3.2	Illumination of the disk . . . . .	13
3.3	Diffraction gratings . . . . .	14
<b>4</b>	<b>Maxwell's equations</b>	<b>15</b>
4.1	Maxwell's equations in free space . . . . .	15
4.2	Energy conservation and the Poynting vector . . . . .	16
4.3	Maxwell's equations in matter . . . . .	18
4.4	Absorption and time-average energy density . . . . .	20
<b>5</b>	<b>The incident field</b>	<b>21</b>
5.1	Plane waves and the electromagnetic field . . . . .	21
5.2	Expansion into plane waves . . . . .	23
5.3	Polarization and the Fresnel coefficients . . . . .	24
5.4	Focusing of a beam by a lens . . . . .	28
5.5	The power of the laser beam . . . . .	30
<b>6</b>	<b>Diffraction at periodic gratings</b>	<b>31</b>
6.1	Derivation of the grating problem in a unit cell . . . . .	31

6.2	Derivation of the boundary conditions for the unit cell . . . . .	34
6.3	TE- and TM-polarization . . . . .	37
6.4	Uniqueness of the solution of the boundary value problem . . . . .	38
6.5	Variational formulation and the FEM . . . . .	39
6.6	Incoming focused spot . . . . .	41
6.7	Sampling of the incident spot . . . . .	43
<b>7</b>	<b>The Cyclop program</b>	<b>45</b>
7.1	The Cyclop preprocessing . . . . .	45
7.1.1	Bicycle and the general Cyclop input file . . . . .	45
7.1.2	Additional Cyclop input files . . . . .	47
7.2	The main structure of Cyclop . . . . .	47
7.2.1	Initialization . . . . .	47
7.2.2	The main loop . . . . .	48
7.2.3	Postprocessing . . . . .	49
7.3	Calculation of an analytical solution . . . . .	49
<b>8</b>	<b>Extension of the Cyclop program</b>	<b>50</b>
8.1	Extension from the 2d-unit cell to a 3d-region . . . . .	50
8.2	The implementation of the extension in Cyclop . . . . .	51
8.2.1	Modification of the initialization . . . . .	51
8.2.2	The modified main loop . . . . .	51
8.2.3	Modification of the postprocessing . . . . .	53
8.3	Additional modifications to Bicycle and Cyclop . . . . .	54
<b>9</b>	<b>Integration of the Cyclop output into the heat diffusion model</b>	<b>55</b>
9.1	Cycpost: the Cyclop postprocessor . . . . .	55
9.2	Mapping of the extended Cyclop output to the heat diffusion mesh . . . . .	56
9.3	Integration of the mapped data in the thermal model . . . . .	58
9.4	An alternative for Bicycle . . . . .	59
9.5	Problems encountered . . . . .	60
<b>10</b>	<b>Numerical simulations</b>	<b>61</b>
10.1	Accuracy of the Cyclop solution . . . . .	61
10.2	The extension of the Cyclop data . . . . .	63
10.3	Validation of the integrated thermal model . . . . .	70
10.4	Stationary spots for a BD-disk recording stack . . . . .	79
10.5	Moving spots for a BD-stack . . . . .	89
<b>11</b>	<b>Conclusions and recommendations</b>	<b>96</b>
	References . . . . .	98

## **Distribution**



# Glossary of notation and symbols

Throughout this report, the symbols printed in *italic* are scalars and symbols in **bold** are vectors. When a symbol is printed calligraphic (for example  $\mathcal{U}$  or  $\mathcal{U}$ ), it is not only a function of the spatial coordinate  $\mathbf{r}$  but also of the time  $t$ .

The following list contains the physical constants that are used in this report.

symbol	description	value
$\epsilon_0$	electric permittivity of vacuum	$8.854 \times 10^{-12} C^2/Nm^2$
$\mu_0$	magnetic permeability of vacuum	$4\pi \times 10^{-7} Wb/Am$

The following list contains the most important symbols that are used in this report.

symbol	description	unit
$\delta$	focal depth	$m$
$\Delta$	thickness of recording stack	$m$
$\Delta c$	distance between successive clusters	$m$
$\Delta k_x, \Delta k_y$	grid distances in reciprocal space	$m$
$\Delta x, \Delta y$	grid distances in ordinary space	$m$
$\epsilon$	relative permittivity	-
$\kappa$	heat conductivity	$W/m/^\circ C$
$\lambda$	wavelength	$m^{-1}$
$\rho$	density	$kg/m^3$
$\rho$	charge density	$C/m^3$
$\rho C_p$	heat capacity	$J/m/^\circ C$
$\chi$	electric susceptibility	-
$\omega$	frequency	$rad/s$
$\Omega$	unit cell	-
$C_p$	specific heat	$J/kg/^\circ C$
$D$	diameter of focused spot	$m$
$\mathcal{E}$	electric field (real)	$V/m$
$\mathbf{E}$	electric field (complex)	$V/m$
$\mathbf{E}^i$	incident electric field	$V/m$
$\mathbf{E}^s$	scattered electric field	$V/m$
$\mathcal{H}$	magnetic field (real)	$A/m$
$\mathbf{H}$	magnetic field (complex)	$A/m$
$\mathbf{H}^i$	incident magnetic field	$A/m$
$\mathbf{H}^s$	scattered magnetic field	$A/m$
$I$	intensity factor	-

symbol	description	unit
$\mathcal{J}$	current density (real)	$A/m^2$
$\mathbf{J}$	current density (complex)	$A/m^2$
$k$	wave number	-
$\mathbf{k}$	wave vector	$rad/m$
$K$	number of grid points used in FFT in period $p$	-
$L_{tx}, L_{ty}, L_{tz}$	dimensions of thermal computational box	$m$
$n$	index of refraction	-
NA	numerical aperture	-
$n_c$	cluster index	-
$N_c$	total number of clusters	-
$n_p$	period index	-
$N_p$	total number of periods	-
$N_x, N_y$	number of grid points used in FFT in $x$ -, $y$ -direction	-
$p$	grating period	$m$
$P$	total power of laser spot	$W$
$\mathbf{P}$	electric polarization	$C/m^2$
$\mathcal{S}$	Poynting vector (real)	$J/sm^2$
$\mathbf{S}$	Poynting vector (complex)	$J/sm^2$
$Q$	heat source	$V/m^3$
$t$	time	$s$
$T$	temperature	$^{\circ}C$
$v$	velocity	$m/s$
$w$	total energy density	$J/m^3$
$w_e$	electric energy density	$J/m^3$
$w_m$	magnetic energy density	$J/m^3$
$W$	absorbed energy	$W/m^3$
$x_c, y_c, z_c$	Cyclop coordinates of a thermal nodal point	-

# Chapter 1

## Introduction

This report is the result of my graduation project at Philips Research Laboratories, Eindhoven. The graduation project is part of the curriculum of Technical Mathematics at Delft University of Technology (TUD) and has been supervised by prof. dr. Urbach (Philips), dr. ir. Meinders (Philips) and ir. Segal (TUD).

### 1.1 Brief history of optical recording

The use of (digital) optical recording started in 1982 with the introduction of the compact disk system (CD). This read-only medium, with a storage capacity of 650MB (Megabytes), became widely accepted and appreciated due to its replicability and durability. Besides as a medium for recorded music the compact disk can be used to store computer data: the compact disk read-only memory or CD-ROM (introduced in 1985).

The digitally encoded information on a CD or CD-ROM is contained on a disk with a diameter of 12 cm in the form of a relief structure, consisting of pits and non-pits with varying length, along a spiralling track. The pits and non-pits can be interpreted as a binary code of zeros and ones. The substrate disk is coated with a metallic mirror and a protective layer. The metallic mirror layer allows the information to be read by detecting intensity differences in the reflected light, caused by the diffraction on the relief structure, of a laser beam that is focused on a track on the surface.

A drawback of the CD(-ROM) was that for consumers it was not possible to record. Therefore the CD-R was introduced in 1990, which made it possible for consumers to write once. Like the CD(-ROM), the CD-R has a 650MB storage capacity, enabling people to make back-up copies of their CD(-ROM)s or to create their own data. In 1997 the limitation of recording once was overcome by the introduction of the CD-ReWritable (CD-RW). With the CD-RW it was possible to rewrite on the same disk up to 1000 times.

The enormous success of the compact disk format and the forthcoming of high quality MPEG video material and the introduction of data traffic over the internet caused a growing need for larger storage capacity and higher data transfer rates (for both reading and recording). This initiated a race between manufacturers focused on both speed and data capacity, which eventually resulted into the development of the digital versatile disk (DVD), introduced to the general public in 1997. Its storage capacity of 4.7GB (Gigabytes), and even 8.5GB for the dual layered version, in combination with a maximum data rate of 11.2 megabit per second (Mb/s), easily fulfilled this need. The introduction of the DVD proceeded even faster than that of the CD and its popularity boomed in particular by the movie industry and because of the possibility to play CD's with DVD-players.

The most recent commercially available recordable media are the DVD+R (e.g. Philips), for single time recording, the DVD+RW (e.g. Philips)/DVD-RW (e.g. Pioneer), for multiple writing and the DVD random access memory (DVD-RAM, e.g. MEI). Like the (single layered) DVD disk both the DVD+R and DVD+RW disks have a storage capacity of 4.7GB. For instance see [2], pp. 99-101.

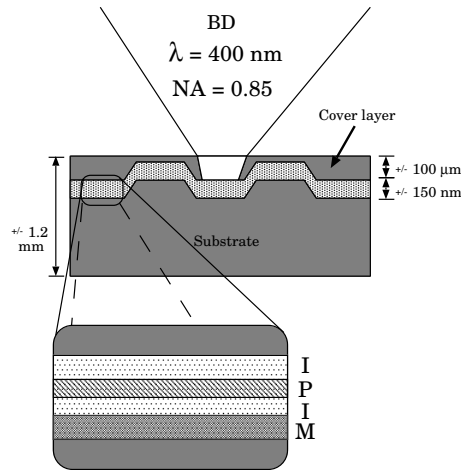


Figure 1.1: An illustration of the stack for the Blu-ray disk, which has an IPIM recording stack.

The latest medium in the race for speed and storage capacity among (re)writable storage media, developed within the framework of high-definition television (HDTV) by Philips and Sony in 1999, is the Blu-ray disk (BD) (the former digital video recording disk (DVR) standard). A single layer BD disk has a storage capacity of 23.5GB or 25GB, whilst the capacity of the double layer version is aimed at a dazzling 47GB or 50GB. Table 1.1 gives an overview of some properties of several of the recordable media.

## 1.2 Dye and Phase-change recording

In contrast to read-only media like the CD(-ROM) and DVD, the tracks of (re-)writable disks are grooved. These grooves are used to guide the spot during reading or recording. The distance between two adjacent tracks is called the track pitch (TP). See Table 1.1. The write once and rewritable disks all consist of several stacked layers. The materials, the thickness and the number of layers depends on the type of disk. In between a pre-grooved substrate of poly-carbonate and another substrate layer, the so called *recording stack* is situated.

For write once disks (CD-R, DVD+R), the recording stack consists of a metallic mirror layer and a layer of organic dye. During the recording process, when a focused laser pulse illuminates it, the dye decomposes, which causes among others the optical properties of the dye to irreversibly change. The written marks have various lengths representing the digitally encoded data.

For rewritable media like the CD-RW, DVD+RW and BD, use is made of a so called phase-change material. Such a material has the property that it can be (locally) changed very quickly from a crystalline to an amorphous state and vice versa by means of heating with a laser. The recording stack of a typical rewritable disk consists of four layers. This structure is called an IPIM layer stack. On top of the pre-grooved substrate made of poly-carbonate or glass, is a dielectric **I**nterference layer. On top of this dielectric layer there are subsequently the **P**hase-change layer, another dielectric **I**nterference layer, a metallic **M**irror layer and

Table 1.1: Optical and mechanical specifications of several recordable media. (TP = track pitch)

medium	$\lambda$ [nm]	TP [ $\mu$ m]	capacity [GB]
CD(-R/-RW)	780	1.60	0.65
DVD(-R/+RW)	650	0.74	4.7
BD	400	0.32	23.5/25

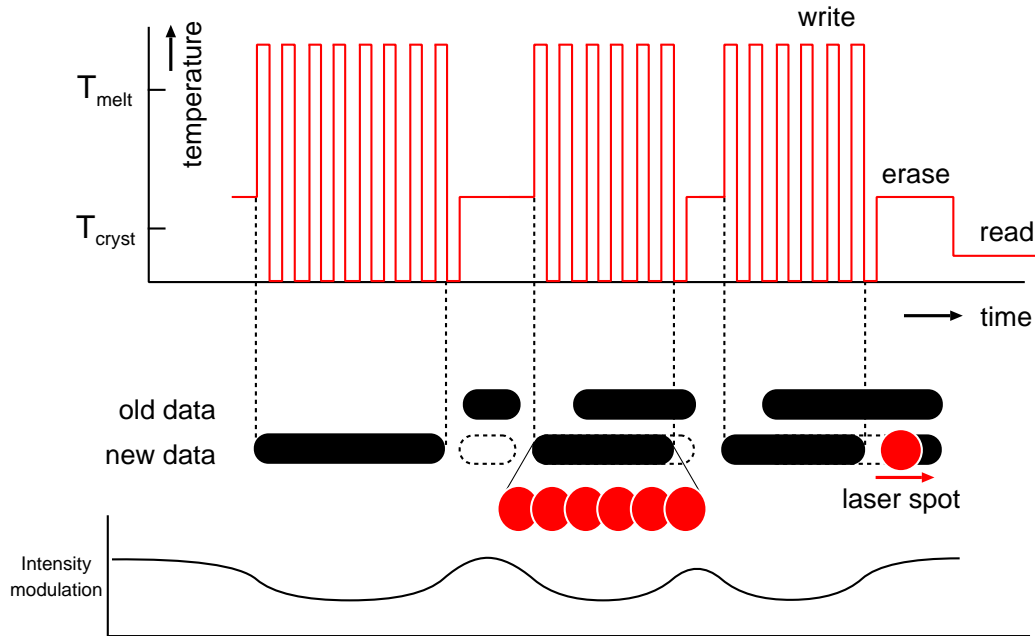


Figure 1.2: Strategy for direct overwrite. During reading, modulations in the intensity of the reflected light can be measured.

finally the protective cover layer. For BD disks a substrate cover layer of just  $100\ \mu\text{m}$  is used. See Figure 1.1.

The metallic layer of the recording stack acts as a heat sink during recording. During the reading process it is used to reflect the incident laser light. The various thicknesses and chemical compositions of the different layers of the recording stack are optimized to fulfill several optical, thermal and mechanical requirements. For example, the thickness of the dielectric and metal layers are chosen such that the optical contrast between the two states of the recording layer is optimized.

The reading of the data is based on the differences in the optical properties of the marks and the surrounding recording material which cause differences in the intensities of the reflected laser light. These intensity variations are measured with a detector.

There are several ways of writing the amorphous marks. Depending on the system, 'groove'-recording or 'land and groove'-recording can be used. In case of 'groove'-recording, the marks are only written in the grooves of the disk. When 'land and groove'-recording is used the marks are written in the lands of the pre-grooved substrate as well as in the grooves.

The actual writing is done by using 'multi-pulse recording'. With this recording technique each mark is formed by a train of short high power laser pulses generating overlapping amorphous dots, as shown in Figure 1.2. To avoid the accumulation of heat, the power of the laser is set to a low level, such that the molten material is cooled to below the crystallization temperature of the phase-change material (quenching). When marks have to be erased, the laser power is set to a certain level which is just high enough to crystallize the material and erase any possibly present previously written marks. Because this system allows the direct overwriting of previous marks, it is generally referred to as Direct Overwrite (DOW). Reading the recorded data is done at a power level fairly below the erasure power level.

### 1.3 Motivation for this research project

The rewritable disks have a narrow track pitch to enable a high areal data density. Unfortunately, this causes optical and thermal cross-track cross talk between adjacent tracks. It has been shown that this optical cross-

track cross talk can be reduced to an acceptable level by tuning the groove depth [16].

During recording, the thermal cross-track cross talk becomes a serious problem, because previously written marks in adjacent tracks can be partially or even completely erased. This undesirable side-effect is due to thermal diffusion from the central track and energy absorption in the adjacent tracks [10].

It has also been observed that on disks with a narrow track pitch the cross-erasure for land recording differs from the cross-erasure effects for groove recording. Moreover, the shape of the written marks on lands are different from those on grooves [3].

The above mentioned effects can be studied by means of simulations. This can be done in three steps. The first step is the creation of an incident field (e.g. a focused spot), which can for instance be done by using the Diffract program developed by Peng and Mansuripur [24]. The second step is the determination of the amount of light that is absorbed in the medium. The absorbed energy is converted into heat and acts as a source term in the heat diffusion equation, from which the temperature distribution in the medium can be calculated in the third step.

Chubing Peng and M. Mansuripur have performed such simulations to determine the temperature distribution within a phase-change stack under the influence of a focused laser beam. For their simulations the authors used a Gaussian incident beam. To determine the absorbed electromagnetic energy they used the finite difference in the time-domain (FDTD) method. They determined the thermal diffusion within the disk by using the finite difference scheme. Peng and Mansuripur have integrated both these calculations in a program called Media [26].

At the Philips Research Laboratories (Natlab) two models were developed. The first model is a finite difference model in which the light absorption is analytically described (Poyning vector) for a layered geometry. The reflected and transmitted fields are calculated iteratively per layer. This model is based on papers published by Mansuripur et al. [7], [8]. For the finite difference model an additional mark-formation model has been developed [10].

The second model is based on the finite element method (FEM) [11]. With this model the temperature distribution can be calculated within three-dimensional geometries similar to the one shown in Figure 1.3. A drawback of this model is that the absorbed energy can only be provided by means of an analytical function (e.g. in case of a spot a Gaussian distribution is taken). In the model the movement of the spot over the geometry is taken into account and the model is thus time dependent, even when the intensity of the spot is constant. The intensity of the laser can be varied in time.

The analytical Gaussian distribution is too inaccurate when grooved structures are modelled, since the sloped edges of the grooves are not be taken into account. To obtain more accurate results, vector diffraction calculations need to be included in the heat diffusion model. By including vector diffraction calculations, in addition it becomes possible to perform sensitivity studies with respect to the groove geometry etc.

Around 1990 Urbach and Merckx developed a finite element program called Cyclop, with which electromagnetic diffraction problems on periodic structures in a two-dimensional geometry can be solved rigorously. *Diffraction* or *scattering* is the phenomenon that the direction of light is changed at interfaces between optically different materials.

The first version of Cyclop from 1990 was extended around 1998 to enable the simulation of general three-dimensional incident fields. The coordinate system is chosen such that the geometry is periodic in the  $x$ -direction and translation invariant in the  $y$ -direction (see Figure 1.3). In this extended version of Cyclop the incident three-dimensional spot is decomposed into a sum of quasi-periodic incident fields. These fields are quasi-periodic in the  $x$ -direction and harmonic with respect to the  $y$ -coordinate. For a quasi-periodic incident field, the scattering problem can be shown to be equivalent to a two-dimensional boundary value problem in a rectangular cell in a plane  $y = \text{constant}$ , whose width in the  $x$ -direction is equal to one period and which is such that all interfaces of the stack are contained in the cell. The fields that are computed in the cell must then be expanded from the cell to the three-dimensional region as shown in Figure 1.3. By adding all these expanded fields coherently, the total three-dimensional field in the disk region is obtained. This model is often called  $2\frac{1}{2}$ -dimensional because the geometry is two-dimensional and the light distribution is three-dimensional. From this expanded solution the absorbed electromagnetic energy density can be derived. This data can then quite easily be mapped from the Cyclop mesh onto the mesh of the thermal

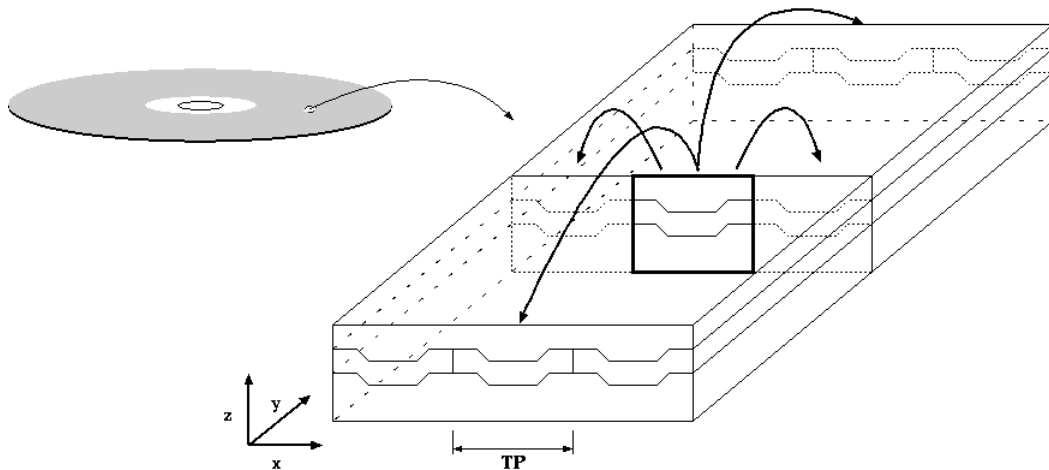


Figure 1.3: A three-dimensional region of an optical disk of which the dimensions are in the order of the track pitch (TP). The grooved structure is periodic in the  $x$ -direction, the  $y$ -axis is in the direction of track and the  $z$ -axis is parallel to the optical axis of the illumination system. In case no data has been written on the optical disk, the geometry is translation invariant in the  $y$ -direction. The cross-section shows a bounded two-dimensional region of which the width equals the track pitch (TP), called a cell, in which the light distribution can be calculated using Cyclop.

model as a replacement for the analytically provided heat source.

## 1.4 Objective of this research project

In the previous section it has been indicated that the Cyclop program can be used to calculate the absorbed energy that serves as input for the thermal model. This requires several additions to and modifications of both models.

The main objective of this research project was to realize the integration of both FEM programs in order to improve the thermal model. To that end roughly the following steps had to be taken:

1. Expansion of Cyclop's two-dimensional solution vector to a three-dimensional geometry.
2. Extension of the functionality of Cyclop by including the calculation of the absorbed electromagnetic energy.
3. Integration of expanded results in the heat diffusion model via an interpolation routine.
4. Validation of local absorption values and temperature distribution via experiments and program Media.

## 1.5 Acknowledgements

First of all I would like to thank Paul Urbach for being my supervisor. His enthusiasm and knowledge of mathematical physics have been of great inspirational and supportive value when working on this graduation project. I also want to thank Guus Segal for his help in solving most Sepran related problems. I like to thank Erwin Meinders for his support concerning the thermal model. Last but not least I would like to express my appreciation to Jurgen Rusch for sharing his knowledge of Fortran programming, Sepran, Kornshell scripting and various other software related issues with me.

## 1.6 About this report

In Chapter 2 the FEM heat diffusion model used by Meinders is discussed. In Chapter 3 we give a general overview of the optical model. In Chapter 4 Maxwell's electromagnetic theory of light is summarized. A formula is derived for the absorbed electromagnetic energy. The incident field is treated in Chapter 5. Then, in Chapter 6 the model for the scattering of light within an optical disk is described. Chapter 7 gives an overview of the structure of the original Cyclop program. The extensions made to Cyclop such as the expansion of the two-dimensional solutions are presented in Chapter 8. The visualization of the three-dimensional field is also treated. In Chapter 9 the integration of the Cyclop output and the heat diffusion model is described. In Chapter 10 some numerical simulations are discussed. Finally, Chapter 11 contains conclusions and recommendations.

## Chapter 2

# The heat diffusion model

In this chapter we shall describe the FEM heat diffusion model as it is presently used. In Section 2.3 we will point out how the optical program Cyclop will be integrated with the heat program.

### 2.1 Current model

When a spot is focused on an optical disk, part of the incident light is absorbed by the recording layer (dye/phase-change) and other absorbing layers (metallic mirror). The absorbed electromagnetic energy is converted into heat. The thus generated heat can be described by a heat source  $Q(x, y, z, t)$  [ $W/m^3$ ] which depends on position and time. The time dependence is caused by the rotation of the disk and possibly also by the time dependent illumination. The temperature  $T(x, y, z, t)$  satisfies the heat diffusion equation:

$$\rho C_p \frac{\partial T}{\partial t} - \nabla \cdot [\kappa \nabla T] = Q(x, y, z, t), \quad (2.1)$$

The values of the heat conductivity  $\kappa$  [ $W/m/^\circ C$ ], the density  $\rho$  [ $kg/m^3$ ] and specific heat  $C_p$  [ $J/kg/^\circ C$ ] are in general different for each layer of the optical disk.

Equation (2.1) can be solved in a three-dimensional region as shown in Figure 2.1. In the  $x$ -direction (the radial direction) of the chosen cartesian coordinate system  $(x, y, z)$ , this computational box is at least several tracks wide, such that the influence of the focused laser beam on adjacent tracks can also be taken into account. The  $y$ -direction is parallel to the grooves (axial direction) and the  $z$ -direction is parallel to the optical axis of the illumination system. The configuration is invariant with respect to translations along the  $y$ -direction. Due to the rotation of the disk, the laser spot moves in the positive  $y$ -direction with speed  $v$ . At  $t = t_0$  the heat source enters the box at  $y = y_0$  and leaves it at  $y = y_1$  ( $y_0 < y_1$ ) at  $t = t_1$ , whence  $y_1 - y_0 = v(t_1 - t_0)$ .

At every time  $t$ ,  $t_0 \leq t \leq t_1$ , we assume that the heat source can be written as

$$Q(x, y, z, t) = f(t)W(x, t, z) \quad (2.2)$$

where  $f(t)$  is defined by

$$f(t) = \begin{cases} I_r & \text{while reading,} \\ I_w & \text{while recording/writing,} \\ I_e & \text{while erasing.} \end{cases} \quad (2.3)$$

The time independent quantity  $W(x, y, z)$  represents the absorption in a point  $(x, y, z)$  within the region where the heat diffusion equation is solved. At any time  $t$  the intensity level  $I$  of the heat source depends on which process (reading, recording or erasing) is modelled.

In the presently used model a two-dimensional Gaussian intensity distribution in the axial and radial direction is assumed for the heat source  $Q$  in the recording layer. In the  $z$ -direction an exponential decrease with

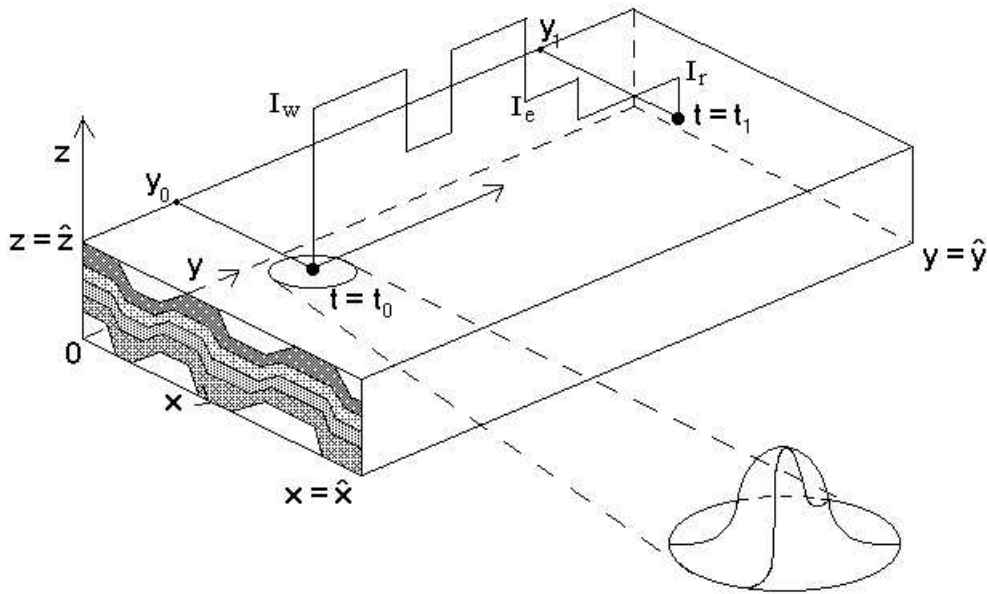


Figure 2.1: Geometry for a grooved recording stack. The incident laser spot causes a more or less Gaussian energy distribution in the  $x$ - and  $y$ -direction. The laser spot moves from  $y = y_0$  at  $t = t_0$  along a groove until  $y = y_1$  at  $t = t_1$  during which the intensity level of the laser can be switched between  $I_r$  (reading),  $I_e$  (erasing) and  $I_w$  (writing).

a factor  $\alpha$  is chosen. At every  $t$ ,  $t_0 \leq t \leq t_1$ , the heat source satisfies

$$Q(x, y, z, t) = f(t)e^{-\frac{(x-x_0)^2}{\sigma_x^2} - \frac{(y-y_0-vt)^2}{\sigma_y^2} - \alpha z}, \quad (2.4)$$

with  $f(t)$  as defined in (2.3) and where  $x_0$  and  $y_0$  are the  $(x, y)$ -coordinates of the point where the center of the spot enters the computational box.  $\sigma_x$  and  $\sigma_y$  determine the spot size.

Since the problem is taken to be adiabatic (i.e. there is no loss or gain of heat across the boundaries) the boundary conditions for equation (2.1) are

$$\frac{\partial T}{\partial n} = 0, \quad (2.5)$$

where  $n$  is the outwards pointing normal at any of the boundary surfaces.

## 2.2 Solving the heat diffusion equation by using Sepran

The above described three-dimensional heat diffusion problem is solved by using the Sepran FEM-package. Since in Sepran the heat diffusion equation (2.1) is a standard problem, the user has to provide Sepran only with information concerning the mesh, the boundary conditions and the type of solver to be used.

Each layer in the stack is assigned to a single piped surface group. On each of these piped surfaces a mesh consisting of triangle elements is created. In Figure 2.2 a mesh is shown created by the Sepran mesh generator for a geometry containing two grooves. On each element of the mesh the temperature solution is interpolated by piecewise linear basis functions.

The finite linear system of equations corresponding to (2.1) is for every time step iteratively solved using the conjugate gradient (CG) method. For the time-integration the Euler implicit method is used.

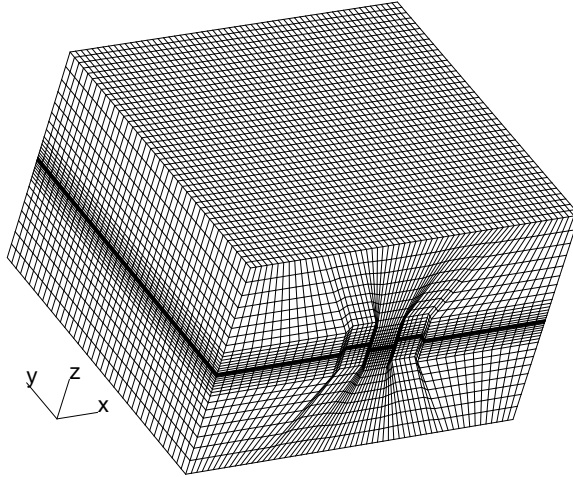


Figure 2.2: A three-dimensional representation of a mesh created with the Sepran mesh generator.

## 2.3 Integration of the thermal model with Cyclop

As has been explained in the Introduction, we want to improve the accuracy of the current heat diffusion model by replacing the currently assumed Gaussian heat source by a heat source that is calculated rigorously with Cyclop.

Hence, the time independent absorbed energy  $W(x, y, z)$  in equation (2.4) must be provided by Cyclop. Since the absorption of energy in Cyclop is a priori only known on the nodal points  $(\tilde{x}, \tilde{y}, \tilde{z})$  of the grid used by Cyclop that is contained in a two-dimensional cell as described in the previous chapter, a mapping  $\phi$  of the Cyclop data to the nodes of the mesh of the thermal model is needed:

$$W(\tilde{x}, \tilde{y}, \tilde{z}) \xrightarrow{\phi} W(x, y, z) \quad (2.6)$$

## Chapter 3

# Overview of the optical model

In this chapter we will give a general introduction to the optical part of the recording process. First a description of the optical system that is used to read and write data on an optical disk is given. In Section 3.2 the illumination of the disk is considered. We conclude this chapter with a section about diffraction gratings.

### 3.1 Optical reading and writing

The various data storage disks mentioned in the Introduction all have in common that the reading, and if applicable writing, of data on the disk is done optically. The reading is based on intensity differences of the reflected light when the spot is above a mark or a non-mark. The writing is based on the absorption of the light energy in either the dye or the phase-change layer. In Figure 3.1 the setup of an optical head for

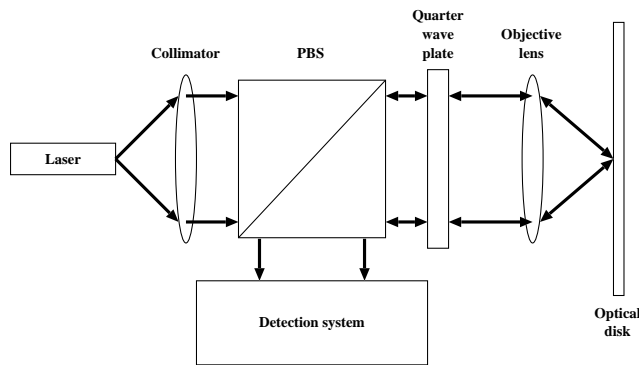


Figure 3.1: Setup for an optical system.

the reading of data from an optical disk is shown. The optical head contains a laser diode, a collimating lens, a polarizing beam splitter (PBS), a quarter wave plate, an objective lens and the detection system. The collimating lens is used to collimate the diverging linearly polarized beam emitted by the laser diode. After passing through the PBS, the light incident on the quarter wave plate is circularly polarized. Finally, the objective lens focusses the beam on the optical disk.

The light that is reflected by the metallic layer of the disk is collimated by the objective lens on its way back through the optical system. The quarter wave plate then converts the dominantly circularly polarized reflected light into a linear polarized beam such that the polarization is perpendicular to that of the incident beam. The PBS finally redirects the reflected beam onto the detection system. Based on a priori knowledge about the differences between the reflected intensities when the spot is focused on a pit or a non pit (for

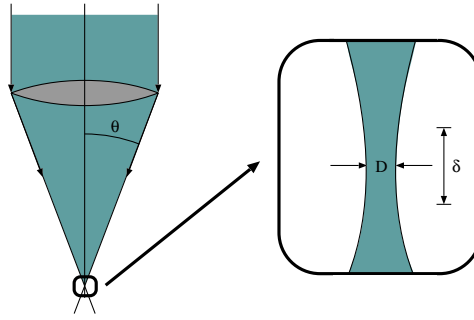


Figure 3.2: The NA of a lens is given by  $\sin(\theta)$ .

prerecorded discs), on a decomposed or intact dye material (for write once media) or on the amorphous or crystalline state of phase-change material (for rewritable media), the detection system can determine whether a 'zero' or a 'one' is read. See [2], pp. 101-102.

The reading of data from an optical disk is done with the intensity of the laser set to a value  $I_r$ . For recordable media, the intensity of the laser pulses during the recording process is set to a much higher value  $I_w$ . In case of rewritable media, the laser's intensity can also be set to a level  $I_e$  between  $I_r$  and  $I_w$  to erase previously written marks.

In order to be able to correctly read from, and write on an optical disk, the focused spot must be kept on the center of a track. When the optical head moves away from the track's center, an asymmetry in the reflected field is induced. Whenever such an asymmetry is detected, the optical head is guided such that the beam is again focused on the center of a track. This process is called tracking.

## 3.2 Illumination of the disk

In geometrical optics the assumption is made that a parallel incident beam on a positive lens converges into a single point. For the optical system considered in this research project, where structures with dimensions in the order of the wavelength of the light are considered, the geometrical approach of a perfect point spot is too coarse. Due to diffraction by the finite aperture of the lens, the diameter of a focused spot is given by [5]:

$$D \approx \frac{\lambda}{\text{NA}}. \quad (3.1)$$

In formula (3.1),  $\lambda$  is the wavelength of the incident light and NA is the numerical aperture of the objective lens. The NA is the sine of the angle between the outer ray and the principle axis of the objective lens. The focal depth  $\delta$  of a spot is given by (see Figure 3.2):

$$\delta \approx \frac{\lambda}{\text{NA}^2}. \quad (3.2)$$

Table 3.1: Diameter and focal depth of the incident light for various types of optical storage disks. Average values for the track pitch (TP) and thickness ( $\Delta$ ) of the recording stack are also given. The wavelength is in air.

medium	$\lambda$ [nm]	NA [-]	D [nm]	TP [nm]	$\delta$ [nm]	$\Delta$ [nm]
CD(-R/-RW)	780	0.50	1560	1500	3120	$\approx 250$
DVD(-R/+RW)	650	0.65	1000	740	$\approx 1540$	$\approx 250$
BD	400	0.85	$\approx 470$	320	$\approx 550$	$\approx 150$

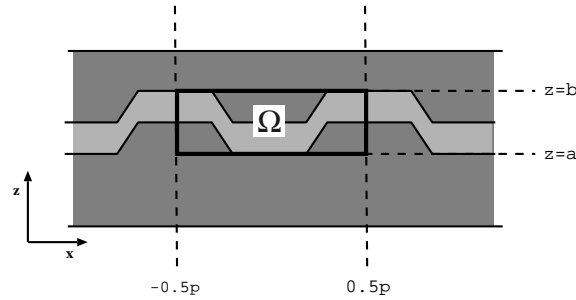


Figure 3.3: Schematic visualization of the area  $\Omega$  in a cross-section of an optical disk.

In Table 3.1 the spot diameters for various optical storage media are listed. We remark that the diameter of the spot is always larger than the track pitch. Consequently, part of the incident light will inevitably fall onto adjacent tracks. Knowing this makes the occurrence of cross-track cross talk even more conceivable in case of 'land and groove' recording.

The focal depth is of special interest during the writing process since it is important to get the highest energy density within the recording layer. When a spot is incident on a recording stack it is very difficult to choose the proper focal plane because reflections between layers of the stack have to be taken into account. However, Table 3.1 suggests that when reflections are neglected there is no need to accurately determine the focus height because the focal depth is at least a factor four larger than the thickness of the recording stack. It is therefore sufficient to make sure that the recording stack lies approximately at a distance of at most  $\frac{\delta}{2}$  from the spot in air.

### 3.3 Diffraction gratings

A diffraction grating is a periodic structure which disturbs the amplitude and/or phase of an incoming wave such that the reflected and/or transmitted energy is diffracted into a finite number of propagating orders. The propagating orders are the discrete directions in which the diffracted light propagates at large distances from the grating. The directions of the diffracted orders depend on the relationship between the period of the grating and the wavelength of the light.

The land and groove structure of an optical disk can be considered to be a diffraction grating. In Figure 3.3 a part of the cross-section of Figure 1.3 in a plane  $y = \text{constant}$  is shown. The two-dimensional region  $\Omega$  is chosen such that its width in  $x$ -direction is equal to one period of the grating and the upper ( $z = b$ ) and lower ( $z = a$ ) boundaries are chosen such that all non-flat surfaces are contained in the domain while the upper and lower half spaces are as large as possible. For the region  $\Omega$ , which we will refer to as a (unit) cell, a boundary value problem can be derived by using rigorous diffraction theory, based on Maxwell's equations.

In the following chapters we will successively discuss the Maxwell equations and general wave optics. In Chapter 6 we will discuss the boundary value problem on  $\Omega$  in more detail.

## Chapter 4

# Maxwell's equations

Light, as has been discovered by the Scottish physicist James Clerk Maxwell (1831-1879), is an electromagnetic phenomenon. It is the transfer of electromagnetic energy and momentum in the visible spectrum. Light can be described by electric and magnetic fields, which dependent on position and time, and which are emitted by moving electric particles. Maxwell's formulation of electricity and magnetism was published in *A Treatise on Electricity and Magnetism* in 1873, which included the formulas today known as Maxwell Equations. In this chapter Maxwell's equations for free space and inside matter are discussed. In Section 4.2 energy conservation and the Poynting vector are discussed. In the final section of this chapter we will describe how quantities such as the absorbed energy can be derived from the electromagnetic field. The theory presented in this chapter can for instance be found in [6].

### 4.1 Maxwell's equations in free space

Let the sources that induce a certain electromagnetic field have (free) *charge density*  $\rho(\mathbf{r},t)$  and (free) *current density*  $\mathcal{J}(\mathbf{r},t)$ . The conservation of charge is expressed by the following equation of continuity:

$$\nabla \cdot \mathcal{J}(\mathbf{r},t) + \frac{\partial \rho}{\partial t} = 0. \quad (4.1)$$

That is, the outwards flux of the current density through a closed surface equals the decrement of charge per unit time within the volume bounded by this surface.

Let  $\mathcal{E}$  and  $\mathcal{H}$  denote the electric and magnetic field strengths respectively, induced by the sources in free space and let  $\epsilon_0$  and  $\mu_0$  denote the *electric permittivity* and *magnetic permeability* of vacuum, respectively. Maxwell's equations are:

$$\nabla \times \mathcal{H} = \epsilon_0 \frac{\partial \mathcal{E}}{\partial t} + \mathcal{J}, \quad (4.2)$$

$$\nabla \times \mathcal{E} = -\mu_0 \frac{\partial \mathcal{H}}{\partial t}, \quad (4.3)$$

$$\nabla \cdot (\mu_0 \mathcal{H}) = 0, \quad (4.4)$$

$$\nabla \cdot (\epsilon_0 \mathcal{E}) = \rho. \quad (4.5)$$

To be able to calculate the electromagnetic field components emitted by charges and currents that depend on time, in general initial conditions are needed. However, when the sources are harmonic with respect to time with given frequency  $\omega$ , the emitted electromagnetic fields are also time-harmonic and initial conditions are not needed.

It is convenient to use complex variables to denote time-harmonic physical quantities. By taking the real part of the complex quantity, the physical quantity is retrieved. The time dependence of the quantity is taken

to be as  $e^{-i\omega t}$ , so that for an arbitrary time-harmonic real quantity  $\mathcal{G}(\mathbf{r}, t)$  we have

$$\mathcal{G}(\mathbf{r}, t) = \text{Re} [\mathbf{G}(\mathbf{r})e^{-i\omega t}], \quad (4.6)$$

where  $\mathbf{G}(\mathbf{r})$  is the complex amplitude. Note that as a consequence of this choice all time derivatives are replaced by multiplications by  $-i\omega$ .

We denote the complex charge density and current density by  $\rho(\mathbf{r})$  and  $\mathbf{J}(\mathbf{r})$  and the complex electric and magnetic fields by  $\mathbf{E}(\mathbf{r})$  and  $\mathbf{H}(\mathbf{r})$ . Then we have:

$$\rho(\mathbf{r}, t) = \text{Re}[\rho(\mathbf{r})e^{-i\omega t}], \quad (4.7)$$

$$\mathcal{J}(\mathbf{r}, t) = \text{Re}[\mathbf{J}(\mathbf{r})e^{-i\omega t}], \quad (4.8)$$

$$\mathcal{E}(\mathbf{r}, t) = \text{Re}[\mathbf{E}(\mathbf{r})e^{-i\omega t}], \quad (4.9)$$

$$\mathcal{H}(\mathbf{r}, t) = \text{Re}[\mathbf{H}(\mathbf{r})e^{-i\omega t}]. \quad (4.10)$$

By substituting equations (4.7-4.10) into Maxwell's equations (4.2-4.5) we find for the complex quantities:

$$\nabla \times \mathbf{H} = -i\omega\epsilon_0\mathbf{E} + \mathbf{J}, \quad (4.11)$$

$$\nabla \times \mathbf{E} = i\omega\mu_0\mathbf{H}, \quad (4.12)$$

$$\nabla \cdot \mathbf{H} = 0, \quad (4.13)$$

$$\nabla \cdot (\epsilon_0\mathbf{E}) = \rho. \quad (4.14)$$

By applying the curl operator to equation (4.12) and by substituting equation (4.11) we obtain the so called vector Helmholtz equation for the electric field  $\mathbf{E}$ :

$$\omega^2\epsilon_0\mu_0\mathbf{E} - \nabla \times \nabla \times \mathbf{E} = -i\omega\mu_0\mathbf{J}. \quad (4.15)$$

By using the operator identity

$$\nabla \times \nabla \times \mathbf{U} = \nabla \nabla \cdot \mathbf{U} - \Delta \mathbf{U}, \quad (4.16)$$

(which is valid in cartesian coordinates only) where:

$$\Delta \mathbf{U} = \frac{\partial^2 \mathbf{U}}{\partial x^2} + \frac{\partial^2 \mathbf{U}}{\partial y^2} + \frac{\partial^2 \mathbf{U}}{\partial z^2}, \quad (4.17)$$

(4.15) can be written as:

$$\omega^2\epsilon_0\mu_0\mathbf{E} + \Delta \mathbf{E} = \nabla \left( \frac{\rho}{\epsilon_0} \right) - i\omega\mu_0\mathbf{J}, \quad (4.18)$$

This shows that every (cartesian) component of the electric field satisfies the scalar Helmholtz equation. Any solution  $\mathbf{E}$  of equation (4.18) of course also has to satisfy equation (4.14). By eliminating the electric field one finds analogously that the (cartesian) components of the magnetic field satisfy:

$$\omega^2\epsilon_0\mu_0\mathbf{H} + \Delta \mathbf{H} = -\nabla \times \mathbf{J}. \quad (4.19)$$

Solutions of equation (4.19) obviously also have to satisfy equation (4.13) as well.

## 4.2 Energy conservation and the Poynting vector

From Maxwell's equations a conservation law for the energy can easily be derived. Since energy is quadratic in the fields we shall first use the real physical quantities. By taking the scalar product of (4.2) with  $\mathcal{E}$  and subtracting the scalar product of (4.3) with  $\mathcal{H}$  we find:

$$\nabla \cdot (\mathcal{E} \times \mathcal{H}) = -\mathcal{E} \cdot \mathcal{J} - \frac{\partial}{\partial t} \left( \frac{\epsilon_0}{2} \mathcal{E} \cdot \mathcal{E} + \frac{\mu_0}{2} \mathcal{H} \cdot \mathcal{H} \right), \quad (4.20)$$

where we have used the vector equality:

$$\nabla \cdot (\mathbf{U} \times \mathbf{V}) = -\mathbf{U} \cdot \nabla \times \mathbf{V} + \mathbf{V} \cdot \nabla \times \mathbf{U}. \quad (4.21)$$

Integration of (4.20) over a volume  $V$  bounded by a surface  $S$  with outward pointing normal  $\mathbf{n}$  results in:

$$-\int_V \mathcal{J} \cdot \boldsymbol{\mathcal{E}} \, dv = \frac{\partial}{\partial t} \int_V \frac{1}{2} [\boldsymbol{\mathcal{E}} \cdot (\epsilon_0 \boldsymbol{\mathcal{E}}) + (\mu_0 \boldsymbol{\mathcal{H}}) \cdot \boldsymbol{\mathcal{H}}] \, dv + \oint_S (\boldsymbol{\mathcal{E}} \times \boldsymbol{\mathcal{H}}) \cdot \mathbf{n} \, da. \quad (4.22)$$

This integral equality can be interpreted as follows. The left-hand side of equation (4.22) is the power exerted on the current density  $\mathcal{J}$  within volume  $V$ . The time derivative of the volume integral on the right-hand side of equation (4.22) represents the change per unit time of the electromagnetic energy contained in  $V$ . The surface integral can be interpreted as the rate of energy flow outwards across the closed surface  $S$ .

The rate of energy flow per unit time per unit area in the direction of the normal is given by :

$$\boldsymbol{\mathcal{S}} \cdot \mathbf{n} = (\boldsymbol{\mathcal{E}} \times \boldsymbol{\mathcal{H}}) \cdot \mathbf{n}, \quad (4.23)$$

where  $\boldsymbol{\mathcal{S}} = \boldsymbol{\mathcal{E}} \times \boldsymbol{\mathcal{H}}$  is called the *Poynting vector*.

An instantaneous value of the energy flow  $\boldsymbol{\mathcal{S}}$  is an impractical quantity to measure because at optical frequencies ( $\omega \approx \mathcal{O}(10^{15})$ )  $\boldsymbol{\mathcal{S}}$  is an extremely rapidly varying function of time. Therefore the average over a period of  $\tau = \frac{2\pi}{\omega}$  is taken. In the following we will make use of the fact that the fields are time-harmonic of frequency  $\omega$ .

Let  $\mathcal{A} = \text{Re}(Ae^{-i\omega t})$  and  $\mathcal{B} = \text{Re}(Be^{-i\omega t})$  be two quantities and let  $*$  denote the complex conjugate. Then:

$$\begin{aligned} \mathcal{A} \cdot \mathcal{B} &= \text{Re}(Ae^{-i\omega t}) \cdot \text{Re}(Be^{-i\omega t}) = \frac{1}{4}(Ae^{-i\omega t} + A^*e^{i\omega t})(Be^{-i\omega t} + B^*e^{i\omega t}) \\ &= \frac{1}{4}(ABe^{-2i\omega t} + A^*B^*e^{2i\omega t} + A^*B + AB^*). \end{aligned} \quad (4.24)$$

The time-average value of the product taken over an interval of time of length  $\tau$  that is large with respect to the period  $\frac{2\pi}{\omega}$  of the light (i.e.  $\tau\omega \rightarrow \infty$ ) is thus:

$$\begin{aligned} \langle \mathcal{A} \cdot \mathcal{B} \rangle &= \frac{1}{\tau} \int_0^\tau \mathcal{A} \cdot \mathcal{B} \, dt \\ &= \frac{1}{2} \text{Re}(AB^*). \end{aligned} \quad (4.25)$$

For the time-average Poynting vector  $\boldsymbol{\mathcal{S}}$  we thus find:

$$\begin{aligned} \langle \boldsymbol{\mathcal{S}} \rangle &= \langle \boldsymbol{\mathcal{E}} \times \boldsymbol{\mathcal{H}} \rangle \\ &= \langle \text{Re}(\mathbf{E}e^{-i\omega t}) \times \text{Re}(\mathbf{H}e^{-i\omega t}) \rangle \\ &= \frac{1}{2} \text{Re}(\mathbf{E} \times \mathbf{H}^*). \end{aligned} \quad (4.26)$$

We now define the complex Poynting vector by:

$$\mathbf{S} = \frac{1}{2} \mathbf{E} \times \mathbf{H}^*, \quad (4.27)$$

and derive the time-average of the conservation law of electromagnetic energy (4.22). The complex conjugate of (4.11) is:

$$\nabla \times \mathbf{H}^* = i\omega\epsilon_0\mathbf{E}^* + \mathbf{J}^*. \quad (4.28)$$

By using this equation together with (4.12) one finds, similarly to the derivation of (4.20):

$$-\nabla \cdot \mathbf{S} = -\frac{1}{2} \mathbf{E} \cdot \mathbf{J}^* + i\omega \left( \frac{\mu_0}{2} |\mathbf{H}|^2 - \frac{\epsilon_0}{2} |\mathbf{E}|^2 \right) \quad (4.29)$$

$$= -\frac{1}{2} \mathbf{E} \cdot \mathbf{J}^* + 2i\omega (\langle w_m \rangle - \langle w_e \rangle), \quad (4.30)$$

where  $\langle w_m \rangle$  and  $\langle w_e \rangle$  represent the time-average magnetic and electric energy density, respectively:

$$\langle w_m \rangle = \frac{\mu_0}{4} |\mathbf{H}|^2, \quad \langle w_e \rangle = \frac{\epsilon_0}{4} |\mathbf{E}|^2. \quad (4.31)$$

### 4.3 Maxwell's equations in matter

Let us consider an isotropic non-magnetic dielectric medium that is, as a whole, electrically neutral. The medium is said to be polarized when a separation of positive and negative electric charges has been effected. The sources responsible for the polarization can be divided into primary (external) and secondary (internal) sources. The primary sources are by definition those sources of which the charge and current densities are assumed to be known, for example the laser source in optical recording. The electromagnetic field induced by these sources causes charges within the dielectric medium to oscillate and atoms within the matter to act like oscillating dipoles. These oscillating charges in turn induce an electromagnetic field themselves also and are called secondary sources.

The *electric polarization*  $\mathbf{P}$  can be expressed in terms of the total macroscopic electric field induced by the primary sources as well as all secondary sources as follows [4]:

$$\mathbf{P} = \epsilon_0 \chi \mathbf{E}. \quad (4.32)$$

The factor  $\chi$  is called the *electric susceptibility*. The *relative electric permittivity*  $\epsilon$  and the *index of refraction*  $n$  are now defined by:

$$\epsilon = 1 + \chi, \quad (4.33)$$

$$n = \sqrt{\epsilon}. \quad (4.34)$$

In case of a conducting medium such as a metal, the conduction electrons also form a secondary source. The current density due to the polarization and the conducting electrons are, respectively

$$\mathbf{J}_d = -i\omega \mathbf{P} = -i\omega \epsilon_0 \chi \mathbf{E}, \quad (4.35)$$

and

$$\mathbf{J}_e = \sigma \mathbf{E}, \quad (4.36)$$

in which  $\sigma$  is the *electric conductivity* of the medium. The charge density due to the polarization is

$$\rho_d = -\nabla \cdot \mathbf{P} = -\epsilon_0 \nabla \cdot (\chi \mathbf{E}), \quad (4.37)$$

while the charge density due to the conduction electrons is given by

$$\rho_e = -\frac{i}{\omega} \nabla \cdot (\sigma \mathbf{E}). \quad (4.38)$$

The total charge density is the sum of the densities of the primary (p) and secondary (s) sources. Therefore

$$\begin{aligned} \rho &= \rho_p + \rho_s = \rho_p + \rho_d + \rho_e \\ &= \rho_p - \nabla \cdot \left[ \epsilon_0 \left( \chi + i \frac{\sigma}{\omega \epsilon_0} \right) \mathbf{E} \right]. \end{aligned} \quad (4.39)$$

Analogously the total current density is given by

$$\begin{aligned} \mathbf{J} &= \mathbf{J}_p + \mathbf{J}_s = \mathbf{J}_p + \mathbf{J}_d + \mathbf{J}_e \\ &= \mathbf{J}_p - i\omega \epsilon_0 \left( \chi + i \frac{\sigma}{\omega \epsilon_0} \right) \mathbf{E}. \end{aligned} \quad (4.40)$$

By substituting equations (4.39) and (4.40) in the (complex) Maxwell equations we get:

$$\nabla \times \mathbf{H} = -i\omega\epsilon_0 \left( \epsilon + i\frac{\sigma}{\omega\epsilon_0} \right) \mathbf{E} + \mathbf{J}_p, \quad (4.41)$$

$$\nabla \times \mathbf{E} = i\omega\mu_0\mathbf{H}, \quad (4.42)$$

$$\nabla \cdot \mathbf{H} = \mathbf{0}, \quad (4.43)$$

$$\nabla \cdot \left[ \epsilon_0 \left( \epsilon + i\frac{\sigma}{\omega\epsilon_0} \right) \mathbf{E} \right] = \rho_p. \quad (4.44)$$

Hence, in presence of dielectric media and/or conductors, the Maxwell equations in matter have the same form as the Maxwell equations for free space, except that  $\epsilon_0$  must be replaced by  $\epsilon_0(\epsilon + i\sigma/\omega\epsilon_0)$ . It is convenient to write  $\epsilon = \epsilon' + i\epsilon''$  instead of  $\epsilon + i\sigma/\omega\epsilon_0$ , so that the conductivity  $\sigma$  contributes to the imaginary part  $\epsilon''$  of the relative dielectric permittivity  $\epsilon$ . Across interfaces between different media where  $\epsilon$  is discontinuous the tangential field components of both the electric and the magnetic field are continuous.

Provided that  $\epsilon_0$  is replaced by  $\epsilon_0\epsilon$  the conservation law of electromagnetic energy for free space is also valid for electromagnetic fields in matter:

$$\frac{1}{2} \nabla \cdot (\mathbf{E} \times \mathbf{H}^*) = -\frac{1}{2} \mathbf{E} \cdot \mathbf{J}_p^* + i\omega \left( \frac{\mu_0}{2} |\mathbf{H}|^2 - \frac{\epsilon_0\epsilon}{2} |\mathbf{E}|^2 \right), \quad (4.45)$$

Integration of the real part of (4.45) over a volume  $V$  bounded by a closed surface  $S$  with outward pointing normal  $\mathbf{n}$  gives:

$$\operatorname{Re} \frac{1}{2} \int_V \mathbf{E} \cdot \mathbf{J}_p^* dv = \operatorname{Re} \oint_S (\mathbf{E} \times \mathbf{H}^*) \cdot \mathbf{n} da + \frac{\omega\epsilon_0 \operatorname{Im}(\epsilon)}{2} \int_V |\mathbf{E}|^2 dv \quad (4.46)$$

Note that  $\operatorname{Im}(\epsilon)$  must be positive, otherwise electrical energy would be generated. The sign of  $\operatorname{Im}(\epsilon)$  depends on the choice of the sign of the time-dependence  $e^{-i\omega t}$  of the fields. If we had chosen  $e^{i\omega t}$  instead,  $\operatorname{Im}(\epsilon)$  would be negative. Since the physical fields are given by the real part of the complex quantities, it does not matter which sign one chooses for the exponent of time-dependence factor, as long as one uses one's choice consistently.

In optics it is often justified to assume that the primary sources are at extremely large distances from the considered media, in comparison to the wavelength of the light. Therefore, the primary currents and charges are assumed to be at infinite distance. Hence,  $\mathbf{J}_p = \mathbf{0}$  and  $\rho_p = 0$  in the region of interest. Furthermore, the electromagnetic field induced by time-harmonic primary sources are time-harmonic.

The components of the electromagnetic field in a homogeneous isotropic medium, i.e. a medium in which  $\epsilon$  is constant scalar, will then satisfy

$$\nabla \times \mathbf{E} = i\omega\mu_0\mathbf{H}, \quad (4.47)$$

$$\nabla \times \mathbf{H} = -i\omega\epsilon_0\epsilon\mathbf{E}, \quad (4.48)$$

$$\nabla \cdot \mathbf{H} = \mathbf{0}, \quad (4.49)$$

$$\nabla \cdot (\epsilon_0\epsilon\mathbf{E}) = 0. \quad (4.50)$$

After a derivation analogous to that of equations (4.18) and (4.19) the electromagnetic field will then satisfy the scalar Helmholtz equations:

$$\omega^2\epsilon_0\epsilon\mu_0\mathbf{E} + \Delta\mathbf{E} = \mathbf{0}, \quad (4.51)$$

$$\omega^2\epsilon_0\epsilon\mu_0\mathbf{H} + \Delta\mathbf{H} = \mathbf{0}. \quad (4.52)$$

## 4.4 Absorption and time-average energy density

When the primary currents and charges are not contained within the considered volume  $V$ , the conservation law of electromagnetic energy (4.46) can be written as

$$-\operatorname{Re} \oint_S (\mathbf{E} \times \mathbf{H}^*) \cdot \mathbf{n} \, da = \frac{\omega \epsilon_0 \operatorname{Im}(\epsilon)}{2} \int_V |\mathbf{E}|^2 \, dv \quad (4.53)$$

The left-hand side of (4.53) is the amount of energy that flows into volume  $V$  per unit of time. This energy flux must evidently be equal to the amount of electric energy that is absorbed by matter inside  $V$  per unit of time. Hence

$$\frac{1}{2} \omega \epsilon_0 \operatorname{Im}(\epsilon) |\mathbf{E}|^2 \quad (4.54)$$

is the rate of which energy is absorbed per unit of volume. This energy is converted into heat. Therefore,

$$W(x, y, z) \equiv \frac{1}{2} \omega \epsilon_0 \operatorname{Im}(\epsilon) |\mathbf{E}|^2 \quad (4.55)$$

is the rate at which heat is generated per unit of volume, due to the absorption of the light.

In matter the time-average magnetic and electric energy density are given by:

$$\langle w_m \rangle = \frac{\mu_0}{4} |\mathbf{H}|^2, \quad \langle w_e \rangle = \frac{\epsilon_0}{4} \operatorname{Re}(\epsilon) |\mathbf{E}|^2. \quad (4.56)$$

The total time-average energy density  $\langle w \rangle$  is the sum of these quantities:

$$\begin{aligned} \langle w \rangle &= \langle w_m \rangle + \langle w_e \rangle \\ &= \frac{\mu_0}{4} |\mathbf{H}|^2 + \frac{\epsilon_0}{4} \operatorname{Re}(\epsilon) |\mathbf{E}|^2. \end{aligned} \quad (4.57)$$

In simulations this quantity is visualized to study the effects of interferences due to multiple reflections and scattering of light.

# Chapter 5

## The incident field

In this chapter the incident field is discussed. In Sections 5.1-5.3 plane waves are considered. In Section 5.4 we will discuss the focusing of a beam of light by a positive aberration-free lens. In the concluding section, Section 5.5, we will describe how the power of the incident laser light of a spot can be determined by using the Poynting vector.

### 5.1 Plane waves and the electromagnetic field

Let  $\mathbf{k}$  be some real vector in cartesian space. A plane perpendicular to  $\mathbf{k}$  is given by

$$\mathbf{k} \cdot \mathbf{r} = \text{constant}. \quad (5.1)$$

A sinusoidally varying function with frequency  $\omega$  of time and position,  $\mathbf{G}(\mathbf{r}, t)$ , given by

$$\mathbf{G}(\mathbf{r}, t) = \mathbf{A}e^{i(\mathbf{k} \cdot \mathbf{r} \mp \omega t)}, \quad (5.2)$$

with  $\mathbf{A}$  a (complex) vector independent of  $\mathbf{r}$ , is called a (harmonic) *plane wave*, since  $\mathbf{G}(\mathbf{r})$  is constant over every plane defined by (5.1). The vector  $\mathbf{k} = (k_x, k_y, k_z)^T$  is called the *wave vector* and its length  $k = |\mathbf{k}| = \frac{2\pi}{\lambda}$ , with  $\lambda$  the wave length, is called the *wave number*. The time dependency will henceforth always be omitted.

In case there are  $m$  plane waves propagating in the same isotropic, homogeneous medium, each having amplitude  $\mathbf{A}_j$  and (complex) wave vector  $\mathbf{k}_j$

$$\mathbf{G}_j = \mathbf{A}_j e^{i\mathbf{k}_j \cdot \mathbf{r}}, \quad 1 \leq j \leq m, \quad (5.3)$$

the resultant field is given by the superposition

$$\mathbf{G} = \sum_{j=1}^m \mathbf{A}_j e^{i\mathbf{k}_j \cdot \mathbf{r}} \quad (5.4)$$

The squared amplitude of every component of the resultant field  $\mathbf{G}$  can easily be calculated with the aid of the equality

$$|A|^2 = (Ae^{i\mathbf{k} \cdot \mathbf{r}})(Ae^{i\mathbf{k} \cdot \mathbf{r}})^*. \quad (5.5)$$

For example, if  $m = 2$ , the squared amplitude of the  $x$ -component of  $\mathbf{A}$  is

$$\begin{aligned} |A_x|^2 &= (A_{1x}e^{i\mathbf{k}_1 \cdot \mathbf{r}} + A_{2x}e^{i\mathbf{k}_2 \cdot \mathbf{r}})(A_{1x}e^{i\mathbf{k}_1 \cdot \mathbf{r}} + A_{2x}e^{i\mathbf{k}_2 \cdot \mathbf{r}})^* \\ &= |A_{1x}|^2 + |A_{2x}|^2 + A_{1x}A_{2x}^*e^{i(\mathbf{k}_1 - \mathbf{k}_2) \cdot \mathbf{r}} + A_{2x}A_{1x}^*e^{i(\mathbf{k}_2 - \mathbf{k}_1) \cdot \mathbf{r}} \\ &= |A_{1x}|^2 + |A_{2x}|^2 + 2|A_{1x}||A_{2x}|\cos[(\mathbf{k}_1 - \mathbf{k}_2) \cdot \mathbf{r} + \phi], \end{aligned} \quad (5.6)$$

where

$$\phi = \arg(A_{1x}A_{2x}^*). \quad (5.7)$$

From (5.6) one can easily see that the addition of two plane waves travelling in opposite directions yields a resultant field of which the amplitude varies sinusoidally as a function of position. Such a field is called a *standing wave*.

Let us consider a homogeneous isotropic material with (possibly complex) relative permittivity  $\epsilon$  and refractive index  $n$ . In Section 4.3 we have shown that for a time-harmonic electromagnetic field the following equations hold inside the material:

$$\nabla \times \mathbf{E} = i\omega\mu_0\mathbf{H}, \quad (5.8)$$

$$\nabla \times \mathbf{H} = -i\omega\epsilon_0\epsilon\mathbf{E}. \quad (5.9)$$

We have also shown that the components of the electromagnetic field satisfy the scalar Helmholtz equations:

$$\omega^2\epsilon_0\epsilon\mu_0\mathbf{E} + \Delta\mathbf{E} = \mathbf{0}, \quad (5.10)$$

$$\omega^2\epsilon_0\epsilon\mu_0\mathbf{H} + \Delta\mathbf{H} = \mathbf{0}. \quad (5.11)$$

Consider an electric field  $\mathbf{E}$  of the form

$$\mathbf{E}(\mathbf{r}) = \mathbf{A}e^{i\mathbf{k}\cdot\mathbf{r}}. \quad (5.12)$$

Because of  $\nabla \cdot (\epsilon_0\epsilon\mathbf{E}) = 0$ , the vector  $\mathbf{A}$  must satisfy:

$$\mathbf{A} \cdot \mathbf{k} = 0. \quad (5.13)$$

From (5.8) it follows that

$$\mathbf{H}(\mathbf{r}) = \frac{\mathbf{k}}{\omega\mu_0} \times \mathbf{A}e^{i\mathbf{k}\cdot\mathbf{r}}, \quad (5.14)$$

so that we can conclude that

$$\mathbf{H} \cdot \mathbf{k} = \mathbf{E} \cdot \mathbf{H} = 0. \quad (5.15)$$

An electric field of the form (5.12) satisfies (5.10) provided that

$$k_x^2 + k_y^2 + k_z^2 = \omega^2\epsilon_0\epsilon\mu_0 = k^2n^2. \quad (5.16)$$

In an optical system in which the light propagates mainly in the  $z$ -direction (the  $z$ -axis is then called the *optical axis*), plane waves whose wave vector has real  $x$ - and  $y$ -components are of most interest. The reason is that, as we will show in Section 5.2, any field that propagates mainly in the direction of the  $z$ -axis can be expanded in an integral over such plane waves. In case of an absorbing medium,  $\epsilon$  and thus  $n$ , will be complex. As a consequence, it follows from (5.16) that the  $z$ -component of the wave vector  $\mathbf{k}$  must be complex. But even when the material is non-absorbing, i.e.  $\epsilon$  is real,  $k_z$  can be complex. Indeed, when  $k_x^2 + k_y^2 > \omega^2\epsilon_0\epsilon\mu_0$ , it follows from (5.16) that then

$$k_z = \pm \sqrt{\omega^2\epsilon_0\epsilon\mu_0 - k_x^2 - k_y^2}, \quad (5.17)$$

will be purely imaginary<sup>1</sup>. A plane wave of which the  $z$ -component of its wave vector is complex is therefore exponentially damped in the  $z$ -direction. Such a wave is called *evanescent* in the direction in which its amplitude decreases exponentially.

<sup>1</sup>In the following we will always choose the branch of the complex square root  $\sqrt{z}$  such that the cut is along the negative real axis and such that for positive real  $z$ :  $\sqrt{z} > 0$  and  $\sqrt{-z} = +i\sqrt{z}$

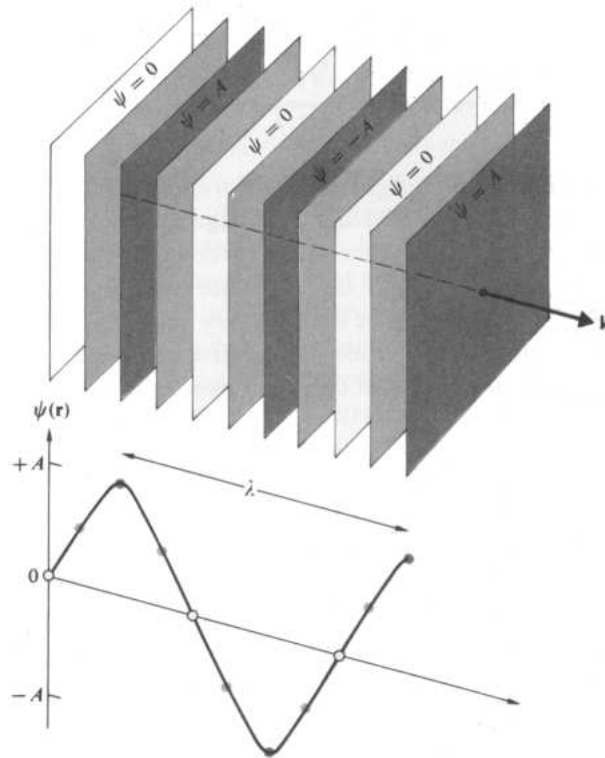


Figure 5.1: A plane wave with real wave vector  $k$  and real amplitude  $A$ .

## 5.2 Expansion into plane waves

Because in our model the  $z$ -axis is chosen as the optical and hence the waves propagate primarily in the  $z$ -direction, we consider an electromagnetic field radiated by sources within a half-space  $z < 0$ . We will now derive the electromagnetic field in the half-space  $z > 0$  filled with a homogeneous isotropic medium with relative (complex) dielectric permittivity  $\epsilon$  and (complex) index of refraction  $n$ , assuming the field in the plane  $z = 0$  to be known. According to (5.10) and (5.11), every component  $U$  of the electromagnetic field in  $z > 0$  satisfies the scalar Helmholtz equation

$$k^2 n^2 U + \Delta U = 0. \quad (5.18)$$

We will show that  $U$  in  $z > 0$  is given by:

$$U(x, y, z) = \iint_{-\infty}^{\infty} e^{2\pi i(xf_x + yf_y) + iz\sqrt{k^2 n^2 - 4\pi^2(f_x^2 + f_y^2)}} \times \mathcal{F}(U)(f_x, f_y, 0) df_x df_y, \quad (5.19)$$

where  $\mathcal{F}(U)(f_x, f_y, 0)$  denotes the Fourier transform of  $U$  with respect to  $x$  and  $y$  in the plane  $z = 0$  and where the so called spatial frequencies  $f_x, f_y$  can be any real number. From (5.19) it follows that each component of the electromagnetic field in  $z > 0$  can be written as the superposition of plane waves having various wave vectors. The wave vectors of these plane waves are given by

$$\mathbf{k} = \begin{pmatrix} k_x \\ k_y \\ k_z \end{pmatrix} = \begin{pmatrix} 2\pi f_x \\ 2\pi f_y \\ \sqrt{k^2 n^2 - 4\pi^2(f_x^2 + f_y^2)} \end{pmatrix}. \quad (5.20)$$

Note that in case of an absorbing medium, i.e.  $n^2$  is complex, the amplitudes of all plane waves decrease exponentially in the positive  $z$ -direction. When there is no absorption, i.e. when  $n^2$  is real, plane waves for

which  $4\pi^2(f_x^2 + f_y^2) > k^2n^2$  also have exponentially decreasing amplitude, because they are evanescent in the positive  $z$ -direction. But, the contribution of the evanescent waves to the field in  $z > 0$  already becomes negligible after short distances in the positive  $z$ -direction.

Equation (5.19) can be derived from equation (5.18) by first taking the Fourier transform of  $U$  with respect to  $x$  and  $y$ :

$$\mathcal{F}(U)(f_x, f_y, z) = \iint_{-\infty}^{\infty} e^{-2\pi i(xf_x + yf_y)} U(x, y, z) dx dy. \quad (5.21)$$

The inverse Fourier transform yields:

$$U(x, y, z) = \iint_{-\infty}^{\infty} e^{2\pi i(xf_x + yf_y)} \mathcal{F}(U)(f_x, f_y, z) df_x df_y. \quad (5.22)$$

After substitution in (5.18) we get for every  $(f_x, f_y)$  the following differential equation for  $z \rightarrow \mathcal{F}(U)(f_x, f_y, z)$ :

$$[k^2n^2 - 4\pi^2(f_x^2 + f_y^2)]\mathcal{F}(U)(f_x, f_y, z) + \frac{\partial^2 \mathcal{F}(U)(f_x, f_y, z)}{\partial z^2} = 0, \quad (5.23)$$

whose general solution is:

$$\mathcal{F}(U)(f_x, f_y, z) = A(f_x, f_y)e^{iz\sqrt{k^2n^2 - 4\pi^2(f_x^2 + f_y^2)}} + B(f_x, f_y)e^{-iz\sqrt{k^2n^2 - 4\pi^2(f_x^2 + f_y^2)}}, \quad (5.24)$$

where  $A$  and  $B$  are still to be determined. Because the time dependency is implicitly given by  $e^{-i\omega t}$ , the first term at the right-hand side of (5.24) represents a wave that propagates or is exponentially decreasing in the positive  $z$ -direction, whereas the second term represents a wave that propagates or is exponentially decreasing in the negative  $z$ -direction. Recalling that we assumed the sources to exist only in  $z < 0$ , we conclude that  $B = 0$ . It now follows that  $A$  can be expressed in the Fourier transform of the (known) electromagnetic field at  $z = 0$ :

$$A(f_x, f_y) = \mathcal{F}(U)(f_x, f_y, 0). \quad (5.25)$$

In combination with (5.22) this yields equation (5.19).

### 5.3 Polarization and the Fresnel coefficients

Let us now consider two half spaces  $z < 0$  and  $z > 0$ , both filled with homogeneous, isotropic materials with (complex) indices of refraction  $n_1$  and  $n_2$ , respectively. In  $z > 0$ , an electromagnetic plane wave, with field components given by (5.12) and (5.14), and with  $\mathbf{k}$  satisfying (5.16), is generated by a source at  $z \rightarrow +\infty$ . This plane wave is incident on the plane  $z = 0$ .

We will first discuss the polarization of such an electromagnetic plane wave. For convenience assume that the wave vector only has a  $z$ -component:  $\mathbf{k} = (0, 0, k_z)^T$  with  $k_z = kn_1$  (this is a complex number if the material in  $z > 0$  is absorbing, i.e.  $n_1$  is complex). (5.15) implies that the vector  $\mathbf{A}$  then only has  $x$ - and  $y$ -components:  $\mathbf{A} = (A_x, A_y, 0)^T$ . If we write  $A_x = |A_x|e^{i\phi_x}$  and  $A_y = |A_y|e^{i\phi_y}$  then for the components of the physical (and thus real) electric field strength holds:

$$\begin{aligned} \mathcal{E}(\mathbf{r}, t) &= \text{Re} [\mathbf{E}(\mathbf{r})e^{-i\omega t}] \\ &= |A_x| \cos(\omega t - k_z z - \phi_x) \mathbf{e}_x + |A_y| \cos(\omega t - k_z z - \phi_y) \mathbf{e}_y. \end{aligned} \quad (5.26)$$

where  $\mathbf{e}_x = (1, 0, 0)^T$  and  $\mathbf{e}_y = (0, 1, 0)^T$ .

From (5.26) it is easy to derive that, when  $\phi_x = \phi_y$  or  $\phi_x = \phi_y \pm \pi$ , the electric field vector  $\mathcal{E}$  is always parallel to the vector  $|A_x|\mathbf{e}_x + |A_y|\mathbf{e}_y$  or  $|A_x|\mathbf{e}_x - |A_y|\mathbf{e}_y$ , its value oscillating between  $-\sqrt{|A_x|^2 + |A_y|^2}$  and  $\sqrt{|A_x|^2 + |A_y|^2}$ . The plane wave is then said to be *linearly polarized* along either vector. When  $|A_x| = |A_y|$  and  $\phi_x = \phi_y \pm \frac{\pi}{2}$ , the tip of the electric vector  $\mathcal{E}$  traces a circular path and the plane wave is called *circularly polarized*. For general  $A_x$  and  $A_y$  the endpoint of the electric field vector describes an

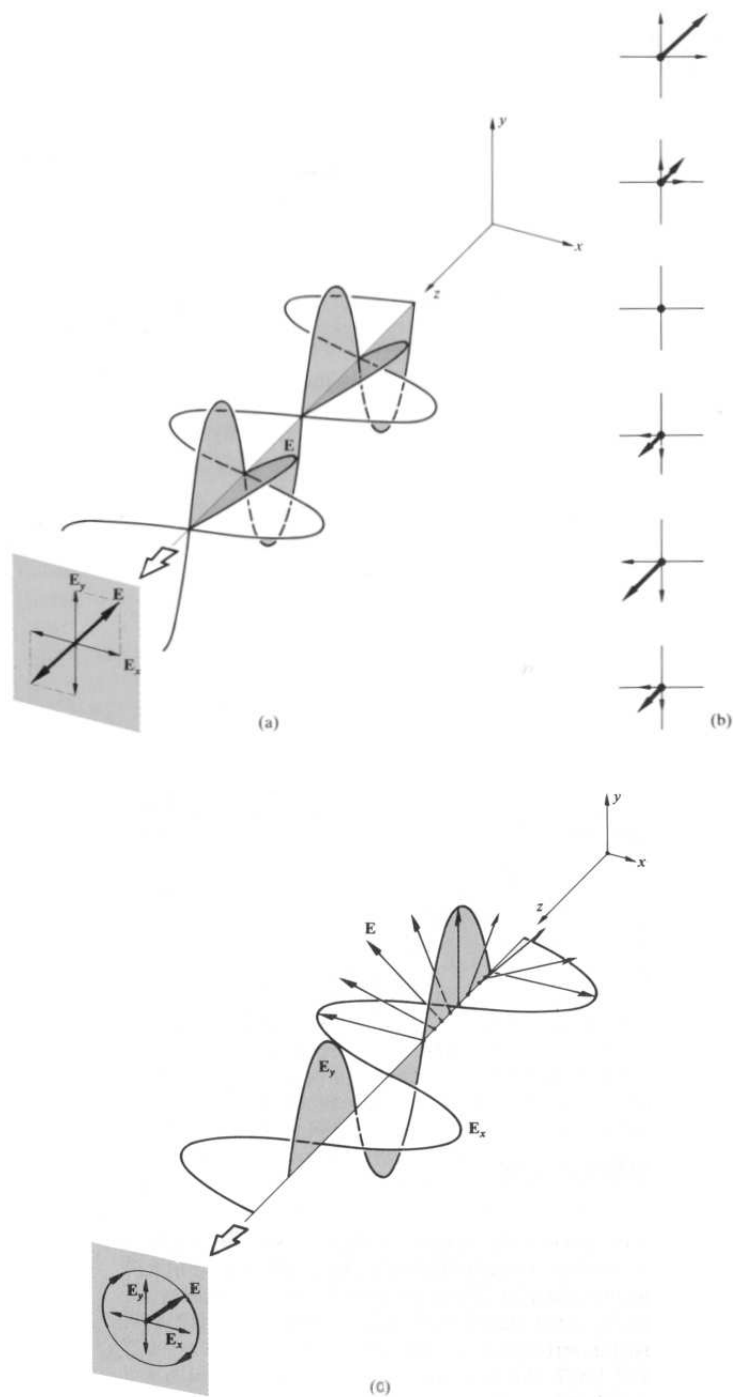


Figure 5.2: (a) A linearly polarized plane wave. Its amplitude oscillates through zero (b). If the wave is circularly polarized (c), the tip of the electric vector traces a circular path.

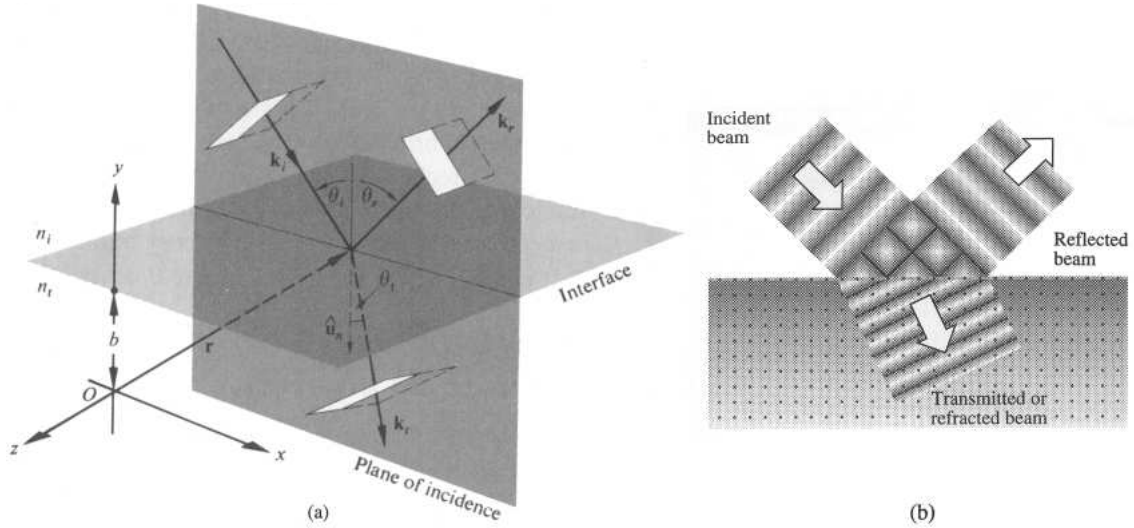


Figure 5.3: Reflection and refraction of a single plane wave with real wave vector  $\mathbf{k}$  and real amplitude  $\text{normbold}A$  on a straight surface.

ellipse. The general state of polarization of a plane wave is therefore called *elliptical polarization*. If for an observer looking in the direction of where the wave comes from, the electric vector rotates clockwise, we have *right-hand elliptical polarization*, when it rotates counter-clockwise, the polarization is called *left-hand elliptical polarization*.

It is clear that an arbitrary elliptically polarized plane wave can always be written as the superposition of two linearly polarized plane waves with mutually perpendicular directions of polarization:

$$\mathbf{A} = \begin{pmatrix} A_x \\ A_y \\ 0 \end{pmatrix} = \begin{pmatrix} A_x \\ 0 \\ 0 \end{pmatrix} + \begin{pmatrix} 0 \\ A_y \\ 0 \end{pmatrix}. \quad (5.27)$$

Moreover, an elliptically polarized plane wave can also be written as the superposition of right-hand and left-hand circular polarized plane waves:

$$\mathbf{A} = \begin{pmatrix} A_x \\ A_y \\ 0 \end{pmatrix} = \frac{A_x - iA_y}{2} \begin{pmatrix} 1 \\ i \\ 0 \end{pmatrix} + \frac{A_x + iA_y}{2} \begin{pmatrix} 1 \\ -i \\ 0 \end{pmatrix}. \quad (5.28)$$

We will now consider a linearly polarized plane wave in  $z > 0$  that is incident on the plane  $z = 0$ , the *interface*. Besides a reflected plane wave in  $z > 0$  there will also be a transmitted electromagnetic plane wave in  $z < 0$ . Let us denote the wave vectors of the incident, reflected and transmitted electromagnetic plane waves by  $\mathbf{k}_1^-$ ,  $\mathbf{k}_1^+$  and  $\mathbf{k}_2^-$  respectively. Without loss of generality we assume  $k_y = 0$ , hence the *plane of incidence* coincides with the plane  $y = 0$ . If we let

$$k_{jz} = \sqrt{k^2 n_j^2 - k_x^2}, \quad j = 1, 2, \quad (5.29)$$

we can write

$$\mathbf{k}_j^\pm = (k_x, 0, \pm k_{jz}), \quad j = 1, 2. \quad (5.30)$$

Let us assume that  $\mathbf{E}$  points in the positive  $y$ -direction. This situation is called *parallel* or simply *P-polarization*. If on the other hand  $\mathbf{H}$  points in the positive  $y$ -direction, the polarization is called *S-polarization*, because  $\mathbf{E}$  is now perpendicular to the plane  $y = 0$  (*Senkrecht* is the German word for perpendicular).

We will now first assume the incident electromagnetic plane wave to be S-polarized and having an amplitude of 1. Then we write

$$\begin{aligned}\mathbf{E}(\mathbf{r}) &= \begin{pmatrix} 0 \\ 1 \\ 0 \end{pmatrix} e^{i\mathbf{k}_1^- \cdot \mathbf{r}} + r \begin{pmatrix} 0 \\ 1 \\ 0 \end{pmatrix} e^{i\mathbf{k}_1^+ \cdot \mathbf{r}}, & z > 0, \\ \mathbf{E}(\mathbf{r}) &= t \begin{pmatrix} 0 \\ 1 \\ 0 \end{pmatrix} e^{i\mathbf{k}_2^- \cdot \mathbf{r}}, & z < 0,\end{aligned}\tag{5.31}$$

where  $r$  denotes the *amplitude reflection coefficient* and  $t$  the *amplitude transmission coefficient*. For the magnetic field we then have according to (5.14):

$$\begin{aligned}\mathbf{H}(\mathbf{r}) &= \frac{1}{\omega\mu_0} \begin{pmatrix} k_{1z} \\ 0 \\ k_x \end{pmatrix} e^{i\mathbf{k}_1^- \cdot \mathbf{r}} + \frac{r}{\omega\mu_0} \begin{pmatrix} -k_{1z} \\ 0 \\ k_x \end{pmatrix} e^{i\mathbf{k}_1^+ \cdot \mathbf{r}}, & z > 0, \\ \mathbf{H}(\mathbf{r}) &= \frac{t}{\omega\mu_0} \begin{pmatrix} k_{2z} \\ 0 \\ k_x \end{pmatrix} e^{i\mathbf{k}_2^- \cdot \mathbf{r}}, & z < 0.\end{aligned}\tag{5.32}$$

The tangential component of the electric field,  $E_y$ , and of the magnetic field,  $H_x$ , should be continuous on the interface. Due to these requirements the *Fresnel coefficients*  $r$  and  $t$  in case of S-polarization are found to be:

$$r = \frac{k_{1z} - k_{2z}}{k_{1z} + k_{2z}},\tag{5.33}$$

$$t = 1 + r = \frac{2k_{1z}}{k_{1z} + k_{2z}}.\tag{5.34}$$

In case the electromagnetic field is P-polarized, the Fresnel coefficients can be found by setting the amplitude of  $H_y$  equal to 1:

$$\begin{aligned}\mathbf{H}(\mathbf{r}) &= \begin{pmatrix} 0 \\ 1 \\ 0 \end{pmatrix} e^{i\mathbf{k}_1^- \cdot \mathbf{r}} + r \begin{pmatrix} 0 \\ 1 \\ 0 \end{pmatrix} e^{i\mathbf{k}_1^+ \cdot \mathbf{r}}, & z > 0, \\ \mathbf{H}(\mathbf{r}) &= t \begin{pmatrix} 0 \\ 1 \\ 0 \end{pmatrix} e^{i\mathbf{k}_2^- \cdot \mathbf{r}}, & z < 0.\end{aligned}\tag{5.35}$$

For the electric field then holds:

$$\begin{aligned}\mathbf{E}(\mathbf{r}) &= -\frac{1}{\omega n_j^2} \begin{pmatrix} k_{1z} \\ 0 \\ k_x \end{pmatrix} e^{i\mathbf{k}_1^- \cdot \mathbf{r}} - \frac{r}{\omega n_j^2} \begin{pmatrix} -k_{1z} \\ 0 \\ k_x \end{pmatrix} e^{i\mathbf{k}_1^+ \cdot \mathbf{r}}, & z > 0, \\ \mathbf{E}(\mathbf{r}) &= -\frac{t}{\omega n_j^2} \begin{pmatrix} k_{2z} \\ 0 \\ k_x \end{pmatrix} e^{i\mathbf{k}_2^- \cdot \mathbf{r}}, & z < 0.\end{aligned}\tag{5.36}$$

The continuity of the tangential components of the electric and magnetic fields ( $H_x$  and  $E_y$ ) now implies that the Fresnel coefficients in case of P-polarization are given by

$$r = \frac{\frac{k_{1z}}{n_1^2} - \frac{k_{2z}}{n_2^2}}{\frac{k_{1z}}{n_1^2} + \frac{k_{2z}}{n_2^2}},\tag{5.37}$$

$$t = 1 + r = \frac{2\frac{k_{1z}}{n_1^2}}{\frac{k_{1z}}{n_1^2} + \frac{k_{2z}}{n_2^2}}.\tag{5.38}$$

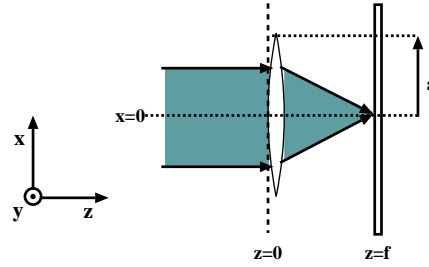


Figure 5.4: A beam of light incident on an objective lens with radius  $a$ . The incident field at  $z = 0$  is assumed to be known. The optical disk lies in the focal plane of the lens at  $z = f$ .

## 5.4 Focusing of a beam by a lens

Let us consider a beam of light that is incident on a positive aberration-free lens with radius  $a$  as shown in Figure 5.4. Consider a field components  $U$ , e.g. the  $E_x$ -component, and assume that it is given in a plane directly in front of the lens. The finite dimensions of the lens can be described by a *pupil function*  $P_a(x, y)$  defined by:

$$P_a(x, y) = \begin{cases} 1 & \sqrt{x^2 + y^2} \leq a, \\ 0 & \sqrt{x^2 + y^2} > a. \end{cases} \quad (5.39)$$

Apart from a constant phase, the field distribution  $U_f$  at the focal plane  $z = f$  is then given by [5]:

$$U_f(u, v) = \iint_{-\infty}^{\infty} U_l(x, y) P_a(x, y) \exp -2\pi i \left( \frac{xu}{\lambda f} + \frac{yv}{\lambda f} \right) dx dy. \quad (5.40)$$

Hence the field distribution  $U_f$  is (proportional to) the two-dimensional Fourier transform of the part of the incident field that passes through the lens, evaluated at spatial frequencies given by  $f_x = \frac{u}{\lambda f}$  and  $f_y = \frac{v}{\lambda f}$ .

**Example 1** Suppose that the incident field is a plane wave with amplitude 1:

$$U_l(x, y) = 1. \quad (5.41)$$

By using (5.40) it follows that

$$\begin{aligned} U_f(r) &= \iint_{-\infty}^{\infty} 1 \cdot P_a(x, y) e^{-2\pi i (f_x x + f_y y)} dx dy \\ &= \frac{\pi a^2}{i \lambda f} \left[ 2 \frac{J_1(akr/f)}{akr/f} \right], \end{aligned} \quad (5.42)$$

where  $r = \sqrt{u^2 + v^2}$  and  $J_1$  is the Bessel function (of the first kind) of order one defined by

$$J_1(\mu) = \frac{1}{2\pi i} \int_0^{2\pi} e^{i(\nu + \mu \cos \nu)} d\nu. \quad (5.43)$$

The related intensity distribution  $I$  can be written as

$$I(r) = \left( \frac{\pi a^2}{\lambda f} \right)^2 \left[ 2 \frac{J_1(akr/f)}{akr/f} \right]^2. \quad (5.44)$$

This intensity distribution is referred to as the *Airy pattern*. See Figure 5.5 (a).

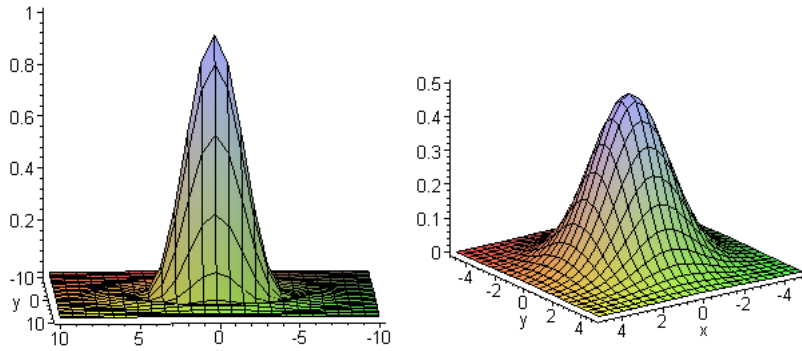


Figure 5.5: An Airy pattern (left) and a Gaussian distribution (right).

**Example 2** In this second example we assume the incident field to be a Gaussian distribution:

$$\mathbf{U}_l(x, y) = e^{-\frac{x^2}{\sigma_x^2} - \frac{y^2}{\sigma_y^2}}. \quad (5.45)$$

When the parameters  $\sigma_x^2$  and  $\sigma_y^2$  are chosen such that the extent of the incident field is much smaller than the lens aperture, the factor  $P_a(x, y)$  in (5.40) may be neglected. Then

$$U_f(u, v) = \iint_{-\infty}^{\infty} U_l(x, y) e^{-2\pi i(f_x x + f_y y)} dx dy. \quad (5.46)$$

By using the following equality with  $\alpha$  an arbitrary constant:

$$\begin{aligned} \int_{-\infty}^{\infty} e^{-\alpha x^2} e^{-2\pi i x f_x} dx &= \int_{-\infty}^{\infty} e^{-\alpha \left(x + \frac{\pi i f_x}{\alpha}\right)^2} e^{-\frac{\pi^2 f_x^2}{\alpha}} dx \\ &= \frac{1}{2} e^{-\frac{\pi^2 f_x^2}{\alpha}} \int_{-\infty}^{\infty} e^{-\alpha \hat{x}^2} d\hat{x} \\ &= \frac{1}{2} \sqrt{\frac{\pi}{\alpha}} e^{-\frac{\pi^2 f_x^2}{\alpha}}, \end{aligned} \quad (5.47)$$

it can then be seen that in case the field distribution right in front of the lens is given by (5.45), the field distribution  $U_f$  in the focal plane will also be a Gaussian distribution.

The Diffract program by Mansuripur et al. [24] can be used to compute the spot focused on the disk. Diffract is a program for calculating diffraction patterns from various optical components that are large with respect to the wavelength of the light. It is an interactive program which allows the user to choose the optical devices and relevant parameters.

By choosing a linearly polarized plane wave (or a Gaussian beam) that is focused by an aberration-free positive lens an almost (but never perfectly!) linearly polarized spot is obtained. The tangential components of the electromagnetic field in the focal plane are calculated with Diffract. This calculation is done in 'quasi-vectorial' way, which means that the rotation of the electric vector upon diffraction is taken into account. Diffract returns the values of the tangential components of the electromagnetic field in the focal plane on a square equidistant grid of points of dimensions defined by the user.

When the field that is incident on the lens is assumed to be linearly polarized, it will at most be predominantly linearly polarized. The spot is called *predominantly TE-polarized* if  $E_y^i$  is the predominant component of the incident electric field. If  $H_y^i$  is the predominant component of the incident magnetic field the field is said to be *predominantly TM-polarized*.

## 5.5 The power of the laser beam

Let us consider a linearly polarized parallel laser beam with wave vector  $\mathbf{k} = (0, 0, -k_z)^T$  in air ( $\epsilon = 1$ ) that is incident on an objective lens. From (5.16) it follows that for this beam  $k = \omega^2 \epsilon_0 \mu_0$ . Using (5.14) we can express the magnetic field component in terms of the electric field components ( $\nabla = i\mathbf{k}$ ):

$$\mathbf{H} = \sqrt{\frac{\epsilon_0}{\mu_0}} \begin{pmatrix} E_y \\ -E_x \\ 0 \end{pmatrix}. \quad (5.48)$$

The time-average energy flow (per unit area) is in the  $z$ -direction and is given by:

$$\langle \mathbf{S} \rangle = \frac{1}{2} \sqrt{\frac{\epsilon_0}{\mu_0}} (|E_x|^2 + |E_y|^2) \mathbf{e}_z, \quad (5.49)$$

where  $\mathbf{e}_z$  denotes the unit vector in the  $z$ -direction. For a Gaussian beam that is polarized along the  $x$ -axis:

$$E_x = A_x e^{-\frac{\alpha(x-x_0)^2 + \beta(y-y_0)^2}{\omega^2}}, \quad E_y = 0, \quad (5.50)$$

the time-average energy flow per unit area becomes

$$\langle \mathbf{S} \rangle = \frac{1}{2} \sqrt{\frac{\epsilon_0}{\mu_0}} |A_x|^2 e^{-2\frac{\alpha(x-x_0)^2 + \beta(y-y_0)^2}{\omega^2}} \mathbf{e}_z. \quad (5.51)$$

This is also called the intensity of the light beam.

Integration of this time-averaged Poynting vector over the area of a cross-section perpendicular to the beams propagation direction, gives us the total (time-averaged) power  $P$  of the laser beam:

$$P = \oint_S \langle \mathbf{S} \rangle \cdot d\mathbf{a} \quad (5.52)$$

## Chapter 6

# Diffraction at periodic gratings

For clarity we will begin this chapter with the description of the model of the scattering of an incident plane wave. The first 5 sections of this chapter will be dedicated to this fundamental problem. Then, in Section 6.6, we shall explain how the diffraction problem can be generalized to an arbitrary incoming focused spot. Finally, in Section 6.7 the numerical sampling of the incident spot will be discussed.

### 6.1 Derivation of the grating problem in a unit cell

In many diffraction problems, the distance of the primary sources, that emit the incident electromagnetic field, to the scattering bodies is so large, that these sources can be considered to be at infinite distance. By definition, the *incident field* is the field that is emitted by the sources and would be present in the absence of the scattering bodies. The complex electric and magnetic components of this field will be denoted by  $\mathbf{E}^i$  and  $\mathbf{H}^i$  and can be considered to be known. The presence of the scattering bodies induces an additional electromagnetic field, called the *scattered field*, which will be denoted by  $\mathbf{E}^s$  and  $\mathbf{H}^s$ . The total electromagnetic field due to the primary sources and the scattering objects is the sum of the incident and scattered field:

$$\mathbf{E} = \mathbf{E}^i + \mathbf{E}^s, \quad (6.1)$$

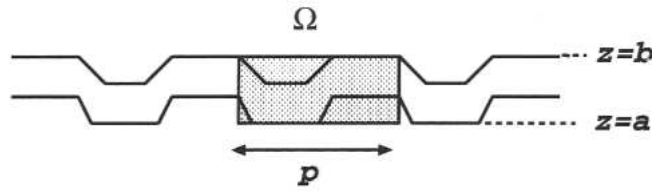
$$\mathbf{H} = \mathbf{H}^i + \mathbf{H}^s. \quad (6.2)$$

As has been explained earlier, the scattered field is induced by oscillating atomic dipole moments within the scattering object. It is a priori unknown.

A periodic grating is an object that periodically disturbs the amplitude and the phase of an incoming field. We restrict ourselves to calculating the electromagnetic field in points of which the distance to the grating is sufficiently small so that the grating can be considered to be infinitely wide. With respect to a cartesian coordinate system  $(x, y, z)$  such that the  $z$ -axis is the optical axis of the illumination system, the grating is assumed to be  $p$ -periodic in the  $x$ -direction and invariant under translations parallel to the  $y$ -axis. The grating consists of a medium of which the complex relative electric permittivity  $\epsilon$  may be a function of  $(x, z)$ , but must be independent of  $y$ . We assume that two planes  $z = a$  and  $z = b$  exist that bound the grating in such a way that the half spaces  $z < a$  and  $z > b$  are filled with homogeneous isotropic media with relative electric permittivity  $\epsilon_l$  and  $\epsilon_u$  respectively. Furthermore,  $\epsilon_u$  is taken to be real, hence the medium in  $z > b$  is assumed to be non-absorbing. Let the two-dimensional unit cell  $\Omega$  be the region in the plane  $y = \text{constant}$  defined by

$$\Omega = \left\{ (x, z) \mid -\frac{p}{2} < x < \frac{p}{2}, a < z < b \right\}. \quad (6.3)$$

The region  $\Omega$  is one period wide and  $a < b$  are chosen such that  $\Omega$  contains all non-flat boundary interfaces and all regions where the permittivity  $\epsilon$  is not homogeneous but is otherwise as small as possible. We call  $\Omega$  a *unit cell* of the periodic grating.

Figure 6.1: The geometry of a  $p$ -periodic cell

Let the incident plane wave have wave vector  $\mathbf{k} = (k_x, k_y, k_z)^T$ . The components  $k_x$  and  $k_y$  of the wave vector are real and

$$k_z = -\sqrt{\omega^2 \epsilon_0 \epsilon_u \mu_0 - k_x^2 - k_y^2}. \quad (6.4)$$

As in Section 5.1, (5.12) and (5.14), we will denote the electromagnetic field of the incident plane wave by

$$\mathbf{E}^i(\mathbf{r}) = \mathbf{A}^i e^{i\mathbf{k} \cdot \mathbf{r}}, \quad (6.5)$$

$$\mathbf{H}^i(\mathbf{r}) = \frac{\mathbf{k}}{\omega \mu_0} \times \mathbf{E}^i(\mathbf{r}), \quad (6.6)$$

where the amplitude  $\mathbf{A}^i$  is a complex vector that satisfies

$$\mathbf{k} \cdot \mathbf{A}^i = 0. \quad (6.7)$$

We will first show that the scattered field and the total field are quasi-periodic (Floquet's theorem). We define the piece-wise constant relative permittivity  $\tilde{\epsilon}$  by

$$\tilde{\epsilon} = \begin{cases} \epsilon_l & z < \frac{a+b}{2}, \\ \epsilon_u & z > \frac{a+b}{2}. \end{cases} \quad (6.8)$$

The true permittivity  $\epsilon$  only differs from  $\tilde{\epsilon}$  within the strip  $a < z < b$ . For convenience we now redefine the incident field as the field that would be present if there were only two half-spaces:  $z < (a+b)/2$  with permittivity  $\epsilon_l$  and  $z > (a+b)/2$  with permittivity  $\epsilon_u$ . In  $z > (a+b)/2$  the incident field thus consists of the sum of the incident plane wave (6.5), (6.6) and of the field reflected at the (virtual) surface  $z = (a+b)/2$ . In  $z < (a+b)/2$  there is only the transmitted field. By definition, the incident field satisfies *for all positions*  $\mathbf{r}$ :

$$\nabla \times \mathbf{E}^i(\mathbf{r}) = i\omega \mu_0 \mathbf{H}^i(\mathbf{r}), \quad (6.9)$$

$$\nabla \times \mathbf{H}^i(\mathbf{r}) = -i\omega \epsilon_0 \tilde{\epsilon} \mathbf{E}^i(\mathbf{r}). \quad (6.10)$$

It is easy to determine  $\mathbf{E}^i$  and  $\mathbf{H}^i$  using the Fresnel formulae of Section 5.3. Since the total electromagnetic field satisfies (4.47) and (4.48), the scattered field ( $\mathbf{E}^s, \mathbf{H}^s$ ) defined by (6.1) and (6.2) satisfies:

$$\nabla \times \mathbf{E}^s = i\omega \mu_0 \mathbf{H}^s, \quad (6.11)$$

$$\nabla \times \mathbf{H}^s = -i\omega \epsilon_0 \epsilon \mathbf{E}^s + i\omega (\tilde{\epsilon} - \epsilon) \mathbf{E}^i. \quad (6.12)$$

From (6.12) it follows that the scattered field is generated by a dipole distribution concentrated in the strip  $a < z < b$  with magnitude  $\mathbf{P} = (\tilde{\epsilon} - \epsilon) \mathbf{E}^i$ . Recalling that the relative electric permittivity  $\epsilon = \epsilon(x, z)$  of the grating is  $p$ -periodic with respect to  $x$  and independent of  $y$  it follows that every component  $U$  of  $\mathbf{P}$  is *quasi-periodic* with respect to  $x$

$$U(x+p, y, z) = U(x, y, z) e^{ik_x p}, \quad (6.13)$$

and harmonic in  $y$

$$U(x, y, z) = U(x, z) e^{ik_y y}. \quad (6.14)$$

Hence, in particular

$$\frac{\partial U}{\partial y} = ik_y U. \quad (6.15)$$

Since the differential operator on the left-hand side of (6.12) maps quasi-periodic electric fields onto quasi-periodic dipole distributions, it follows using the uniqueness of the solution of the diffraction problem, that the scattered field and hence the total field also have these properties.

Substitution of (6.15) in the homogeneous Maxwell equations (4.47) and (4.48) for the partial derivatives with respect to  $y$  of all components of the total field gives:

$$ik_y E_z - \frac{\partial E_y}{\partial z} = i\omega\mu_0 H_x, \quad (6.16)$$

$$\frac{\partial E_z}{\partial x} - \frac{\partial E_x}{\partial z} = -i\omega\mu_0 H_y, \quad (6.17)$$

$$\frac{\partial E_y}{\partial x} - ik_y E_x = i\omega\mu_0 H_z, \quad (6.18)$$

and

$$ik_y H_z - \frac{\partial H_y}{\partial z} = -i\omega\epsilon_0 \epsilon E_x, \quad (6.19)$$

$$\frac{\partial H_z}{\partial x} - \frac{\partial H_x}{\partial z} = i\omega\epsilon_0 \epsilon E_y, \quad (6.20)$$

$$\frac{\partial H_y}{\partial x} - ik_y H_x = -i\omega\epsilon_0 \epsilon E_z. \quad (6.21)$$

Equations (6.16) and (6.20) can be used to express the transverse field components  $E_z$  and  $H_x$  in the axial components  $E_y$  and  $H_y$ . Analogously we can use (6.17) and (6.19) to express  $E_x$  and  $H_z$  in these axial components. This yields

$$E_x = \frac{i}{\omega^2 \epsilon_0 \epsilon \mu_0 - k_y^2} \left( k_y \frac{\partial E_y}{\partial x} - \omega \mu_0 \frac{\partial H_y}{\partial z} \right), \quad (6.22)$$

$$E_z = \frac{i}{\omega^2 \epsilon_0 \epsilon \mu_0 - k_y^2} \left( k_y \frac{\partial E_y}{\partial z} + \omega \mu_0 \frac{\partial H_y}{\partial x} \right), \quad (6.23)$$

$$H_x = \frac{i}{\omega^2 \epsilon_0 \epsilon \mu_0 - k_y^2} \left( \omega \epsilon_0 \epsilon \frac{\partial E_y}{\partial z} + k_y \frac{\partial H_y}{\partial x} \right), \quad (6.24)$$

$$H_z = \frac{i}{\omega^2 \epsilon_0 \epsilon \mu_0 - k_y^2} \left( -\omega \epsilon_0 \epsilon \frac{\partial E_y}{\partial x} + k_y \frac{\partial H_y}{\partial z} \right). \quad (6.25)$$

Substitution of (6.22)-(6.25) into (6.17) and (6.20) yields a coupled system of two differential equations for only  $E_y$  and  $H_y$ :

$$i\omega\epsilon_0\epsilon E_y - \frac{\partial}{\partial x} \left[ \frac{i}{\omega^2 \epsilon_0 \epsilon \mu_0 - k_y^2} \left( -\omega \epsilon_0 \epsilon \frac{\partial E_y}{\partial x} + k_y \frac{\partial H_y}{\partial z} \right) \right] + \frac{\partial}{\partial z} \left[ \frac{i}{\omega^2 \epsilon_0 \epsilon \mu_0 - k_y^2} \left( \omega \epsilon_0 \epsilon \frac{\partial E_y}{\partial z} + k_y \frac{\partial H_y}{\partial x} \right) \right] = 0, \quad (6.26)$$

$$i\omega\mu_0 H_y + \frac{\partial}{\partial x} \left[ \frac{i}{\omega^2 \epsilon_0 \epsilon \mu_0 - k_y^2} \left( k_y \frac{\partial E_y}{\partial z} + \omega \mu_0 \frac{\partial H_y}{\partial x} \right) \right] - \frac{\partial}{\partial z} \left[ \frac{i}{\omega^2 \epsilon_0 \epsilon \mu_0 - k_y^2} \left( k_y \frac{\partial E_y}{\partial x} - \omega \mu_0 \frac{\partial H_y}{\partial z} \right) \right] = 0. \quad (6.27)$$

Note that this system contains  $k_y$  as a parameter. In the next section we will derive the necessary boundary conditions for this coupled system of differential equations on the boundaries of the unit cell  $\Omega$ .

## 6.2 Derivation of the boundary conditions for the unit cell

We will start with the derivation of the boundary conditions at  $x = \pm \frac{p}{2}$ . Since the components of the total field that are tangential to a plane should be continuous across that plane,  $E_y$  and  $E_z$  as well as  $H_y$  and  $H_z$  must be continuous across the planes  $x = \pm \frac{p}{2}$ . Recall from the previous section that the total field is quasi-periodic with respect to  $x$ . Using (6.13) we can then conclude that

$$E_y\left(\frac{p}{2}, y, z\right) = E_y\left(-\frac{p}{2}, y, z\right) e^{ik_x p}, \quad (6.28)$$

$$H_y\left(\frac{p}{2}, y, z\right) = H_y\left(-\frac{p}{2}, y, z\right) e^{ik_x p}, \quad (6.29)$$

and with (6.23) and (6.25)

$$\begin{aligned} & \frac{1}{\omega^2 \epsilon_0 \epsilon\left(\frac{p}{2}, z\right) \mu_0 - k_y^2} \left[ k_y \frac{\partial E_y\left(\frac{p}{2}, y, z\right)}{\partial z} + \omega \mu_0 \frac{\partial H_y\left(\frac{p}{2}, y, z\right)}{\partial x} \right] \\ &= \frac{1}{\omega^2 \epsilon_0 \epsilon\left(-\frac{p}{2}, z\right) \mu_0 - k_y^2} \left( k_y \frac{\partial E_y\left(-\frac{p}{2}, y, z\right)}{\partial z} + \omega \mu_0 \frac{\partial H_y\left(-\frac{p}{2}, y, z\right)}{\partial x} \right) e^{ik_x p}, \end{aligned} \quad (6.30)$$

$$\begin{aligned} & \frac{1}{\omega^2 \epsilon_0 \epsilon\left(\frac{p}{2}, z\right) \mu_0 - k_y^2} \left[ -\omega \epsilon_0 \epsilon\left(\frac{p}{2}, z\right) \frac{\partial E_y\left(\frac{p}{2}, y, z\right)}{\partial x} + k_y \frac{\partial H_y\left(\frac{p}{2}, y, z\right)}{\partial z} \right] \\ &= \frac{1}{\omega^2 \epsilon_0 \epsilon\left(-\frac{p}{2}, z\right) \mu_0 - k_y^2} \left( -\omega \epsilon_0 \epsilon\left(-\frac{p}{2}, z\right) \frac{\partial E_y\left(-\frac{p}{2}, y, z\right)}{\partial x} + k_y \frac{\partial H_y\left(-\frac{p}{2}, y, z\right)}{\partial z} \right) e^{ik_x p}. \end{aligned} \quad (6.31)$$

It remains to specify the boundary conditions on the upper and lower boundaries  $z = b$  and  $z = a$ . This can be achieved by expanding the total field in the half-spaces  $z < a$  and  $z > b$  in terms of plane waves. Restricting ourselves temporarily to only the  $y$ -component of the scattered electric field, we can define a function  $U_y^s(x, z)$  that is periodic in  $x$  and independent of  $y$  such that

$$E_y^s(x, y, z) = U_y^s(x, z) e^{i(k_x x + k_y y)}. \quad (6.32)$$

By using the Fourier series representation of  $U_y^s(x, z)$  we get

$$E_y^s(x, y, z) = \sum_{m=-\infty}^{\infty} \hat{U}_y^s(m, z) e^{\frac{2\pi i x m}{p}} e^{i(k_x x + k_y y)}, \quad (6.33)$$

where  $\hat{U}_y^s(m, z)$  is the  $m$ -th Fourier coefficient of  $x \rightarrow U^s(x, z)$ :

$$\hat{U}_y^s(m, z) = \frac{1}{p} \int_{-\frac{p}{2}}^{\frac{p}{2}} U^s e^{-i(k_x x)} dx. \quad (6.34)$$

We will now use (5.19) to show that we can write the reflected field in  $z > b$  as a superposition of plane waves. (5.19) can be used because the reflected field is propagating in the positive  $z$ -direction. We start by calculating the Fourier transform of (6.33):

$$\begin{aligned} \mathcal{F}(E_y^s)(f_x, f_y, b) &= \iint e^{-2\pi i(x f_x + y f_y)} E_y^s(x, y, b) dx dy \\ &= \sum_{m=-\infty}^{\infty} \hat{U}_y^s(m, b) \iint e^{-2\pi i \left[ x \left( f_x - \frac{m}{p} - \frac{k_x}{2\pi} \right) + y \left( f_y - \frac{k_y}{2\pi} \right) \right]} dx dy \\ &= \sum_{m=-\infty}^{\infty} \hat{U}_y^s(m, b) \delta \left( f_x - \frac{m}{p} - \frac{k_x}{2\pi} \right) \delta \left( f_y - \frac{k_y}{2\pi} \right). \end{aligned} \quad (6.35)$$

Substitution in (5.19) with  $n^2 = \epsilon_u$  then leads to

$$\begin{aligned}
E_y^s(x, y, z) &= \iint e^{2\pi i(xf_x + yf_y) + iz\sqrt{k^2\epsilon_u - 4\pi^2(f_x^2 + f_y^2)}} \times \mathcal{F}(E_y^s)(f_x, f_y, b) \, df_x \, df_y \\
&= \sum_{m=-\infty}^{\infty} \hat{U}_y^s(m, b) \iint e^{2\pi i(xf_x + yf_y) + iz\sqrt{k^2\epsilon_u - 4\pi^2(f_x^2 + f_y^2)}} \times \\
&\quad \delta\left(f_x - \frac{m}{p} - \frac{k_x}{2\pi}\right) \delta\left(f_y - \frac{k_y}{2\pi}\right) \, df_x \, df_y \\
&= \sum_{m=-\infty}^{\infty} \hat{U}_y^s(m, b) e^{i\left[x\left(\frac{2\pi m}{p} + k_x\right) + yk_y + z\sqrt{k^2\epsilon_u - \left(k_x + \frac{2\pi m}{p}\right)^2 - k_y^2}\right]} \\
&= \sum_{m=-\infty}^{\infty} A_m^s e^{i\mathbf{k}_m \cdot \mathbf{r}}, \tag{6.36}
\end{aligned}$$

in which

$$\mathbf{k}_m = \left( k_x + \frac{2\pi m}{p}, k_y, +\sqrt{k^2\epsilon_u - \left(k_x + \frac{2\pi m}{p}\right)^2 - k_y^2} \right)^T, \tag{6.37}$$

with  $k$  the wave number in vacuum. The  $\mathbf{k}_m$  are called the wave vectors of the reflected field.

We conclude similarly that all electric and magnetic components of the reflected field in  $z > b$  can be written as a sum of plane waves. The following expansion in terms of plane waves thus applies for the total field in  $z > b$ :

$$\begin{aligned}
\mathbf{E}(\mathbf{r}) &= \mathbf{E}^i(\mathbf{r}) + \mathbf{E}^s(\mathbf{r}) \\
&= \mathbf{A}^i e^{i\mathbf{k} \cdot \mathbf{r}} + \sum_{m=-\infty}^{\infty} \mathbf{A}_m^s e^{i\mathbf{k}_m \cdot \mathbf{r}}, \tag{6.38}
\end{aligned}$$

$$\mathbf{H}(\mathbf{r}) = \mathbf{B}^i e^{i\mathbf{k} \cdot \mathbf{r}} + \sum_{n=-\infty}^{\infty} \mathbf{B}_m^s e^{i\mathbf{k}_m \cdot \mathbf{r}}. \tag{6.39}$$

Note that  $\mathbf{k}$  and  $\mathbf{k}_0$  have opposite  $z$ -components.  $\mathbf{A}^i$  and  $\mathbf{B}^i$  are the known complex amplitudes of the incident plane wave and the  $\mathbf{A}_m^s$  and  $\mathbf{B}_m^s$  are the (a priori unknown) amplitudes of the reflected field. Although there are an infinite number of scattered plane waves, only a finite number actually propagates, namely those for which  $m$  satisfies:

$$\left(k_x + \frac{2\pi m}{p}\right)^2 + k_y^2 < k^2\epsilon_u. \tag{6.40}$$

The rest of the waves are evanescent in the positive  $z$ -direction and propagate parallel to the  $(x, y)$ -plane. The  $m$ -th propagating reflected plane wave is called the  $m$ -th reflected order.

Because of the quasi-periodicity, the components  $E_y$  and  $H_y$  of the total field within  $\Omega$  can be written as follows in terms of Fourier series:

$$E_y(x, y, z) = \sum_{m=-\infty}^{\infty} \hat{E}_y(m, z) e^{i\left[\left(k_x + \frac{2\pi m}{p}\right)x + k_y y\right]}, \tag{6.41}$$

$$H_y(x, y, z) = \sum_{m=-\infty}^{\infty} \hat{H}_y(m, z) e^{i\left[\left(k_x + \frac{2\pi m}{p}\right)x + k_y y\right]}, \tag{6.42}$$

where  $\hat{E}_y(m, z)$  is the  $m$ -th Fourier coefficient given by

$$\hat{E}_y(m, z) = \frac{1}{p} \int_{-\frac{p}{2}}^{\frac{p}{2}} E_y(x, y, z) e^{-i\left[\left(k_x + \frac{2\pi m}{p}\right)x + k_y y\right]} \, dx, \tag{6.43}$$

with a similar formula for  $\hat{H}_y(m, z)$ . Since the components  $E_y$  and  $H_y$  are tangential to the plane  $z = b$  they must be continuous across this plane. Therefore the  $y$ -components of (6.38) and (6.39) must be equal to the corresponding equations (6.41) and (6.42) for  $z = b$ . This yields a set of equations for the unknown amplitudes  $A_m^s$  and  $B_m^s$ . To be able to eliminate these unknowns, we have to derive two additional equations. We accomplish this by looking at the other tangential components  $E_x$  and  $H_x$ . These components should also be continuous across the plane  $z = b$ . It is convenient to introduce the following notation to denote the  $x$ - and  $z$ -component of the wave vector  $\mathbf{k}_m$  given by (6.37):

$$k_{m,x} = k_x + \frac{2\pi m}{p}, \quad k_{m,z} = +\sqrt{k^2 \epsilon_u - \left(k_x + \frac{2\pi m}{p}\right)^2 - k_y^2}. \quad (6.44)$$

By substituting (6.38) and (6.39) into (6.22) and (6.24), respectively, we get for the half space  $z > b$ :

$$E_x(x, y, z) = \frac{i}{\omega^2 \mu_0 \epsilon_0 \epsilon_u - k_y^2} (ik_x k_y A^i - i\omega \mu_0 B^i) e^{i\mathbf{k} \cdot \mathbf{r}} \\ + \frac{i}{\omega^2 \mu_0 \epsilon_0 \epsilon_u - k_y^2} \sum_{m=-\infty}^{\infty} (ik_{m,x} k_y A_m^s - i\omega \mu_0 k_{m,z} B_m^s) e^{i\mathbf{k}_m \cdot \mathbf{r}}, \quad (6.45)$$

and

$$H_x(x, y, z) = \frac{i}{\omega^2 \mu_0 \epsilon_0 \epsilon_u - k_y^2} (i\omega \epsilon_0 \epsilon_u A^i + ik_x k_y B^i) e^{i\mathbf{k} \cdot \mathbf{r}} \\ + \frac{i}{\omega^2 \mu_0 \epsilon_0 \epsilon_u - k_y^2} \sum_{m=-\infty}^{\infty} (i\omega \epsilon_0 \epsilon_u k_{m,z} A_m^s + ik_{m,x} k_y B_m^s) e^{i\mathbf{k}_m \cdot \mathbf{r}}. \quad (6.46)$$

Within the unit cell  $\Omega$  we find by substituting (6.41) and (6.42) into (6.22) and (6.24):

$$E_x(x, y, z) = \frac{i}{\omega^2 \mu_0 \epsilon_0 \epsilon_u - k_y^2} \sum_{m=-\infty}^{\infty} \left( -\omega \mu_0 \frac{\partial \hat{H}_y(m, z)}{\partial z} + ik_{m,x} k_y \hat{E}_y(m, z) \right) e^{i(k_{m,x}x + k_y y)}, \quad (6.47)$$

$$H_x(x, y, z) = \frac{i}{\omega^2 \mu_0 \epsilon_0 \epsilon_u - k_y^2} \sum_{m=-\infty}^{\infty} \left( \omega \epsilon_0 \epsilon_u \frac{\partial \hat{E}_y(m, z)}{\partial z} + ik_{m,x} k_y \hat{H}_y(m, z) \right) e^{i(k_{m,x}x + k_y y)}. \quad (6.48)$$

By requiring that (6.45) and (6.47) are identical for  $z = b$  and similarly that (6.46) and (6.48) are the same for  $z = b$ , we obtain the two required additional equations. We finally obtain the following two coupled boundary conditions on  $z = b$ :

$$\frac{\omega \epsilon_0 \epsilon(x, b)}{\omega^2 \mu_0 \epsilon_0 \epsilon(x, b) - k_y^2} \frac{\partial \hat{E}_y(m, b)}{\partial z} - \frac{ik_{m,z} \omega \epsilon_0 \epsilon_u}{\omega^2 \mu_0 \epsilon_0 \epsilon_u - k_y^2} \hat{E}_y(m, b) - \frac{ik_{m,x} k_y}{\omega^2 \mu_0 [\epsilon(x, b) - \epsilon_u] - k_y^2} H_y(m, b) \\ = -\frac{2ik_{m,z} \omega \epsilon_0 \epsilon_u}{\omega^2 \mu_0 \epsilon_0 \epsilon_u - k_y^2} A^i e^{-ik_{m,z} b} \delta_{m0}, \quad \forall m, \quad (6.49)$$

and

$$\frac{\omega \mu_0}{\omega^2 \mu_0 \epsilon_0 \epsilon(x, b) - k_y^2} \frac{\partial \hat{H}_y(m, b)}{\partial z} + \frac{ik_{m,z} \omega \mu_0}{\omega^2 \mu_0 \epsilon_0 \epsilon_u - k_y^2} \hat{H}_y(m, b) + \frac{ik_{m,x} k_y}{\omega^2 \mu_0 [\epsilon(x, b) - \epsilon_u] - k_y^2} E_y(m, b) \\ = \frac{2ik_{m,z} \omega \mu_0}{\omega^2 \mu_0 \epsilon_0 \epsilon_u - k_y^2} B^i e^{-ik_{m,z} b} \delta_{m0}, \quad \forall m, \quad (6.50)$$

where  $\delta_{m0} = 1$  if  $m = 0$  and  $\delta_{m0} = 0$  if  $m \neq 0$ .

Analogously one finds by using the plane wave expansion in  $z < a$  that on the plane  $z = a$

$$\frac{\omega \epsilon_0 \epsilon(x, a)}{\omega^2 \mu_0 \epsilon_0 \epsilon - k_y^2} \frac{\partial \hat{E}_y(m, a)}{\partial z} - \frac{ik_{m,z} \omega \epsilon_0 \epsilon_l}{\omega^2 \mu_0 \epsilon_0 \epsilon_l - k_y^2} \hat{E}_y(m, a) \\ + \frac{ik_{m,x} k_y}{\omega^2 \mu_0 [\epsilon(x, a) - \epsilon_l] - k_y^2} H_y(m, a) = 0, \quad \forall m, \quad (6.51)$$

and

$$\begin{aligned} \frac{\omega\mu_0}{\omega^2\mu_0\epsilon_0\epsilon(x,a) - k_y^2} \frac{\partial \hat{H}_y(m,a)}{\partial z} + \frac{ik_{m,z}\omega\mu_0}{\omega^2\mu_0\epsilon_0\epsilon_l - k_y^2} \hat{H}_y(m,a) \\ - \frac{ik_{m,x}k_y}{\omega^2\mu_0[\epsilon(x,a) - \epsilon_l] - k_y^2} E_y(m,a) = 0, \quad \forall m, \end{aligned} \quad (6.52)$$

with  $k_{m,z}$  as defined in (6.44), but with  $\epsilon_u$  replaced by  $\epsilon_l$ . The right-hand side of (6.52) vanishes because of the assumption that there is no light incident from the lower half space. These conditions on the boundaries  $z = a$  and  $z = b$  are called radiation conditions. In contrast with for example absorbing boundary conditions, these radiation boundary conditions are exact and the boundary value problem on  $\Omega$  therefore is *equivalent* with the scattering problem for Maxwell's equations.

We now make the following important remark. The scattering of a quasi-periodic incident field can be computed in a similar way as for a single plane wave. For a quasi-periodic incident field,  $E_y^i$  and  $H_y^i$  are for some fixed  $(k_x, k_y)$  given by:

$$E_y^i(\mathbf{r}) = \sum_{m=-\infty}^{\infty} A_m^i e^{i\mathbf{k}_m^i \cdot \mathbf{r}}, \quad (6.53)$$

$$H_y^i(\mathbf{r}) = \sum_{m=-\infty}^{\infty} B_m^i e^{i\mathbf{k}_m^i \cdot \mathbf{r}}, \quad (6.54)$$

where

$$\mathbf{k}_m^i = \left( k_x + \frac{2\pi m}{p}, k_y, -\sqrt{k^2\epsilon_u - \left(k_x + \frac{2\pi m}{p}\right)^2 - k_y^2} \right)^T, \quad (6.55)$$

and the  $A_m^i$  and  $B_m^i$  are the amplitudes of the incoming orders. In the right-hand side of boundary conditions (6.49) and (6.50),  $A^i$  and  $B^i$  should then be replaced by  $A_m^i$  and  $B_m^i$  respectively and  $\delta_{m0}$  should be omitted. Note that often there are no evanescent waves in the incident field so that the sums in (6.53) and (6.54) are only over the finite number of propagating plane waves.

### 6.3 TE- and TM-polarization

When  $k_y = 0$  in (6.14), the field components do not depend on  $y$  and the diffraction problem is truly two-dimensional. Then equations (6.26) and (6.27) become two uncoupled scalar Helmholtz equations for  $E_y$  and  $H_y$ :

$$\omega^2\epsilon_0\epsilon\mu_0 E_y + \frac{\partial^2 E_y}{\partial x^2} + \frac{\partial^2 E_y}{\partial z^2} = 0, \quad (6.56)$$

$$\omega^2\mu_0 H_y + \frac{\partial}{\partial x} \left( \frac{1}{\epsilon} \frac{\partial H_y}{\partial x} \right) + \frac{\partial}{\partial x} \left( \frac{1}{\epsilon} \frac{\partial H_y}{\partial z} \right) = 0. \quad (6.57)$$

In case of homogeneous media, this is the same result as we have already derived earlier, where we showed that for every homogeneous material the electromagnetic field components satisfy scalar Helmholtz equations (but here  $\epsilon$  does not need to be constant). Let  $S$  be a surface with normal  $\mathbf{n}$  across which  $\epsilon$  is discontinuous. The transmission boundary conditions on this surface are then given by the requirement that the tangential electric and magnetic field components are continuous on  $S$ . Due to our assumption that all objects are invariant under translations parallel to the  $y$ -axis, the surface  $S$  will be parallel to the  $y$ -axis, and the normal  $\mathbf{n}$  will be in the  $(x,z)$ -plane:  $\mathbf{n} = (n_x, 0, n_z)^T$ . It thus follows that

$$\mathbf{n} \times \mathbf{E} = \begin{pmatrix} -n_z E_y \\ n_x E_z - n_z E_x \\ n_x E_y \end{pmatrix}, \quad (6.58)$$

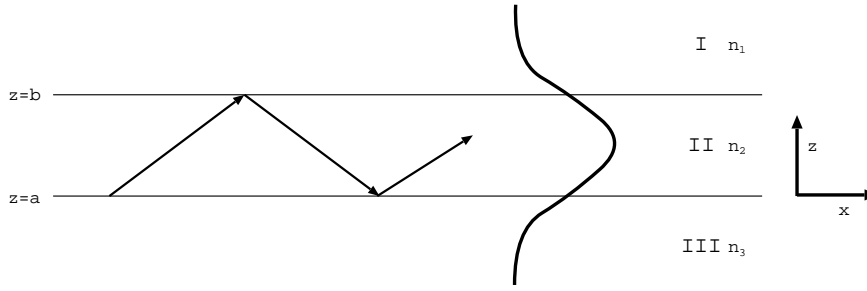


Figure 6.2: A plane geometry in a plane  $y = \text{constant}$  that is translation invariant in  $x$ - and  $y$ -direction.

and

$$\mathbf{n} \times \mathbf{H} = \begin{pmatrix} -n_z H_y \\ n_x H_z - n_z H_x \\ n_x H_y \end{pmatrix}, \quad (6.59)$$

are continuous. By substitution of equations (6.22)-(6.25) with  $k_y = 0$ , it is seen that this is equivalent with the continuity of respectively

$$E_y, \quad \frac{\partial E_y}{\partial n}, \quad (6.60)$$

and

$$H_y, \quad \frac{1}{\epsilon} \frac{\partial H_y}{\partial n}. \quad (6.61)$$

We can now conclude that when the electromagnetic field is two-dimensional ( $k_y = 0$ ), both the differential equations as well as the transmission boundary conditions expressed in terms of  $E_y$  and  $H_y$  are uncoupled. This implies that we can distinguish two polarizations: *TE-polarization* (transversale electric) and *TM-polarization* (transversale magnetic). It follows from (6.22)-(6.25) that in case of TE-polarization  $E_y$ ,  $H_x$  and  $H_z$  are in general non-zero while the other components are zero. In case of TM-polarization,  $H_y$ ,  $E_x$  and  $E_z$  are in general non-zero whereas the other components vanish. Note that TE-polarization is the same as S-polarization, whereas TM-polarization is the same as P-polarization as defined in Section 5.3.

When the electromagnetic field depends harmonically on  $y$  ( $k_y \neq 0$ ), all field components can still be expressed in terms of  $E_y$  and  $H_y$ , but the problem for  $E_y$  and  $H_y$  will then be coupled as is seen from (6.26), (6.27) and pure TE- and TM-polarizations can no longer be distinguished.

## 6.4 Uniqueness of the solution of the boundary value problem

It is outside the scope of this manuscript to formulate and prove the conditions under which the diffraction problem has a unique solution. Instead we refer to [21]. We only remark that as soon as there is some region (no matter how small) that is absorbing, uniqueness is guaranteed. In fact, when uniqueness does not hold, there is a solution of the diffraction problem without an incident field. But when there is absorption, such a solution which is periodic in  $x$  and time-harmonic can clearly not exist. We shall now give a simple example of a case where uniqueness does not hold.

Consider a planar structure as shown in Figure 6.2 that is translation invariant in the  $x$ - and  $y$ -direction. We assume the index of refraction  $n_2$  of the material in region II to be larger than the indices of refraction  $n_1$  and  $n_3$  in the regions I and III, respectively. Under certain conditions a solution of the Maxwell equations exists that is non-zero in region II and is exponentially decreasing in regions I and III. Such a solution is called a *guided wave*.

Consider a TE-polarized wave that is independent of  $y$  and harmonic in  $x$  and propagates in the positive  $x$ -direction in region II. The  $E_y$ -component of this wave has the form

$$E_y(x, z) = u(z)e^{ik_x x}, \quad (6.62)$$

where  $k_x > 0$ . According to (5.18),  $u(z)$  satisfies

$$(k^2 n_j^2 - k_x^2)u + \frac{d^2 u}{dz^2} = 0, \quad j = \begin{cases} 1 & \text{in region I,} \\ 2 & \text{in region II,} \\ 3 & \text{in region III,} \end{cases} \quad (6.63)$$

where  $k$  is the wave number in vacuum. By using the notation introduced in Section 5.3:

$$k_{jz} = \sqrt{k^2 n_j^2 - k_x^2}, \quad j = 1, 2, 3, \quad (6.64)$$

we can write the general solution as

$$u(z) = \begin{cases} C e^{ik_{1z}z} & z \text{ in region I,} \\ A e^{ik_{2z}z} + B e^{-ik_{2z}z} & z \text{ in region II,} \\ D e^{-ik_{3z}z} & z \text{ in region III,} \end{cases} \quad (6.65)$$

where  $C, A, B, D$  are constants that are to be determined from the jump relations at  $z = a$  and  $z = b$ . In case  $k_x^2 > k^2 n_1^2$  or  $k_x^2 > k^2 n_3^2$  the field decreases exponentially in the regions *I* and *III* or equivalently, the wave is totally reflected at the boundaries  $z = b$  and  $z = a$ . Total reflection is thus necessary for a solution that vanishes in the limit of  $|z| \rightarrow \infty$ .

We assume that  $k_x^2 > k^2 n_1^2$  or  $k_x^2 > k^2 n_3^2$  holds. The field components  $E_y$  and  $H_x = (-i/\omega\mu_0) \frac{\partial E_y}{\partial z}$  are tangential to the interfaces  $z = a, z = b$  and therefore have to be continuous there. This is equivalent with the continuity of  $u$  and  $\frac{du}{dz}$  at  $z = a$  and  $z = b$ . We thus obtain

$$A e^{ik_{2z}b} + B e^{-ik_{2z}b} - C e^{ik_{1z}b} = 0, \quad (6.66)$$

$$k_{2z} A e^{ik_{2z}b} - k_{2z} B e^{-ik_{2z}b} - k_{1z} C e^{ik_{1z}b} = 0, \quad (6.67)$$

$$A e^{ik_{2z}a} + B e^{-ik_{2z}a} - D e^{-ik_{3z}a} = 0, \quad (6.68)$$

$$k_{2z} A e^{ik_{2z}a} - k_{2z} B e^{-ik_{2z}a} + k_{3z} D e^{-ik_{3z}a} = 0. \quad (6.69)$$

This homogeneous system only has a solution if its determinant is equal to zero. This gives us an equation for  $k_x$  in terms of  $a, b, n_1, n_2, n_3$  and  $\mathbf{k}$ .

It can then be shown that the following statements hold [9]:

- If the refractive indices  $n_1$  and  $n_3$  of the regions *I* and *III* are equal and  $n_2 > n_1 = n_3$  there exists at least one real  $k_x$  such that there is a guided TE-wave.
- If the refractive indices of the regions *I* and *III* are different, then no guided waves exist for sufficiently small differences between  $n_2$  and  $n_1, n_3$ .

This implies that a guided TE-wave is a solution of the diffraction problem for  $k_x$  and  $k_y = 0$  without a source at  $|z| \rightarrow \infty$ . For a TM-polarized wave analogous results hold.

## 6.5 Variational formulation and the FEM

In the previous sections we derived for given  $(k_x, k_y)$  a coupled system of partial differential equations (6.26), (6.27) on the region  $\Omega$  (6.3) in terms of  $E_y$  and  $H_y$  with quasi-periodic boundary conditions (6.28) - (6.31) and radiation conditions (6.49) - (6.52). We will now derive the variational formulation for this boundary value problem (BVP).

The set of two coupled partial differential equations (6.26), (6.27) can be written as follows:

$$L(\mathbf{u}) \equiv \sum_{i,j=1}^2 D_i (S_{ij} D_j \mathbf{u}) + i S_{11} \mathbf{u} = 0, \quad (6.70)$$

where

$$D_1 = \frac{\partial}{\partial x}, \quad D_2 = \frac{\partial}{\partial z}, \quad \mathbf{u} = (u_1, u_2)^T, \quad u_1 = E_y, \quad u_2 = H_y, \quad (6.71)$$

and the  $S_{ij}$ ,  $1 \leq i, j \leq 2$  are (2,2)-matrices defined by

$$S_{11} = S_{22} = \frac{i}{\omega^2 \epsilon_0 \epsilon \mu_0 - k_y^2} \begin{pmatrix} \omega \epsilon_0 \epsilon & 0 \\ 0 & \omega \mu_0 \end{pmatrix}, \quad (6.72)$$

$$S_{12} = -S_{21} = \frac{i}{\omega^2 \epsilon_0 \epsilon \mu_0 - k_y^2} \begin{pmatrix} 0 & -k_y \\ k_y & 0 \end{pmatrix}. \quad (6.73)$$

We introduce the space

$$V = \{ \mathbf{v} | \mathbf{v} \in H^1(\Omega) \times H^1(\Omega), \mathbf{v}(x, z) e^{-ik_x x} \text{ is } p\text{-periodic with respect to } x \}, \quad (6.74)$$

equipped with the  $H^1(\Omega) \times H^1(\Omega)$ -norm  $\|\mathbf{v}\|_V$ . This means that for the given  $k_x$  we have

$$\mathbf{v}(x + p, z) = \mathbf{v}(x, z) e^{ik_x p}. \quad (6.75)$$

For  $\mathbf{v} \in V$  we put

$$\mathbf{v}(x, z) = \sum_{m=-\infty}^{\infty} \hat{\mathbf{v}}(m, z) e^{i(k_x + \frac{2\pi m}{p})x}. \quad (6.76)$$

It can then be shown [22] that if the field  $\mathbf{u} \in H_{loc}^1(\mathbb{R}^2) \times H_{loc}^1(\mathbb{R}^2)$  satisfies (6.70), the restriction of  $\mathbf{u}$  to  $\Omega$  is in  $V$  and is a solution of the following variational problem on  $\Omega$ :

$$a(\mathbf{u}, \mathbf{v}) + b(\mathbf{u}, \mathbf{v}) = \sum_{m=-\infty}^{\infty} \hat{\mathbf{F}}^{in}(m) \cdot \hat{\mathbf{v}}^*(m, b) \equiv -F^{in}(\mathbf{v}), \quad \forall \mathbf{v} \in V, \quad (6.77)$$

where  $a, b : V \times V \rightarrow \mathbb{C}$  are sesquilinear forms defined by

$$a(\mathbf{u}, \mathbf{v}) = \sum_{i,j=1}^2 \int_{\Omega} S_{ij} D_j \mathbf{u} \cdot D_i \mathbf{v}^* d\Omega + i \int_{\Omega} S_{11} \mathbf{u} \cdot \mathbf{v}^* d\Omega, \quad (6.78)$$

and

$$b(\mathbf{u}, \mathbf{v}) = \sum_{m=-\infty}^{\infty} \left[ B_0(m, \epsilon_u) \hat{\mathbf{u}}(m, b) \cdot \hat{\mathbf{v}}^*(m, b) + B_1(m, \epsilon_u) \hat{\mathbf{u}}(m, b) \cdot \mathbf{v}^*(m, b) \right. \\ \left. + B_0(m, \epsilon_l) \hat{\mathbf{u}}(m, a) \cdot \hat{\mathbf{v}}^*(m, a) + B_1(m, \epsilon_l) \hat{\mathbf{u}}(m, a) \cdot \mathbf{v}^*(m, a) \right], \quad (6.79)$$

with the matrices  $B_0(m, \bar{\epsilon}), B_1(m, \bar{\epsilon}), -\infty < m < \infty$  defined by

$$B_0(m, \bar{\epsilon}) = \frac{ik_{m,z}}{\omega^2 \mu_o \epsilon_0 \bar{\epsilon} - k_y^2} \begin{pmatrix} \omega \epsilon_0 \bar{\epsilon} & 0 \\ 0 & \omega \mu_0 \end{pmatrix}, \quad (6.80)$$

$$B_1(m, \bar{\epsilon}) = \frac{ik_{m,x}}{\omega^2 \mu_o \epsilon_0 \bar{\epsilon} - k_y^2} \begin{pmatrix} 0 & -k_y \\ k_y & 0 \end{pmatrix}, \quad (6.81)$$

and where the vector  $\hat{\mathbf{F}}^{in}(m)$  is determined by the incident field:

$$\hat{\mathbf{F}}^{in}(m) = \frac{2ik_{m,z}}{\omega^2 \mu_0 \epsilon_0 \epsilon_u - k_y^2} e^{-ik_{m,z}b} \begin{pmatrix} A_m^i \omega \epsilon_0 \epsilon_u \\ B_m^i \omega \mu_0 \end{pmatrix}. \quad (6.82)$$

The weak formulation in the infinite dimensional space  $V$  is equivalent to the boundary value problem formulated in the Sobolev space  $H^1(\Omega) \times H^1(\Omega)$ . In order to apply the FEM, the region  $\Omega$  is first discretised

with triangular elements such that the interfaces on which  $\epsilon$  is discontinuous are never intersected by an element. The basis functions are for example chosen to be piece-wise linear functions on this mesh.

We define a finite dimensional subspace  $V_N$  of  $V$  as the space of vector fields generated by the basis:

$$\mathbf{w}_k^\mu(x, z) = \phi^\mu(x, z)\mathbf{e}_k, \quad \mu = 1, 2, \dots, N, \quad k = 1, 3, \quad (6.83)$$

where  $\phi^\mu, \mu = 1, 2, \dots, N$  are real-valued basis functions such that  $\phi^\mu(x, z)e^{-ik_x x}$  is  $p$ -periodic with respect to  $x$  and where  $\mathbf{e}_1 = (1, 0, 0)^T$  and  $\mathbf{e}_3 = (0, 0, 1)^T$ . Hence the space  $V_N$  has dimension  $2N$ .

Any  $\mathbf{v} \in V_N$  can then be expressed as a linear combination:

$$\mathbf{v}(x, z) = \sum_{\mu=1}^N \mathbf{v}^\mu \phi^\mu(x, z), \quad (6.84)$$

with  $\mathbf{v}^\mu = (v_1^\mu, v_2^\mu)^T \in \mathbb{C}^2, \mu = 1, 2, \dots, N$ .

For fixed  $(k_x, k_y)$  we now pose the following finite dimensional problem:

Find  $\mathbf{u} \in V_N$  such that

$$a(\mathbf{u}, \mathbf{v}) + b(\mathbf{u}, \mathbf{v}) = -F^{in}(\mathbf{v}), \quad \forall \mathbf{v} \in V_N. \quad (6.85)$$

This numerical method is called the Galerkin method. We will not work out the variational formulation (6.85). Instead, the reader is referred to [19]. We will conclude this section with some additional remarks.

The matrix of the finite linear system is sparse, i.e. it has a relatively large number of zeros. This is an advantage of the FEM compared to other numerical methods, e.g. the method of integral equations.

The existence of a solution of (6.85) has been proven by Urbach [19]. Using the assumption that in all regions of  $\Omega$  one has  $k_y^2 < \omega^2 \text{Re}(\epsilon)\mu_0$ , it has been proved that provided uniqueness holds, the Galerkin method converges. In this way a constructive existence proof is obtained.

The radiation boundary conditions are not standard conditions. Although they express a relation between the field components and their normal derivative ( $\frac{\partial}{\partial z}$ ), they are formulated in terms of Fourier coefficients, which means that these boundary conditions are not local. That is, they are not defined in every point on the boundary separately. The Fourier series with respect to  $x$  of the basis functions  $\phi^\mu$  are needed. The Fourier series of a basis function  $\phi^\mu(x, z)$  has the form

$$\phi^\mu(x, z) = \sum_{m=-\infty}^{\infty} \hat{\phi}^\mu(m, z) e^{i(k_x + \frac{2\pi m}{p})x}, \quad (6.86)$$

where  $\hat{\phi}^\mu(m, z)$  denotes the  $m$ -th Fourier coefficient:

$$\hat{\phi}^\mu(m, z) = \frac{1}{p} \int_{-\frac{p}{2}}^{\frac{p}{2}} \phi^\mu(x, z) e^{-i(k_x + \frac{2\pi m}{p})x} dx. \quad (6.87)$$

The Fourier series can be problematic in case of piece-wise linear basis functions, since the Fourier series will in general converge slowly because the basis functions are not very smooth.

## 6.6 Incoming focused spot

Let us now consider an incident focused spot. We assume that the electric field component  $\mathbf{E}^i$  of the incident spot is known in a certain plane  $z = z_i$  above the grating. Let  $\mathcal{F}(\mathbf{E}^i)(f_x, f_y, z_i)$  be the Fourier transform of  $\mathbf{E}^i$  with respect to  $x$  and  $y$  in the plane  $z = z_i$ :

$$\mathcal{F}(\mathbf{E}^i)(f_x, f_y, z_i) = \iint e^{-2\pi i(f_x x + f_y y)} \mathbf{E}^i(x, y, z_i) dx dy. \quad (6.88)$$

The inverse Fourier transform

$$\mathbf{E}^i(x, y, z_i) = \iint e^{2\pi i(f_x x + f_y y)} \mathcal{F}(\mathbf{E}^i)(f_x, f_y, z_i) df_x df_y, \quad (6.89)$$

corresponds with a plane wave expansion of the incident field with wave vectors whose components in the  $x$ - and  $y$ -direction are given by  $2\pi f_x$  and  $2\pi f_y$ , respectively and whose complex amplitude is  $\mathcal{F}(\mathbf{E}^i)(f_x, f_y, z_i)$ .

With the Diffract program [24] the incident spot in the plane  $z = z_i$  can be computed. Diffract gives the  $E_x^i$ - and  $E_y^i$ -components of the incident field in this plane. As has been explained earlier, we only need the  $y$ -component of the electric and magnetic incident field ( $E_y^i, H_y^i$ ). Both  $E_x^i$  and  $E_y^i$  can be written as a superposition of plane waves in the plane  $z = z_i$  by using (6.89):

$$E_x^i(x, y, z_i) = \frac{1}{4\pi^2} \iint e^{i(k_x x + k_y y)} \mathcal{F}(E_x^i) \left( \frac{k_x}{2\pi}, \frac{k_y}{2\pi}, z_i \right) dk_x dk_y, \quad (6.90)$$

with a similar expression for  $E_y^i$ . For every  $(k_x, k_y)$ ,  $\mathcal{F}(E_x^i)$  and  $\mathcal{F}(E_y^i)$  are the complex amplitudes of plane waves with wave vector  $\mathbf{k}$  given by (6.95). It then follows from  $\mathbf{E} \cdot \mathbf{k} = 0$  that:

$$\mathcal{F}(E_z^i) = -\frac{1}{k_z} (k_x \mathcal{F}(E_x^i) + k_y \mathcal{F}(E_y^i)). \quad (6.91)$$

The magnetic incident field  $\mathbf{H}^i$  is then found by using (6.6).

Let  $p$  be the period of the grating. Then (6.89) can be rewritten as follows:

$$\begin{aligned} \mathbf{E}^i(x, y, z_i) &= \sum_{m=-\infty}^{\infty} \int_{-\infty}^{\infty} \int_{\frac{m}{p}}^{\frac{m+1}{p}} e^{2\pi i(f_x x + f_y y)} \mathcal{F}(\mathbf{E}^i)(f_x, f_y, z_i) df_x df_y \\ &= \sum_{m=-\infty}^{\infty} \int_{-\infty}^{\infty} \int_0^{\frac{1}{p}} e^{2\pi i(f_x x + f_y y)} e^{\frac{2\pi i m x}{p}} \mathcal{F}(\mathbf{E}^i) \left( f_x + \frac{m}{p}, f_y, z_i \right) df_x df_y \\ &= \int_{-\infty}^{\infty} \int_0^{\frac{2\pi}{p}} \mathbf{U}_{k_x, k_y}^i(x, z_i) e^{i(k_x x + k_y y)} dk_x dk_y, \end{aligned} \quad (6.92)$$

where

$$\mathbf{U}_{k_x, k_y}^i(x, z_i) = \frac{1}{4\pi^2} \sum_{m=-\infty}^{\infty} \mathcal{F}(\mathbf{E}^i) \left( \frac{k_x}{2\pi} + \frac{m}{p}, \frac{k_y}{2\pi}, z_i \right) e^{\frac{2\pi i m x}{p}}, \quad (6.93)$$

is  $p$ -periodic in  $x$ .

By using (5.14) in Section 5.1 it follows that

$$\mathcal{F}(\mathbf{H}^i)(f_x, f_y, z_i) = \frac{\mathbf{k}}{\omega \mu_0} \times \mathcal{F}(\mathbf{E}^i)(f_x, f_y, z_i), \quad (6.94)$$

where  $\mathbf{k}$  is given by (5.20):

$$\mathbf{k} = \begin{pmatrix} k_x \\ k_y \\ k_z \end{pmatrix} = \begin{pmatrix} 2\pi f_x \\ 2\pi f_y \\ \sqrt{k^2 \epsilon_u - 4\pi^2(f_x^2 + f_y^2)} \end{pmatrix}. \quad (6.95)$$

Hence for the magnetic component of the incident spot  $\mathbf{H}^i$  we can write:

$$\mathbf{H}_{k_x, k_y}^i(x, y, z_i) = \int_{-\infty}^{\infty} \int_0^{\frac{2\pi}{p}} \mathbf{V}_{k_x, k_y}^i(x, z_i) e^{i(k_x x + k_y y)} dk_x dk_y \quad (6.96)$$

where

$$\mathbf{V}_{k_x, k_y}^i(x, z_i) = \frac{1}{4\pi^2} \sum_{m=-\infty}^{\infty} \frac{\mathbf{k}}{\omega \mu_0} \times \mathcal{F}(\mathbf{E}^i) \left( \frac{k_x}{2\pi} + \frac{m}{p}, \frac{k_y}{2\pi}, z_i \right) e^{\frac{2\pi i m x}{p}}, \quad (6.97)$$

Hence we have written the electric and magnetic components of the incident spot as an integral over  $k_x$  and  $k_y$  of the quasi-periodic fields

$$\mathbf{U}_{k_x, k_y}^i(x, z_i) e^{i(k_x x + k_y y)}, \quad \mathbf{V}_{k_x, k_y}^i(x, z_i) e^{i(k_x x + k_y y)} \quad (6.98)$$

When no confusion can arise we will omit the subscript  $(k_x, k_y)$  in the sequel. Actually, only the  $y$ -component of the incident electric and magnetic field need to be known, i.e. the quasi-periodic fields

$$U_y^i(x, z_i) e^{i(k_x x + k_y y)}, \quad (6.99)$$

$$V_y^i(x, z_i) e^{i(k_x x + k_y y)}, \quad (6.100)$$

need to be given.

In Section 6.1 we have explained that for each of these quasi-periodic incident fields the corresponding scattered fields are also quasi-periodic. Furthermore, the total field for the electric and magnetic field components (i.e the sum of the quasi-periodic incident field and the quasi-periodic scattered field) is quasi-periodic.

By solving the BVP for each of the quasi-periodic incident fields (6.99), (6.100) corresponding to each  $(k_x, k_y)$  in the ranges  $0 \leq k_x \leq \frac{2\pi}{p}$ ,  $-\infty < k_y < \infty$ , we obtain the  $y$ -components of the total electric ( $\mathbf{U}^{tot}$ ) and magnetic field ( $\mathbf{V}^{tot}$ ) for this  $k_x, k_y$  in the unit cell  $\Omega$ . By adding these quasi-periodic solutions we can compute the total  $y$ -components of the electric and magnetic fields due to the entire incident spot:

$$E_y^{tot}(x, y, z) = \int_{-\infty}^{\infty} \int_0^{\frac{2\pi}{p}} U_y^{tot}(x, k_y, z) e^{i(k_x x + k_y y)} dk_x dk_y, \quad (6.101)$$

$$H_y^{tot}(x, y, z) = \int_{-\infty}^{\infty} \int_0^{\frac{2\pi}{p}} V_y^{tot}(x, k_y, z) e^{i(k_x x + k_y y)} dk_x dk_y. \quad (6.102)$$

For each  $(k_x, k_y)$  the other electric and magnetic field components can be immediately obtained from equations (6.22)-(6.25) and are added accordingly.

For an incident spot the components of the total electric and magnetic field can therefore be written as

$$\mathbf{E}^{tot}(x, y, z) = \int_{-\infty}^{\infty} \int_0^{\frac{2\pi}{p}} \mathbf{U}_{k_x, k_y}^{tot}(x, z) e^{i(k_x x + k_y y)} dk_x dk_y, \quad (6.103)$$

$$\mathbf{H}^{tot}(x, y, z) = \int_{-\infty}^{\infty} \int_0^{\frac{2\pi}{p}} \mathbf{V}_{k_x, k_y}^{tot}(x, z) e^{i(k_x x + k_y y)} dk_x dk_y. \quad (6.104)$$

These formulae apply to the total field in an *arbitrary* point  $(x, y, z)$ , hence not only to points in the unit cell  $\Omega$ .

## 6.7 Sampling of the incident spot

The focused spot as calculated by the Diffract program is a sampled spot. In order to get accurate results when an incident spot is simulated, the number of terms that is used in the plane wave expansion of the spot must be sufficiently large. Let  $\Delta x, \Delta y$  be the grid distances in  $(x, y)$ -space and  $N_x, N_y$  the number of grid points in the  $x$ - and  $y$ -direction, respectively. We define  $K$  as the number of points of the  $(x, y)$ -grid that are within the period  $p$ :

$$K = \frac{p}{\Delta x}. \quad (6.105)$$

Hence we assume that  $\Delta x$  is chosen such that  $p$  is a multiple of  $\Delta x$ .

It remains to specify the number of grid points  $N_x$  and  $N_y$  in  $x$ - and  $y$ -direction. We will now discuss the restrictions for the choice of  $N_x$ .  $N_y$  is often chosen equal to  $N_x$ .

Because we use the Fast Fourier Transform (FFT) to compute the plane wave expansion, the grid in the  $(k_x, k_y)$ -plane (reciprocal space) is coupled to the grid in the  $(x, y)$ -plane (ordinary space):

$$\Delta k_x = \frac{2\pi}{N_x \Delta x}, \quad \Delta k_y = \frac{2\pi}{N_y \Delta y}. \quad (6.106)$$

To make sure that for every grid point  $(k_x, k_y)$  the various orders  $(k_x + \frac{2\pi m}{p})$ ,  $m$  integer, are also grid points in reciprocal space, an integer  $j$  must exist such that the following holds:

$$\frac{2\pi}{p} = j \Delta k_x = \frac{j}{N_x \Delta x}. \quad (6.107)$$

By combining (6.105) and (6.107) we then get:

$$K = \frac{p}{\Delta x} = \frac{N_x}{j}. \quad (6.108)$$

Because  $K$  and  $j$  are both integers it follows that  $N_x$  must be a multiple of  $K$ .

Let  $\mathcal{L}_{k_x}$  be the length in the  $k_x$ -direction of the region in reciprocal space where the intensity of the spot can not be neglected. To avoid aliasing effects, in addition to the previous constraint,  $N_x$  should be chosen such that at least holds:

$$N_x \Delta k_x \geq 2\mathcal{L}_{k_x}. \quad (6.109)$$

## Chapter 7

# The Cyclop program

As has been mentioned in the Introduction, the first version of the Cyclop program developed by Urbach and Merks is a FEM solver for the two-dimensional grating problem for quasi-periodic incident fields derived in the previous chapter. The Cyclop program is based on the FEM software package Sepran [25] and is written in FORTRAN77. In this chapter we will give a description of the 1998 version of Cyclop. We will successively discuss the preprocessing and the main structure of Cyclop in Sections 7.1 and Section 7.2. We end this chapter with some remarks about the analytical computation of the total electromagnetic field in planar multi-layers.

### 7.1 The Cyclop preprocessing

To be able to run a simulation with the Cyclop program the geometry must be described and the incident field must be specified. This preprocessing is done with the program Bicycle. With Bicycle a general input file for the Cyclop program is generated.

#### 7.1.1 Bicycle and the general Cyclop input file

Bicycle uses an input file called **jobname.dat**<sup>1</sup>, in which the user specifies the geometry and the type of incident field. When the incident field is quasi-periodic, the wave length, amplitudes of the field components, propagation directions and the mode numbers have to be specified. In case a general three-dimensional incident spot is to be simulated, no further information about the field has to be specified in the Bicycle input file. This information is provided to Cyclop by two additional input files which we will discuss later. By means of an example we will explain how the geometry of the unit cell  $\Omega$  is to be specified.

Assume that the geometry we want to model is a grooved structure of a material with refractive index  $n_1$ , that is periodic in  $x$ -direction and translation invariant in the  $y$ -direction. For simplicity we assume also that the material surrounding the structure has an index of refraction  $n_2$ . We choose the region  $\Omega$  such that it contains one period of the structure and furthermore that the half-spaces above and below the structure are as large as possible. See Figure 7.1 (a).

We then subdivide the region  $\Omega$  in rectangular and triangular regions. This is done by placing a rectangular grid over the geometry such that the interfaces in  $x$ - and  $z$ -direction coincide with interconnection lines of the grid and such that a sloped interface forms the diagonal of at least one rectangle. See Figure 7.1 (b). In the input file for Bicycle the width of each column from left to right, and the height of each row from bottom to top have to be specified. For each rectangle and triangle of the subdivision and for the half-space above and below the region  $\Omega$ , the index of refraction is also to be specified. These indices of refraction are allowed to be complex.

---

<sup>1</sup>In practice the name of the problem (job) to be solved, the 'jobname', can be any arbitrary name.

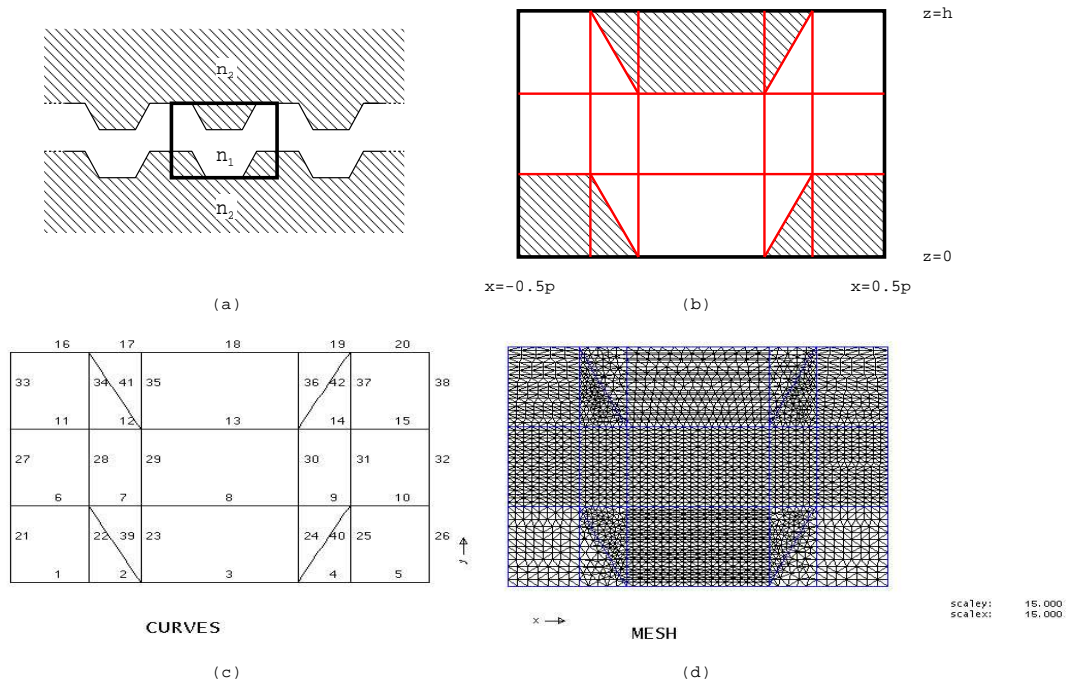


Figure 7.1: An example of a periodic structure (a). The thick rectangle is the unit cell  $\Omega$ . In Bicycle  $\Omega$  is subdivided into rectangles and triangles (b). The results of the Sepran mesh generator are shown in (c) and (d).

For all incident fields one additional parameter, *nelements*, has to be given. This parameter specifies the number of elements of the Sepran mesh per curve per wavelength in the material to be generated by the Sepran mesh generator.

From the data in the file **jobname.dat** the Bicycle program generates a general input file for Cyclop. This input file, called **jobname.input**, consists of three blocks of information. The first two blocks are specific to Sepran and thus use a predefined syntax. In the first Sepran input block (MESH2D) the geometry of the unit cell is defined. The coordinates of the vertices of the rectangles and triangles of the subdivision described above are translated such that for the  $x$ -coordinates of all points holds that  $-0.5p \leq x \leq 0.5p$ . Actually, the unit length is chosen such that  $p = 1$ , hence the cell corresponds to  $-0.5 \leq x \leq 0.5$ . The curves connecting these points are defined as straight lines with linear elements (LINE1). The number of elements on each curve is calculated by Bicycle using the values of the parameter *nelements* and the refractive indices of the materials on both sides of the curve. The curves that together form the upper and lower boundary are combined respectively to a single curve. Both are coupled to a line element (MESHLINE, LELM#). One 'super-element' is created that contains all points on each of these curves (SHAPE = -1).

The rectangular regions are defined as surfaces using the submesh generator quadrilat with triangular elements (QUADRILAT3). The triangular regions are defined as surfaces using the submesh generator triangle with triangular elements (TRIANGLE3). Each of these surfaces is coupled to a single surface element (MESH SURF, SELM#). The curves that form the left boundary ( $x = -0.5p$ ) are combined to a single curve. The same is done for the curves that form the right boundary ( $x = 0.5p$ ). The points on these two boundary curves are connected (MESHCONNECT, CURVES0).

In the second Sepran block (PROBLEM) a description of the problem in terms of types of element groups is given. Both the upper and lower boundary curve are coupled to their own element group (ELGRP#) with user problem definition types 11 and 12, respectively. Each surface element is coupled to a element group, with increasing user problem definition types 21, 22, ... The number of degrees of freedom (NUMDEGFD) in the nodal points for each of these line and surface element groups is 2, because these are

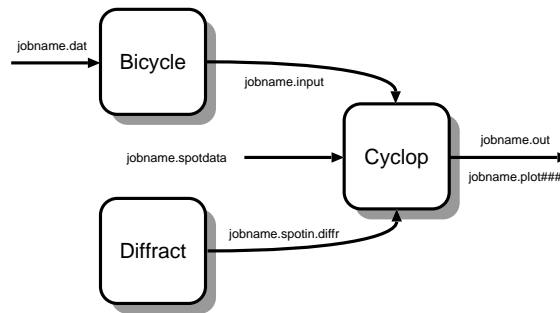


Figure 7.2: Overview of the input/output structure of the 1998 version of Cyclop for an incident spot.

the (complex) unknowns per nodal point, namely  $E_y$  and  $H_y$ . To store quasi-periodic quantities, Sepran vectors of special type are defined via VEC1=(2) for vectors with 2 degrees of freedom and VEC2=(1) for vectors with one degree of freedom. The element defined by MESHCONNECT is coupled to an element group with type -1 (periodic boundary).

The last block of the file **jobname.input** contains some additional data about the geometry and the incident field. The extra information about the geometry consists of the indices of refraction for the various element groups and the period length of the unit cell in microns (recall that the points of the computational box are scaled with respect to the period length). For quasi-periodic incident fields the wavelength, amplitude and phase of the field components and polarization are also defined. This data is omitted in case of an incident spot, since this information is then specified in additional files that we will discuss in the next section.

The final part of the general Cyclop input file also contains several boolean flags that can be set by the user to indicated what data should be printed/plotted during postprocessing.

### 7.1.2 Additional Cyclop input files

When the incident field is a spot, besides the general input file two additional files are needed. The first file, **jobname.inspot.diffr**, contains the grid and the  $E_x$ - and  $E_y$ - components of the incident field on this grid. The structure of this data is dictated by an output file generated by the optical package Diffract by Mansuripur et al.

The second file, **jobname.spotdata**, contains the specification of the grid in Fourier space used in the computations of the FFT's (the sampling) of the incident field. The position of the incident spot with respect to the grating is also specified. This grid can be specified as desired by the user independent of the grid in the Diffract file.

An overview of the input/output structure for this Cyclop version is shown in Figure 7.2

## 7.2 The main structure of Cyclop

The structure of the Cyclop program can be divided into three parts: initialization, a loop over all quasi-periodic fields and the postprocessing. We will now successively discuss each of these parts.

### 7.2.1 Initialization

After the initialization of Sepran, the mesh is generated by calling subroutine MESH. All input that is read from the input file **jobname.input**. The structure of the mesh is stored in the Sepran vector KMESH. For the definition of the problem the subroutine PROBDF is called. The input is read from file **jobname.input**. The information about the problem is stored in the Sepran vector KPROB. Then the structure of the large

matrix is defined by using subroutine COMMAT. The matrix is not hermitian and it is complex symmetric. The linear system is solved by using a direct solver.

Now the non-Sepran related data is read from the general input file **jobname.input**. For quasi-periodic fields the  $(k_x, k_y)$  can be directly retrieved from this input file. In case of an incident spot the incident field as calculated by Diffract is read from the file **jobname.spotin.diff**. The field is sampled and then Fourier transformed by using the Fast Fourier Transform (FFT). The specifications about the Fourier grid needed in the computation of the FFT's are read from the file **jobname.spotdata**. When the grid defined by the parameters in **jobname.spotdata** for the FFT differs from the grid in **jobname.spotin.diff** (which in general it does), the incident field specified in **jobname.spotin.diff** is interpolated.

Finally, all (Sepran) vectors are created and initialized. Most variables are stored in pairs, such as the field components  $(E_y, H_y)$ , in complex vectors with two degrees of freedom.

## 7.2.2 The main loop

The core of the Cyclop program is the double loop over all relevant pairs  $(k_x, k_y)$ . The outer loop is over all  $k_y$ , the inner loop over all  $k_x$ . In pseudo code the double loop can be described as follows:

```

for all k_y do
  for all k_x do
    if (flux(k_x, k_y) < threshold) then
      goto next k_x
    else
      solve the BVP for the pair (k_x, k_y)
      calculate x- and z-derivatives of the solution
      add solution coherently to the sum over previous k_x
      do the same for the derivatives
    endif
  enddo
  compute the other field components
  add field components to the sum over previous k_y
enddo

```

At the start of the inner loop it is checked if the pair  $(k_x, k_y)$  satisfies the criterion of minimum incident flux [?]. If the incident flux of the quasi-periodic field corresponding to a certain pair  $(k_x, k_y)$  is smaller than a minimum threshold, the BVP is not solved for this pair  $(k_x, k_y)$  and the corresponding solution is considered to vanish.

If the incident flux is not negligible, the large matrix and the right-hand side vector of the linear system for the BVP corresponding to the pair  $(k_x, k_y)$  are build by a call to SYSTEM0. All element groups are used (including the line element groups). The linear system is solved by means of a Gaussian elimination method  $(L^T - D - L)$ . The solution of the BVP is stored in solution vector  $femeh_y$ .

From the solution vector the derivatives in  $x$ - and  $z$ - direction, which are needed to calculate the other components of the electromagnetic field, are determined. The derivatives are calculated per element via a linear interpolation routine (DERIVA). The derivatives with respect to  $x$  and  $z$  are stored in vectors  $d_x femeh_y$  and  $d_z femeh_y$ , respectively.

The solution vectors  $femeh_y$  for all  $k_x$  are coherently summed and stored in vector  $femeh_y tot$ . The same is done for the derivative vectors  $d_x femeh_y$  and  $d_z femeh_y$ . The summed derivatives are stored in vectors  $d_x femeh_y tot$  and  $d_z femeh_y tot$  respectively.

After the loop over all  $k_x$  the remaining field components are computed. For fixed given  $k_y$  all field components can be expressed in terms of the  $E_y$ - and  $H_y$ - component via (6.22)-(6.25). Hence we can use the sum of the field components over all  $k_x$ ,  $femeh_y tot$  and the sums of the derivatives of the field components over all  $k_x$ ,  $d_x femeh_y tot$  and  $d_z femeh_y tot$ . The  $x$ - and  $z$ -components of the field for this fixed value of  $k_y$  are calculated and the results are coherently summed and stored in the vectors  $femeh_x tot$  and  $femeh_z tot$ .

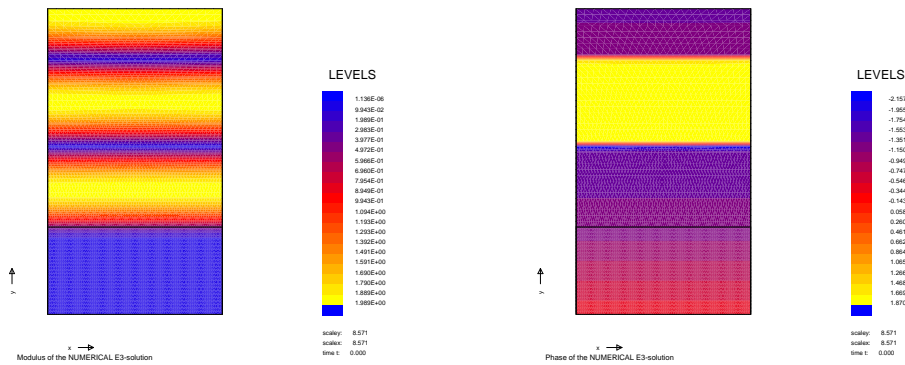


Figure 7.3: Two examples of Sepran plots for the whole computational box. The modulus (left) and phase (right) of the  $y$ -component of a TE-polarized plane wave ( $\lambda = 400 \text{ nm}$ ) with amplitude 1 in air ( $n = 1.0$ ) that is perpendicularly incident on a flat aluminium ( $n = 0.28 + 4.1i$ ) layer. The air layer is  $500 \text{ nm}$  thick, the aluminium layer is  $200 \text{ nm}$  thick and the region is  $400 \text{ nm}$  wide.

### 7.2.3 Postprocessing

The total electric and magnetic field are now known on every point of the mesh of the two-dimensional unit cell  $\Omega$ . Recall that these fields are complex valued. To analyze the total fields, real quantities such as the modulus and phase of the field components are desired. The values of these real quantities can then be printed to an output file **jobname.out** or plotted (**jobname.plot###**). The plots can be made for the whole unit cell (two-dimensional) or along an arbitrary curve defined by Bicycle. The plots can be viewed by the Sepran program Sepview. Figure 7.3 shows two examples of Sepran plots.

## 7.3 Calculation of an analytical solution

In the special case that the unit cell  $\Omega$  consists of flat homogeneous regions with interfaces parallel to the  $(x, y)$ -plane it is possible to derive an analytical solution for each pair  $(k_x, k_y)$  of the corresponding BVP. In the presently used version of Cyclop, the only components of the electromagnetic field that are computed analytically are  $E_y$  and  $H_y$ . As with the numerical solution, the components of the total electromagnetic field are acquired by coherently summing the solutions for each pair  $(k_x, k_y)$ . In Cyclop the derivation of the analytical solution is also implemented in the main double loop. We have omitted it in the pseudo code above because in general an analytical solution does not exist. However, for flat geometries this analytical solution is important since it can be used to verify the numerical results.

## Chapter 8

# Extension of the Cyclop program

In the previous chapter the 1998 version of the Cyclop program has been discussed with which the total electromagnetic field can be determined in a two-dimensional unit cell  $\Omega$  contained in some plane  $y = \text{constant}$ . In this chapter we will discuss how the solution on this two-dimensional region  $\Omega$  can be extended in  $x$ - and  $y$ -direction to a sufficiently large three-dimensional region. We will start this chapter by discussing the theory behind this extension. In Section 8.2 we will describe how this extension is implemented in Cyclop. We end this chapter by discussing a modification made to Bicycle and an improvement of Cyclop regarding the analytical solution.

### 8.1 Extension from the 2d-unit cell to a 3d-region

The total electric and magnetic field on the unit cell  $\Omega$  are given by (6.103) and (6.104)

$$\mathbf{E}^{tot}(x, y, z) = \int_{-\infty}^{\infty} \int_0^{\frac{2\pi}{p}} \mathbf{U}_{k_x, k_y}^{tot}(x, z) e^{i(k_x x + k_y y)} dk_x dk_y, \quad (8.1)$$

$$\mathbf{H}^{tot}(x, y, z) = \int_{-\infty}^{\infty} \int_0^{\frac{2\pi}{p}} \mathbf{V}_{k_x, k_y}^{tot}(x, z) e^{i(k_x x + k_y y)} dk_x dk_y, \quad (8.2)$$

where  $\mathbf{U}_{k_x, k_y}^{tot}(x, z)$ ,  $\mathbf{V}_{k_x, k_y}^{tot}(x, z)$  are  $p$ -periodic functions with respect to  $x$  and independent of  $y$  which are obtained from the solutions of the BVP for the  $(k_x, k_y)$ -pair considered. As has been remarked in Section 6.6, formulae (8.1), (8.2) apply to arbitrary points  $(x, y, z)$  which need not to be in the plane  $y = \text{constant}$  of  $\Omega$ . For all  $|m| = 1, 2, \dots$  the total fields in a period  $-0.5p + mp \leq x \leq 0.5p + mp$  and in a plane  $y = y + \Delta y$  are given by

$$\mathbf{E}^{tot}(x, y, z) = \int_{-\infty}^{\infty} \int_0^{\frac{2\pi}{p}} \mathbf{U}_{k_x, k_y}^{tot}(x, z) e^{i(k_x x + k_y y)} e^{i(k_x mp + k_y \Delta y)} dk_x dk_y, \quad (8.3)$$

$$\mathbf{H}^{tot}(x, y, z) = \int_{-\infty}^{\infty} \int_0^{\frac{2\pi}{p}} \mathbf{V}_{k_x, k_y}^{tot}(x, z) e^{i(k_x x + k_y y)} e^{i(k_x mp + k_y \Delta y)} dk_x dk_y. \quad (8.4)$$

We see that the extension of the total field in the unit cell to a arbitrary other period and at arbitrary distance in  $y$ -direction from the unit cell comes down to multiplication of the total field in the unit cell by a factor  $e^{i(k_x mp + k_y \Delta y)}$  for each given pair  $(k_x, k_y)$ . In the next section we will describe how this extension is added to the Cyclop program. In Cyclop the unit cell  $\Omega$  lies in the plane  $y = 0$ .

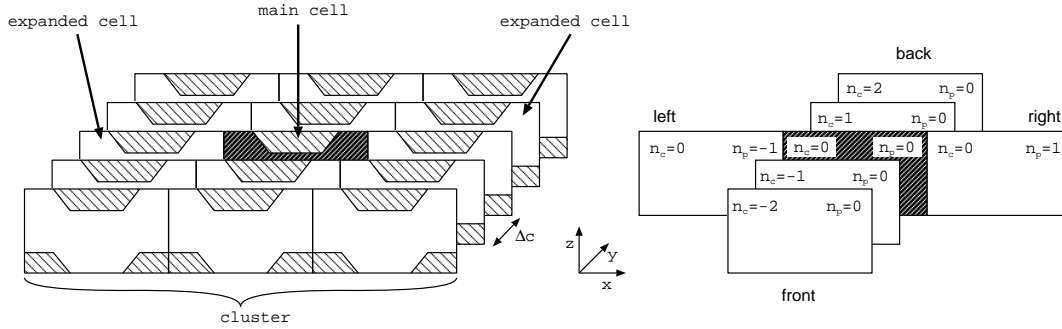


Figure 8.1: The extended geometry.

## 8.2 The implementation of the extension in Cyclop

We will first start with some definitions and notations. We refer to Figure 8.1 for the visualization of the notations. From this point onwards we will refer to the unit cell  $\Omega$  as the *main cell*. For every period in every plane  $y = \text{constant}$  we have a cell of which the geometry is exactly the same as that of the main cell. Since we are going to expand the total electromagnetic field to these cells we will refer to them as *expanded cells*. The two-dimensional region formed by several adjacent cells in a plane  $y = \text{constant}$  will be called a *cluster*. The cluster that contains the main cell is called the *main cluster*.

The number of expanded cells (and thus periods) in the  $x$ -direction will be denoted by  $N_p$  and the total number of clusters in the  $y$ -direction by  $N_c$ . It is convenient to take  $N_p$  and  $N_c$  odd so that we have an equal amount of expanded cells to the left and to the right and an equal number of clusters in front and behind the main cell and the main cluster, respectively. The cells in one cluster are indexed from left to right. For the *period index*  $n_p$  it follows that  $n_p = -\frac{N_p-1}{2}, \dots, \frac{N_p-1}{2}$ . The clusters are indexed from front to back. For the *cluster index*  $n_c$  we have  $n_c = -\frac{N_c-1}{2}, \dots, \frac{N_c-1}{2}$ . Consequently,  $n_p = n_c = 0$  for the main cell. The distance between two successive clusters will be denoted by  $\Delta c$ .

We recall from Section 7.2 that the structure of the Cyclop program can be divided into an initialization part, a main double loop over all  $(k_x, k_y)$  pairs and a postprocessing part. We will now discuss the extensions and modifications needed for the extension made to these three parts.

### 8.2.1 Modification of the initialization

From the description of the main loop over the  $(k_x, k_y)$  it follows that for the extension we will need to create five Sepran vectors for every expanded cell. Three vectors are needed in the inner loop over all  $k_x$  to store the accumulative sums of the BVP solution vector ( $femeh_ytot$ ) and the two derivative vectors ( $d_x femeh_ytot, d_z femeh_ytot$ ), respectively. The two other vectors are used in the outer loop to store the accumulative sums of the derived field components ( $femeh_xtot, femeh_ztot$ ). Thus, for the extension we need five arrays of  $N_p \times N_c$  vectors.

The vectors for the expanded cells are created with the Sepran subroutine CREAVC where the vectors KMESH and KPROB are used. Consequently, the structure of these solution vectors is equal to that of the solution vectors for the main cell and are therefore also periodic.

### 8.2.2 The modified main loop

In pseudo code the modified double loop in Cyclop is as follows:

```
for all k_y do
  for all k_x do
```

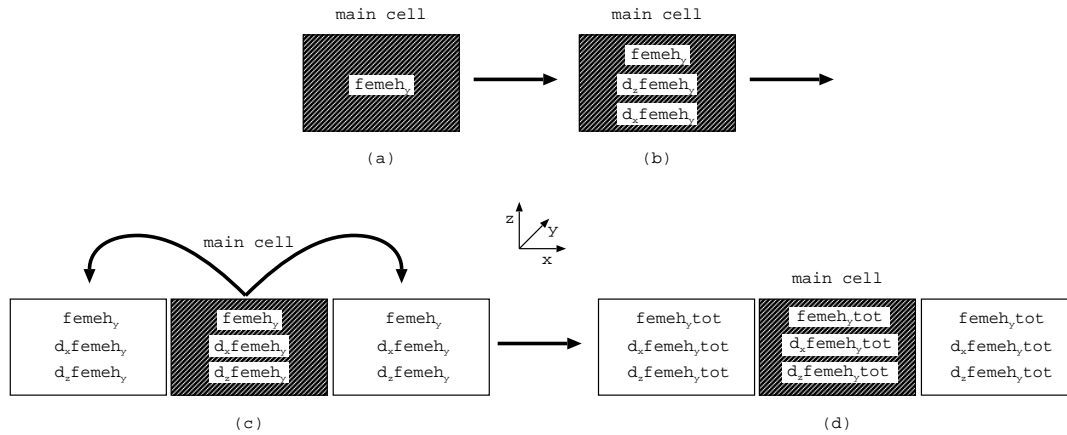


Figure 8.2: The inner loop for the extension. When the solution of the BVP is computed (a) the  $x$ - and  $z$ -derivatives are calculated (b) and these three vectors are expanded to all cells in the main cluster by multiplying by the appropriate factor  $e^{ik_x n_p p}$  (c). The results are then added to the accumulative sums over previous  $k_x$  (d).

```

if (flux(k_x, k_y) < threshold) then
  goto next k_x
else
  solve the BVP for the pair (k_x, k_y)
  calculate x- and z-derivatives of the solution
  for all $N_p$ expanded cells in main cluster do
    multiply solution and derivatives by  $\exp(i k_x n_p p)$ ,
    with  $n_p$  the period index
    add expanded solution coherently to the accumulated
    sum over previous  $k_x$ 
    do the same for the expanded derivatives
  enddo
endif
enddo
for all  $N_p$  expanded cells in main cluster do
  for all  $N_c$  clusters do
    compute the other field components
    multiply all field component vectors by
     $\exp(i k_y n_c \Delta_c)$ , with  $n_c$  the cluster index
    add field components coherently to the accumulated
    sum over previous  $k_y$ 
  enddo
enddo
enddo

```

In the inner loop it is first checked whether the pair  $(k_x, k_y)$  satisfies the criterion of minimum incident flux. When the flux is not negligible, the BVP for the given pair on the main cell is solved and the solution is stored in the vector  $femeh_y$ . Then the derivatives with respect to  $x$  and  $z$  are computed and stored in the vectors  $d_x femeh_y$  and  $d_z femeh_y$ , respectively. For the expanded cells in the main cluster with period indices  $n_p = -\frac{N_p-1}{2}, \dots, \frac{N_p-1}{2}$  the vectors  $femeh_y$ ,  $d_x femeh_y$  and  $d_z femeh_y$  are multiplied by the appropriate factor  $e^{ik_x n_p p}$ . The resulting expanded vectors are then in every cell of the main cluster coherently added to the accumulative sum vectors  $femeh_y,tot$ ,  $d_x femeh_y,tot$  and  $d_z femeh_y,tot$ . See Figure 8.2.

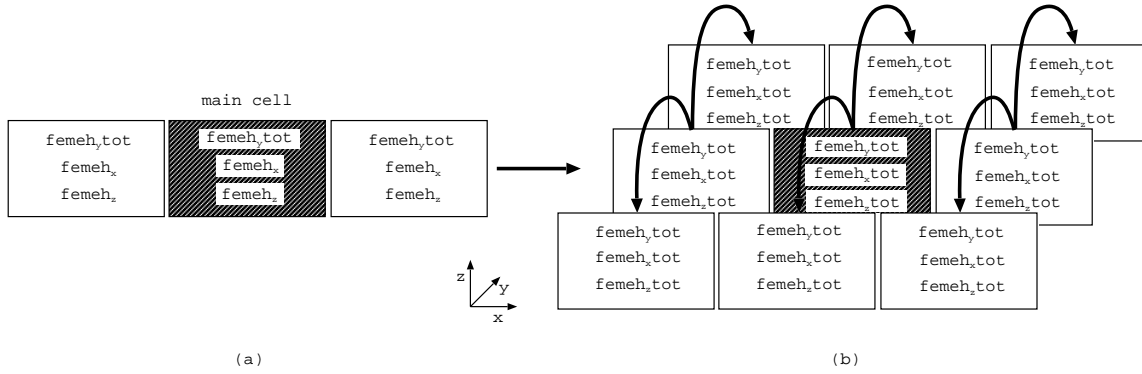


Figure 8.3: In the outer loop of the extension the field components  $E_x, H_x$  and  $E_z, H_z$  are computed in every cell of the main cluster (a). These vectors are then extended in the  $y$ -direction by multiplying by the appropriate factor  $e^{ik_x n_c \Delta c}$ . The results are then added to the accumulative sums over previous  $k_y$  (b)

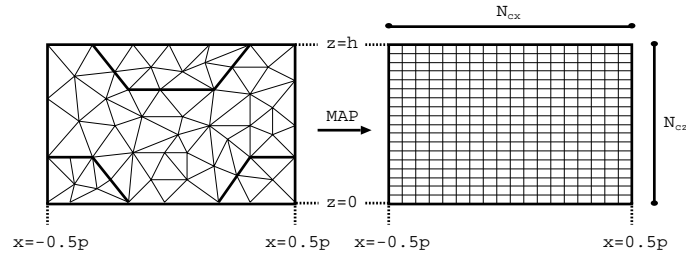


Figure 8.4: To visualize real quantities known on the nodal points of the Sepran mesh of each cell we map these values to a rectangular grid with dimensions  $N_{cx} \times N_{cz}$ .

After the loop over all  $k_x$ , for fixed  $k_y$  the field components  $E_x, H_x$  and  $E_z, H_z$  are then computed in every cell of the main cluster using the vectors  $femeh_{y,tot}$ ,  $d_x femeh_{y,tot}$  and  $d_x femeh_{y,tot}$ . In all  $N_p$  vectors in the main cluster this results in the vectors  $femeh_x$  and  $femeh_z$ . Finally we extend the vectors  $femeh_{y,tot}$ ,  $femeh_x$  and  $femeh_z$  for each cell in the main cluster in the  $y$ -direction by multiplying by a factor  $e^{ik_y n_c \Delta c}$ , where  $n_c$  is the appropriate cluster index,  $n_c = -\frac{N_c-1}{2}, \dots, \frac{N_c-1}{2}$ . After the multiplication, the resulting vectors in every expanded cell are coherently added to the correct accumulative vectors  $femeh_{y,tot}$ ,  $femeh_{x,tot}$  and  $femeh_{z,tot}$ . Note that for the cells in the main cluster this comes down to a multiplication by 1. See Figure 8.3.

### 8.2.3 Modification of the postprocessing

To be able to analyze the total electromagnetic field that we have computed, real quantities such as the modulus and phase of the various field components can be calculated in every cell of the extended region. For each cell this data can then be printed to an output file or plotted and viewed with Sepview. But what we would really like is to visualize these quantities for the expanded region as a whole. This is done by using the Amira graphics package.

Amira is a 3D visualization and modelling system [23]. The AmiraMesh format, which is Amira's native general-purpose file format, allows the storage of field values on a rectangular grid.

Assume we have an array of  $N_p \times N_c$  vectors in which for each expanded cell we have stored a real quantity (e.g. the modulus of a field component). We now first create a rectangular grid for the main cell with  $N_{cx}$  points in  $x$ -direction  $-0.5p \leq x \leq 0.5p$  and  $N_{cz}$  points in  $z$ -direction  $0 \leq z \leq h$ . We then use the Sepran interpolation routine INTCOOR to map the quantity values from the points of the Sepran mesh of the main cell, as stored in vector KMESH, to the points of the rectangular grid. Information about the mapping

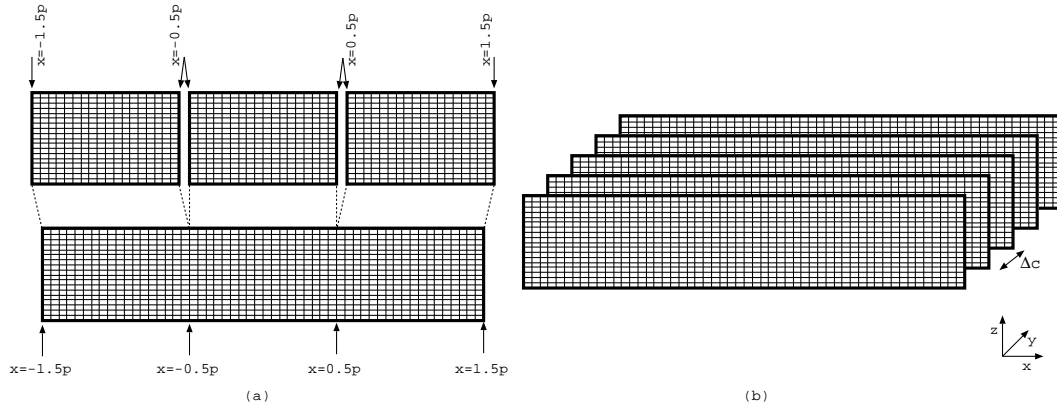


Figure 8.5: For adjacent cells in a cluster we have to omit double points (a). In (b) an impression is given of the grid for the whole expanded region.

is stored in a vector MAP. By now using the fact that all expanded cells implicitly have the same mesh structure, we can map the quantity vectors on all expanded cells by using subroutine INTCOOR, with the same rectangular grid and the vector KMESH. We thereby use the mapping specifications already stored in the vector MAP in the first call to subroutine INTCOOR to speed up the mapping process.

After the mapping, we have for every expanded cell, including the main cell, the values of the quantity of interest on the nodes of the rectangular grid. We now create a rectangular grid for the whole extended region. The grid distances in  $x$ - and  $z$ -direction for the 3D-grid are taken equal to  $p/(N_{cx} - 1)$  and  $h/(N_{cz} - 1)$ . The grid distance in  $y$ -direction we choose equal to  $\Delta c$ . We can now write the coordinates of this 3D-grid and the corresponding mapped quantity values in the expanded cells to the Amira mesh-file. Note that for two adjacent cells in a cluster the most right column of grid points of the left cell and most left column of grid points of the right cell actually represent the same points. To avoid double points in the amira mesh-file, we therefore make sure that we omit the coordinates of the most right columns and their corresponding quantity values for the first  $N_p - 1$  cells (counted from left to right) in every cluster.

### 8.3 Additional modifications to Bicycle and Cyclop

For very complicated geometries such as those of a Blu-ray disk stack, the number of surfaces that Bicycle generates becomes very large. Since Bicycled assigned each surface to a separate element group this becomes problematic. This is because in Sepran the total number of user element groups is at maximum 99. Larger numbers can not be used since they are reserved for the standard element groups of Sepran. Therefore, Bicycle has been modified in such a way that all surfaces corresponding to rectangles and triangles of which the refractive index is equal are combined in a single grouped surface by using the SURFACES keyword.

In the previous chapter we have mentioned that in the special case that  $\Omega$  consists of a multi-layer with flat interfaces, the  $y$ -components of the total electromagnetic field can be computed analytically. Previously in Cyclop only the  $E_y$  and  $H_y$  components were computed analytically. We have extended Cyclop such that now also all other field components are calculated on  $\Omega$  (no extension of the analytic solution to the three-dimensional region is done however). By calculating the  $l_2$ -norm of the absolute differences between the numerical and analytical solutions it is possible to get insight in the precision of the numerical model.

Finally, the absorbed energy (4.55) and the total time-average electromagnetic energy density (4.57) can be computed in every expanded cell of the enlarged region.

## Chapter 9

# Integration of the Cyclop output into the heat diffusion model

In the previous chapter we have described how the two-dimensional solution on the main cell is extended to a three-dimensional region. From the extended total electric field the absorbed energy  $W(x, y, z)$  on the whole extended region can be determined. In Chapter 2 we have pointed out that the absorbed energy known in the nodal points of the Cyclop mesh can be mapped to the three-dimensional mesh used in the thermal model. In this chapter we will describe the various steps that have been taken to integrate the absorbed energy data calculated by Cyclop into the thermal model and the problems that were encountered.

The first step was to separate the postprocessing process from the main Cyclop program. We will discuss the stand alone postprocessing program Cycpost in Section 9.1. The mapping has been integrated in the Cycpost program and is discussed in Section 9.2. In Section 9.3 we discuss how the mapped data is integrated in the thermal model.

The method used in the preprocessor program Bicycle turned out to be too inaccurate. Therefore an alternative has been made, which is described in Section 9.4. Several of the various other problems encountered are discussed in Section 9.5.

### 9.1 Cycpost: the Cyclop postprocessor

When we simulate a spot that is incident on a complex geometry such as that of a Blu-ray disk stack, then depending on the number of quasi-periodic fields in the main double loop, the Cyclop program can take a very long time to run (i.e. over 20 hours). With the postprocessing part of the Cyclop program, if one wants to view a quantity that has not yet been derived and printed/plotted, the whole Cyclop program has to be run once more. It is therefore convenient to separate the postprocessing part from the Cyclop program.

After the main double loop, the arrays containing the components of the total electromagnetic field for the whole extended region and (if applicable) the analytical solution vectors for the main cell  $\Omega$  are written to Sepran output file **jobname.sepcomp**. This is done by using the Sepran subroutine **OUTSOL**. In order to be able to use this subroutine correctly, several changes have to be made to Cyclop and its general input file **jobname.input**. In Cyclop the calls to subroutines **START**, **MESH**, **PROBDF** and **COMMAT** are replaced by a single call to subroutine **SEPSTM**. This subroutine reads information about the large matrix (**MATRIX** block) and the number of vectors that is to be written to **jobname.sepcomp** (**OUTPUT** block) from **jobname.input**, in addition to the information about the mesh (**MESH2D** block) and the problem definition (**PROBLEM** block). Bicycle is therefore modified such that it adds these last two blocks to the general input file. Some additional parameters that are needed for postprocessing, such as the value of a boolean flag that indicates whether an analytical solution has been calculated and stored or not, are written to a file called **jobname.params**.

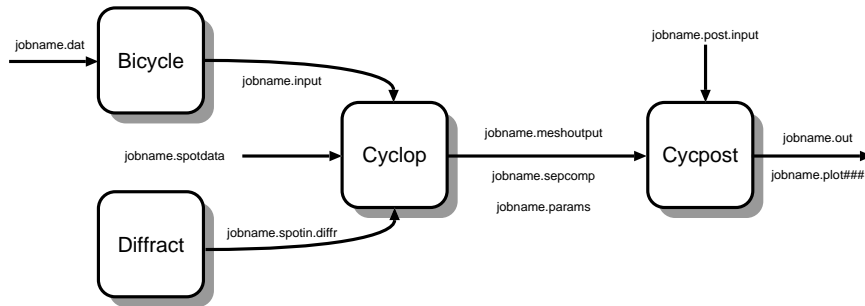


Figure 9.1: The Cyclop input/output structure when the postprocessing is separated and performed by the Cycpost program.

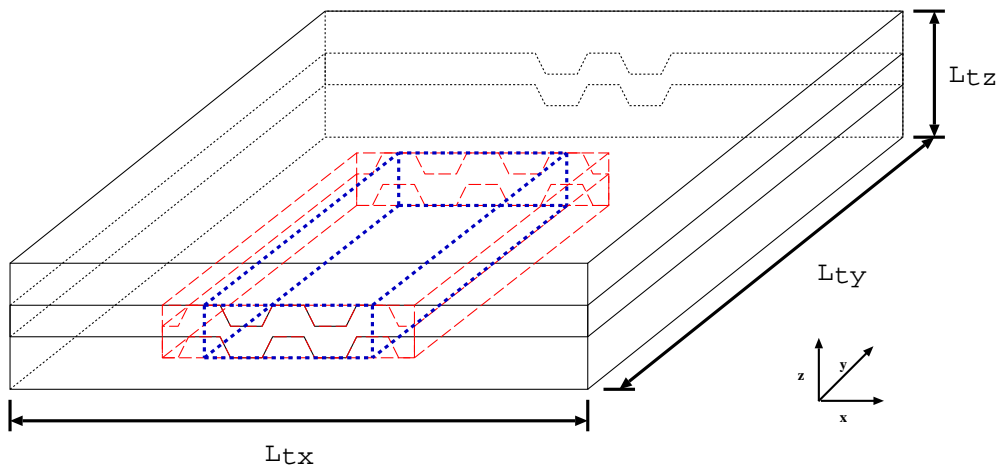


Figure 9.2: Visualization of the Cyclop extended region ('red box') in the computational box of the thermal model ('black box') (at  $t = 0$ ). The geometries of both models are equal in the 'blue box'.

The Cyclop postprocessing program Cycpost is based on the Sepran postprocessing program Seppost. Cycpost reads the solution arrays from the **jobname.sepcomp** file, the vectors KMESH and KPROB from the file **jobname.meshoutput** and finally the extra parameters from **jobname.params**. In the input file **jobname.post.input** the user can specify by means of boolean flags which quantities are to be computed, printed and/or plotted. All postprocessing functions that were present in the extended Cyclop program, including the 3D-visualization with Amira, are also available in Cycpost.

Finally, the mapping which we will discuss next, is implemented in Cycpost.

## 9.2 Mapping of the extended Cyclop output to the heat diffusion mesh

We will first describe the computational box used in the thermal model. In the translation invariant  $y$ -direction along the grooves, the box has length  $L_{ty}$ . The height in  $z$ -direction is  $L_{tz}$ . In the  $x$ -direction two periods of the grooved structure are often chosen. In the current model of the heat problem it is assumed that the exterior of the computational box consists of a flat multi-layer (i.e. there are no grooves). The total length of the computational box in  $x$ -direction is  $L_{tx}$ .  $L_{tx}$ ,  $L_{ty}$  and  $L_{tz}$  are chosen sufficiently large to make sure that the adiabatic boundary conditions are sufficiently accurate. See Figure 9.2.

For the extension in Cyclop we choose to extend to a region three periods wide in the  $x$ -direction ( $N_p = 3$ ) and three periods long in the  $y$ -direction. The number of clusters  $N_c > 3$  can be freely chosen. In the

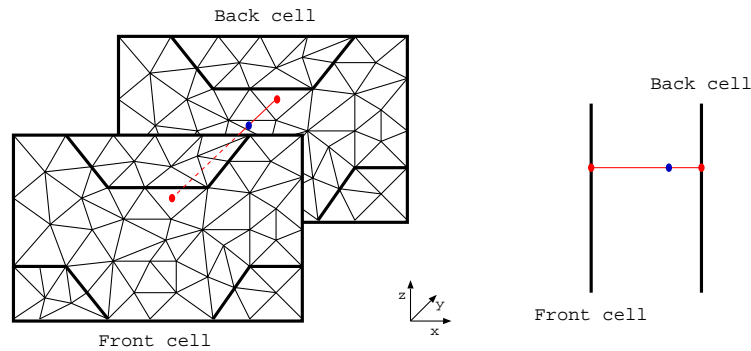


Figure 9.3: When the cells have been determined between which the mapped nodal point  $(x_c, y_c, z_c)$  (blue dot) lies, the absorption values in both cells are interpolated (red dots). These interpolated values are once more interpolated to acquire the absorbed energy in the mapped nodal point.

current extended Cyclop a value  $N_c = 59$  is used.

In Figure 9.2 we have drawn the extended region of Cyclop ('red box') in the thermal computational box. The coordinate system for the thermal model is chosen such that its axes coincide with those of the Cyclop model. The optical axis of the incident spot coincides with the  $z$ -axis of both models.

Let us now assume that we have calculated the absorbed energy in every cell in the extended Cyclop region. Remark that in Cyclop we have three grooved periods, while in the thermal model we have only two grooved periods. For every nodal point of the thermal mesh that lies outside the 'blue box' shown in Figure 9.2 we therefore set the absorbed energy equal to zero.

We generate the mesh for the thermal computational box by using the Sepran program Sepmesh. The information about the mesh is stored in the file **3dmeshoutput**.

In pseudo code the mapping as implemented in Cycpost can be described as follows:

```

read thermal 3d-mesh from file 3dmeshoutput
create user array containing nodal points of the thermal 3d-mesh
for every nodal point of the thermal mesh do
  map coordinates of nodal point to Cyclop coordinates
  if nodal point lies outside 'blue box'
    return absorption = 0
  else
    determine period index
    determine cluster indices of cells immediately in front of
      and immediately behind the considered point
    translate x-coordinate such that  $-0.5p < x < 0.5p$ 
    interpolate in front cell with INTCOOR (f)
    interpolate in back cell with INTCOOR (b)
    linear interpolate between (f) and (b)
  endif
enddo

```

We start by reading the vector that stores the information about the 3d-mesh of the thermal model by using the Sepran subroutine MESHRD and store it in a vector KMESH2 (we already have a vector KMESH with information about the mesh of the main cell). All coordinates of the nodal points of the 3d-mesh are then stored in a double precision user array (via KMESH2(23)).

We then loop over all points of the thermal 3d-mesh. First the coordinates are transformed to Cyclop coordinates. Let us denote these Cyclop coordinates of the point by  $(x_c, y_c, z_c)$ . If this point lies outside the 'blue box' in Figure 9.2 we set the absorption to zero at that point. Otherwise we continue by determining

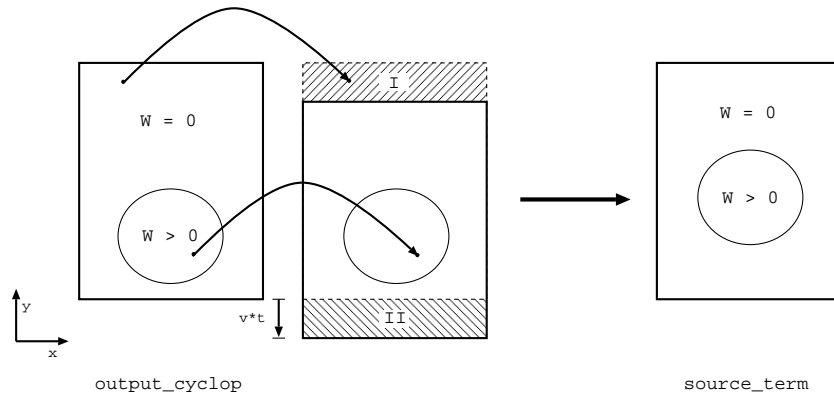


Figure 9.4: A visualization of how a source term is obtained at a time step  $t > 0$  from the source term calculated by Cyclop for  $t = 0$ .

between which two expanded cells the mapped point lies, see Figure 9.3. The period index  $n_p$  and the cluster indices  $n_{c,f}$ ,  $n_{c,b}$  of the cells directly in front of and behind the mapped point follow from the  $x$ - and the  $y$ -coordinate, respectively.

Since in each cluster we have a two-dimensional geometry, we temporarily omit the  $y$ -coordinate of the mapped nodal point. Recall that the solution vectors for the expanded cells have the same structure as those on the main cell. Therefore we first translate the  $x$ -coordinate of the mapped nodal point to the main cell so that  $-0.5p \leq x_c + n_p p \leq 0.5p$ . We can then compute the interpolated absorbed energy values in the point  $(x_c + n_p p, z_c)$  in the expanded cells immediately in front of and behind the mapped nodal point by using the Sepran interpolation subroutine INTCOORD (with vectors KMESH and KPROB of the main cell). Finally we linearly interpolate these two interpolated absorption values to obtain the absorbed energy in the point  $(x_c, y_c, z_c)$  (and thus in the corresponding point in the thermal 3d-mesh).

The array of interpolated absorption values is written to the standard Sepran backup storage file **sepranback** by using the Sepran subroutine WRITBS.

### 9.3 Integration of the mapped data in the thermal model

The three-dimensional heat diffusion equation (2.1) is a second order real linear parabolic equation for one unknown function, namely the temperature  $T$ . Such a differential equation is a standard problem in Sepran. It can therefore be solved by using the Sepran programs Sepmesh, Sepcomp and Seppost.

In the previous section a description of the three-dimensional computational box used in the thermal model has been given. With Sepmesh a mesh can be generated for this computational box. Sepmesh requires an input file called **jobname.msh** in which a description of the discretization of the computational box is given in terms of Sepran keywords. Each layer of the stack to be modelled is assigned to a single volume element group. Each of these volumes is generated by using the volume generator pipe with tetrahedral elements (PIPE11). The surfaces are generated with the submesh generators rectangle and pipesurface with triangular elements (RECTANGLE3 and PIPESURFACE3). The points of the mesh are connected with line elements with 2 points (LINE1).

When the mesh file has been made, the heat diffusion equation is solved by using the program Sepcomp. The problem is specified in the input file **jobname.prb**. All element groups are of type 800 (potential problem).

To describe a differential equation of a standard form in Sepran, such as the heat diffusion equation considered, it suffices to specify the coefficients of the differential equation. The coefficients that are assigned a value are 6, 9 and 11 (the heat conductivity  $\kappa$  in  $x$ -,  $y$ - and  $z$ -direction, respectively), 16 (the source  $Q$ ) and 17 (the heat capacity  $\rho C_p$ ). These coefficients are specified for each element group individually. In

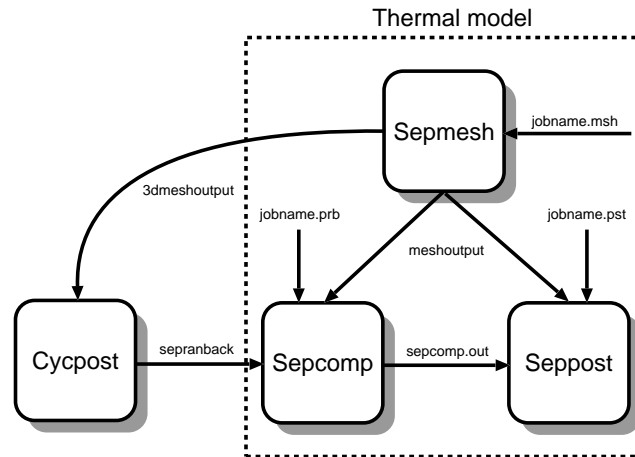


Figure 9.5: An overview of the file communication structure between Cycpost and the thermal model.

the original thermal model, a moving spot is simulated by filling coefficient 16 for every nodal point of the thermal mesh at any time step by means of a user defined analytical function of position and time (via the assignment  $coef\ 16 = (points, iref = -1)$  and user subroutine FUNC).

We have replaced this analytically defined heat source by a heat source as calculated by Cyclop in the following way. At  $t = 0$  the double precision array containing the absorbed energy  $W(x, y, z)$  in every nodal point of the thermal mesh is read from the Sepran backup storage file **sepranback**. This data is then stored in a Sepran vector called *output\_cyclop* of solution type (110). To simulate the movement of the spot, at every discretized time  $t$  the data in *output\_cyclop* is mapped on a copy of the thermal mesh that has been shifted in the negative  $y$ -direction over a distance  $v * t$ , where  $v$  is the velocity at which the spot moves. This results in a Sepran vector *source\_term* that contains the heat source at time  $t$ .

In Figure 9.4 this mapping has been visualized. For the mapping Sepran subroutine INTMSH3D is used. For nodal points that are mapped into region *I* of the shifted mesh, the absorbed energy  $W$  is set to zero at these points. The data at nodal points that are mapped into region *II* can be considered to be 'lost'. Consequently, for  $v > 0$ , from a certain time step  $t > 0$  at which nodal points were  $W > 0$  are mapped into region *I*, the vector containing the source term will become unusable.

The vector *source\_term* is used to fill coefficient 16 for every nodal point of the thermal mesh by the assignment  $coef\ 16 = old\ solution$ . The intensity of the spot can be changed by multiplying with an intensity factor  $I$ .

The Sepcomp program can be instructed to write the calculated temperature distribution at every time step  $t$  to a file called **sepcomp.out**. The Sepran postprocessor Seppost can then be used to interpret the data in **sepcomp.out**.

Figure 9.5 shows the file communication structure in case the thermal simulation is run with a heat source that has been calculated by Cyclop.

## 9.4 An alternative for Bicycle

The sloped edges of the grooves of the disk structures that we model are inconvenient when the geometry is described using the Bicycle program. Due to the complexity of for instance the stack of a Blu-ray disk, the division of the region  $\Omega$  in rectangles and triangles causes that the sloped interfaces are subdivided and contained in several rectangles. See Figure 9.6. Consequently, instead of straight lines, the slopes are represented by piece-wise linear curves. This results in undesirable inaccuracies. Furthermore, creating the Sepran part of the general input file **jobname.input** manually is very time consuming, especially for such complex geometries and therefore is no alternative to using a preprocessor.

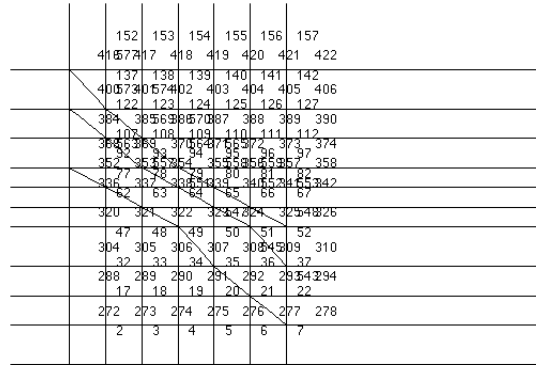


Figure 9.6: In case of very complex geometries the sloped interfaces are approximated by piece-wise linear curves.

Hence, a start has been made to develop an alternative for Bicycle. In *xfig*<sup>1</sup> we draw each layer of the stack structure that we want to describe as a closed polygon. As a unit of length we use one pixel to represent one nanometer. When we have drawn the whole unit cell, we save the drawing in the standard *xfig* format to the file **jobname.fig**. Since this file is an ASCII file, we can manually add additional information such as the refractive indices corresponding to the various layers of the stack we have represented by polygons and the wavelength of the incident light. By processing the file **jobname.fig** with an *AWK*<sup>2</sup> script, we generate the Sepran blocks of the general input file **jobname.input**. The vertices and edges of the polygons are coupled to the points and curves of the mesh description. The number of elements per curve is calculated from the wave length and the refractive indices. The regions formed by the polygons are defined as surfaces using the submesh generator general with triangular elements (GENERAL3). To complete the input file we use the non-Sepran part from the input file generated by Bicycle for the same geometry. After some minor modifications to this non-Sepran part we then have a general input file in which the interfaces of the stack are exactly described.

## 9.5 Problems encountered

The performance of numerical programs such as Cyclop and the thermal model not only depend on the implementation but also on the computer systems on which these programs are run. Depending on the fineness of the mesh and the sampling rate of the spot, Cyclop jobs require a computer system with a large memory to store the large matrix and the right-hand side vector of the discretized linear system, the solution vectors and derived quantity vectors.

The geometries such as that of a BD-disk recording stack are relatively complex and therefore a relative large memory is required. At first, the Cyclop program constantly failed to run, even though the computer to which the job was submitted had enough memory available. This turned out to be caused by the limited stack size of the computer systems that were used.

The extension of the two-dimensional quasi-periodic fields to a three-dimensional region and the mapping of the meshes required features that probably were hardly ever (or never) tested before. At various occasions when Sepran errors or warnings occurred, the problem at hand could be solved by contacting Sepra. Unfortunately, in several cases a lot of time had to be spent on debugging because no apparent reason could be found for the crashing of the software. As a result of this debugging some bugs and limitations in Sepran have been discovered.

<sup>1</sup>A graphical tool for the X Windows System.

<sup>2</sup>A pattern-directed scanning and processing language.

# Chapter 10

## Numerical simulations

When running numerical simulations it is important to validate the results of these simulations and consider their accuracy. In the first section we will discuss the precision of the numerical solution of Cyclop for a geometry consisting of homogeneous plane regions by comparing this solution with the analytical solution. In Section 10.2 results of the extension of the two-dimensional Cyclop data on the unit cell to a three-dimensional region are discussed. The extended absorbed energy will be mapped to the three-dimensional mesh of the thermal model to replace the previously analytically given heat source. The thermal model with the integrated Cyclop heat source is validated for a plane geometry by comparing the results of the simulation with the results of the Media program. In Section 10.3 the validation of the integrated thermal model is discussed. In the two concluding sections of this chapter we will successively consider a stationary and a moving spot for a Blu-ray disk recording stack. In nearly all of the figures in this chapter arbitrary units are used.

### 10.1 Accuracy of the Cyclop solution

In Section 7.3 we remarked that in case the geometry of the unit cell consists of flat homogeneous regions with interfaces parallel to the  $(x,y)$ -plane, an analytical solution of the BVP can be calculated. As has been remarked in Section 8.3 all six components of the electromagnetic field can be analytically computed with Cyclop when such plane geometries are considered.

To gain insight in the precision of the numerical solution, a comparison is made with the analytical solution. Let  $\mathbf{u}$  denote a field component of the analytical solution and let  $\hat{\mathbf{u}}$  denote the corresponding field component of the numerical solution. The relative error between the numerical and the analytical solution is measured by the quantity:

$$\frac{\|\mathbf{u} - \hat{\mathbf{u}}\|_2}{\|\mathbf{u}\|_2}, \quad (10.1)$$

where  $\|u\|_2$  is the  $l_2$ -norm defined by:

$$\|\mathbf{u}\|_2 = \sqrt{\sum_{i=1}^N (u_i \cdot u_i^*)/N}, \quad (10.2)$$

where  $N$  is the number of nodal points and  $u_i$  is the value of the field component in nodal point  $i$ .

Let us consider an unit cell containing a geometry with flat homogeneous regions and interfaces parallel to the  $(x,y)$ -plane with specifications as shown in Table 10.1 and Figure 10.1. The reason for using this geometry is that it is similar to the Blu-ray disk recording stack which we will consider in the Sections 10.3-10.5. Since the metal layer is 120 nm thick, in Cyclop it can be taken to be a half space. In order to be able to visualize field quantities in the upper part of the metal layer, we chose the thickness of this layer

Table 10.1: The parameters, their abbreviations and values that are used for the simulations of a planar structure.

Wavelength in vacuum	$\lambda$	405 nm
Period of the grating	$p$	320 nm
Index of refraction of substrate	$n_{subs}$	1.6
Index of refraction of metal	$n_{met}$	$0.17 + 2.04i$
Index of refraction of dielectric material	$n_{die}$	2.28
Index of refraction of phase-change material	$n_{pha}$	$1.52 + 3.36i$

in the unit cell to be equal to the skin depth of 30 nm. The half space below the unit cell is filled with the metal.

First we consider the accuracy of the numerical Cyclop solution for a linearly TE-polarized plane wave of which the amplitude of  $E_y$  is 1 V/m. The wavelength of the plane wave is 405 nm and it is incident on the geometry as shown in Figure 10.1 under an angle of 52 degrees with the  $z$ -axis, with the wave vector  $k$  in the  $(x, z)$ -plane. In Table 10.2 an overview is given of the relative errors of the various components of the total electromagnetic field for three values of the parameter *nelements*. As has been remarked in Section 7.1.1, this parameter is used to specify the fineness of the finite element mesh of the unit cell. The higher the value of *nelements*, the finer the mesh. From Table 10.2 it becomes clear that the convergence of the numerical solution to the analytical solution is quadratical in *nelements*.

As an example we visualize the modulus of  $H_x$  of which the numerical solution (*nelements* = 40) is shown in Figure 10.2. In Figure 10.3 the numerically and analytically computed modulus of  $H_x$  are shown for *nelements* = 20 and *nelements* = 40 along a vertical curve parallel to the  $z$ -axis. For *nelements* = 40 the graphs of the analytical and the numerical solution coincide.

Next consider a normalized Gaussian right-hand circular polarized spot that is focused on the aforementioned plane geometry. The NA of the focussing lens is 0.85 and the wave length of the light is 405 nm. This spot will be used in Section 10.3 for the validation of the integrated thermal model. The spot is created with Diffract. For the sampling of the spot, the number of points in the  $x$ - and  $y$ -direction ( $N_x, N_y$ ) are both set equal to 384. The number of grid points contained in one period  $p$  of the grating  $K = 8$ . Table 10.2 shows the relative norms for the six field components of the electromagnetic field for this spot. For this simulation a value *nelements* = 40 is used. From the table it becomes clear that for all field components the relative error is in the order of 1%, which is acceptable. From this points onwards *nelements* = 40 will be used in the Cyclop simulations.

Table 10.2: Relative errors of the six field components of the electromagnetic field for a single incident plane wave and for a Gaussian spot as explained in this section. For those field components of the TE-polarized plane wave that are theoretically equal to zero, no relative error is given since the numerical values of these field components are of the order of  $O(10^{-20})$ .

	plane wave <i>nelements</i> = 20	plane wave <i>nelements</i> = 30	plane wave <i>nelements</i> = 40	Gaussian spot <i>nelements</i> = 40
Relative error of $E_x$	X	X	X	$0.345 \times 10^{-1}$
Relative error of $H_x$	$0.267 \times 10^{-1}$	$0.121 \times 10^{-1}$	$0.685 \times 10^{-2}$	$0.398 \times 10^{-1}$
Relative error of $E_y$	$0.267 \times 10^{-1}$	$0.120 \times 10^{-1}$	$0.674 \times 10^{-2}$	$0.223 \times 10^{-1}$
Relative error of $H_y$	X	X	X	$0.452 \times 10^{-1}$
Relative error of $E_z$	X	X	X	$0.798 \times 10^{-2}$
Relative error of $H_z$	$0.271 \times 10^{-1}$	$0.123 \times 10^{-1}$	$0.695 \times 10^{-2}$	$0.918 \times 10^{-2}$

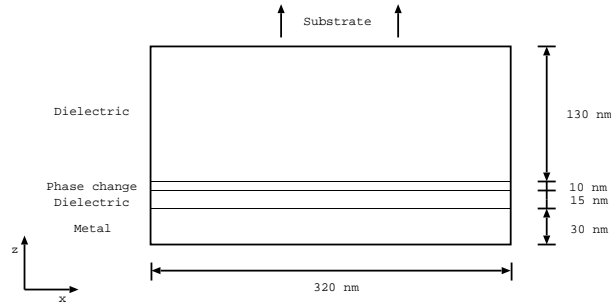


Figure 10.1: An overview of the dimensions of the geometry of the planar structure (i.e. the unit cell) used in the simulations. On top of the upper dielectric layer we consider the half-space to be filled with a substrate. The half-space below the unit cell is filled with metal. The geometry is translation invariant in the  $y$ -direction.

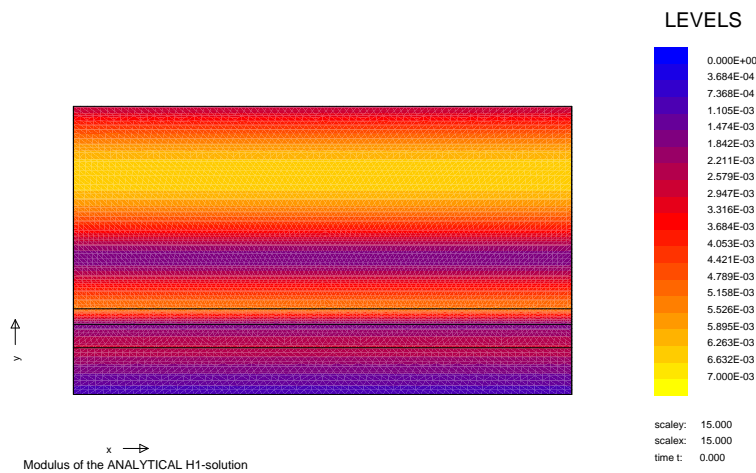


Figure 10.2: The numerically computed modulus of the  $H_x$  component of the TE-polarized plane wave incident on the planar geometry as described in this section. For the generation of the mesh *nelements* is set to 40.

## 10.2 The extension of the Cyclop data

We will now consider the extension of the Cyclop solution from the two-dimensional unit cell (i.e. the main cell) to a three-dimensional region as discussed in Chapter 8. The total number of expanded cells in the  $x$ -direction  $N_p$  is chosen equal to 3 and the total number of clusters in the  $y$ -direction  $N_c = 59$ . Considering the symmetry of the spots that we will use later on, it is convenient to choose the dimensions of the extended region in  $x$ - and  $y$ -direction to be equal. For the distance between two successive clusters  $\Delta c$  it follows that  $\Delta c = 3p/(N_c - 1)$ , where  $p$  is the period length (in  $x$ -direction) of the main cell (and thus of all expanded cells of the extension).

From the extended total electromagnetic field various real quantities can be derived such as the modulus and phase of a field component and the absorbed energy. These quantities are visualized with the Amira program. The dimensions of the rectangular grid on which each expanded cell is mapped are taken as  $N_{cx} = 50$  and  $N_{cz} = 75$ . Since the grid distance of the Amira mesh in  $y$ -direction is chosen to be equal to  $\Delta c$ , the three-dimensional Amira mesh will contain  $148 \times 59 \times 75$  grid points. In all Amira visualizations the period width  $p$  will be normalized.

Let us now consider the Cyclop extension for the incident plane wave from the previous section to give a first impression of a visualization in Amira. Once again we choose the (numerical) modulus of the  $H_x$

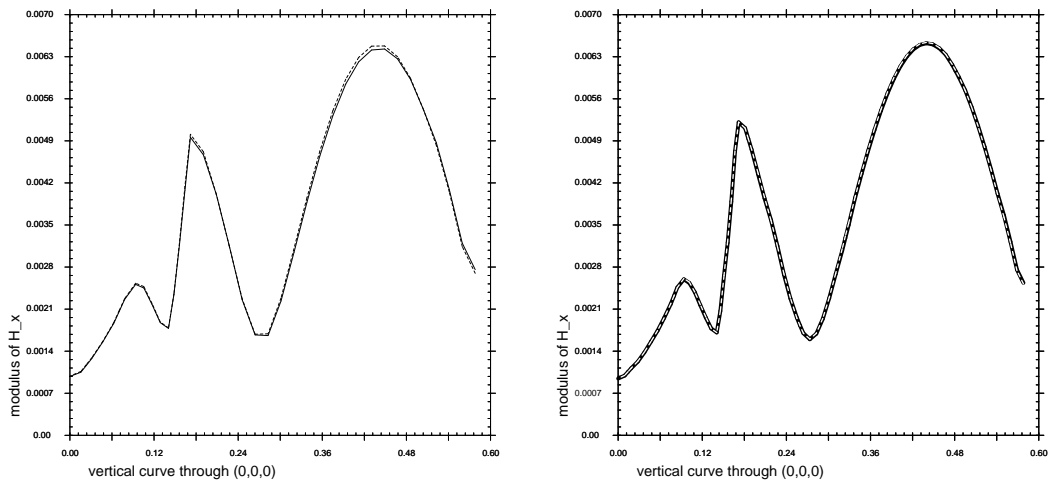


Figure 10.3: Plots of the modulus of  $H_x$  along a vertical curve parallel to the  $z$ -axis. The left graph shows for  $nelements = 20$  the analytical (dashed line) and numerical values. The right graph shows these values for  $nelements = 40$  (white dashed line represents the analytical solution).

component of the total electromagnetic field as our quantity of interest. In Figure 10.4 the extension of this quantity is shown. Unfortunately the color scheme used in the Amira plots can not be chosen equal to the one used in the plots made with Sepran. Figure 10.5 shows the phase of  $H_x$  for the same geometry. Both figures give a good indication of the continuity of the extended data.

Now let us once again consider the Gaussian spot that is focused on the planar geometry from the previous section. For the extension we choose to visualize the modulus and phase of the  $E_y$  component of the total electromagnetic field. A two-dimensional plot of the modulus of  $E_y$  in the main cell is shown in Figure 10.6. It can be seen that only part of the spot is present in the main cell. In Figure 10.7 intersections parallel to the planes  $x = constant$  and  $y = constant$  are shown of the modulus of the extension of  $E_y$ . The left intersection parallel to the  $y$ -axis shows the layers of the geometry. The intersections are positioned such that the region bounded by these intersections corresponds to the main cell (compare with Figure 10.6).

Figure 10.8 shows an intersection parallel to a plane  $z = constant$  through the lower maximum visible in Figure 10.7. The figure clearly shows the continuity of the extended field. In Figure 10.9 an intersection through the upper maximum visible in Figure 10.7 is shown. The field values have been scaled such that the highest elevation level corresponds to the highest value of the field. The shape of the graph has the distinct form of a Gaussian distribution. In Figures 10.7-10.9 the darkest blue corresponds to approximately  $0 V/m$  and the darkest red to the maximum field value. The phase of the extended  $E_y$  is shown in Figure 10.1. A phase jump can be seen from  $-\pi$  (white) to  $\pi$  (yellow) in the upper dielectric layer.

Figures 10.11 and 10.12 show the total electromagnetic energy density  $w$  and the absorbed energy  $W$ , respectively. The only layer in which absorption can clearly be seen is the phase-change layer. The absorbed energy is Gaussian distributed. There is also a small amount of energy absorption at the top of the metal layer, which is t+oo less to be visible in the figure.

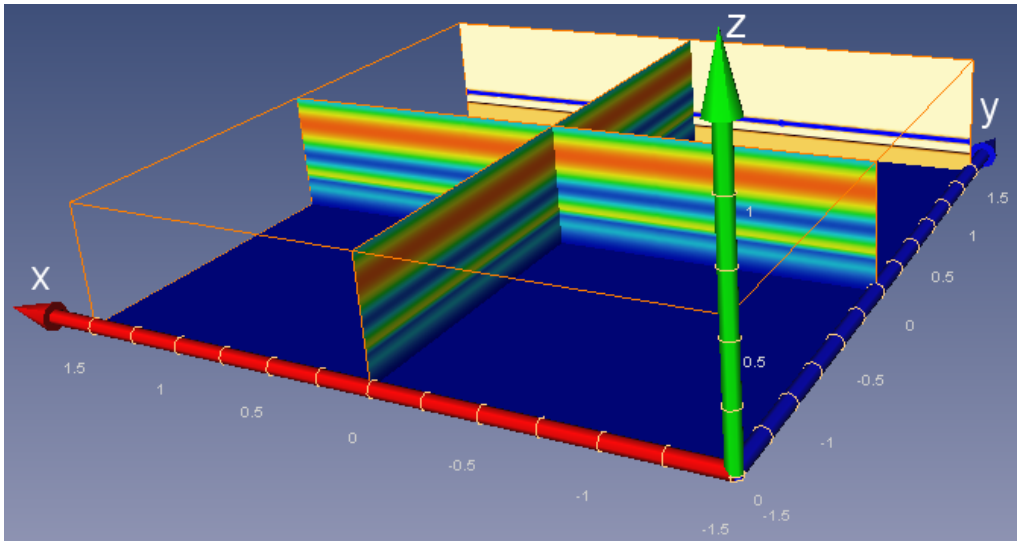


Figure 10.4: The modulus of  $H_x$  of the TE-polarized plane wave that is incident on a planar geometry as described in the previous section. TE-polarized means that the magnetic field is parallel to the x-axis. The wave vector  $k$  lies in the  $(x, z)$ -plane and makes an angle of 52 degrees with the  $z$ -axis. The plane at  $y = 1.5$  shows the layers of the geometry (see Figure 10.1). The darkest blue corresponds to approximately  $0 \text{ A/m}$  and the darkest red corresponds to the maximum field value.

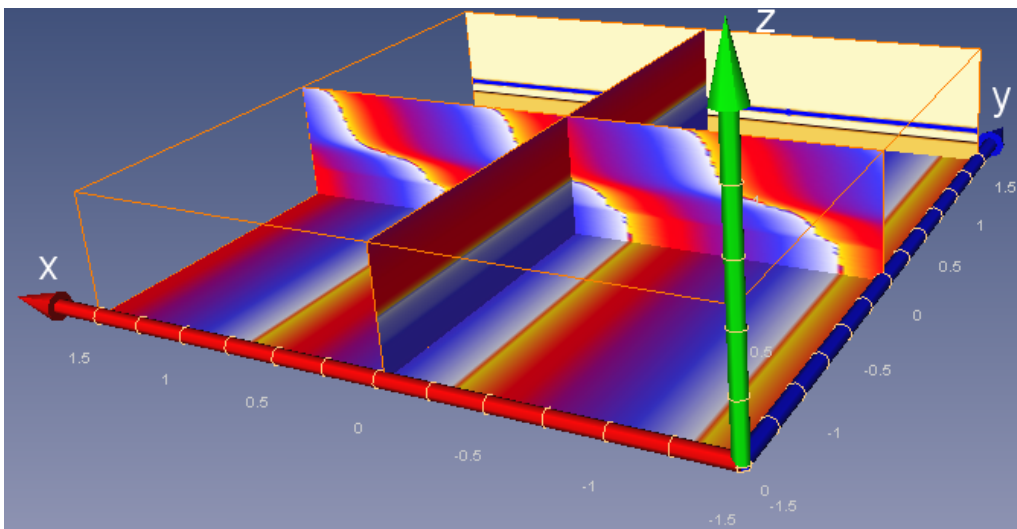


Figure 10.5: The phase of  $H_x$  of the TE-polarized plane wave that is incident on a planar geometry as described in the previous section. The wave vector  $k$  lies in the  $(x, z)$ -plane and makes an angle of 52 degrees with the  $z$ -axis. The plane at  $y = 1.5$  shows the layers of the geometry (see Figure 10.1). White corresponds to  $-\pi$  and yellow to  $\pi$ .

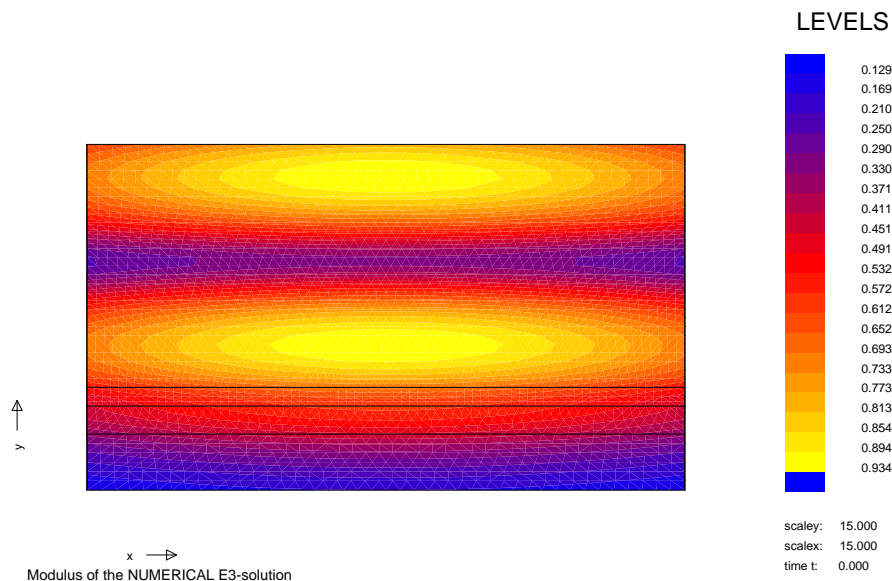


Figure 10.6: The modulus of  $E_y$  in the main cell for the right-hand circular Gaussian spot that is focused on center of the planar geometry, as described in the previous section.

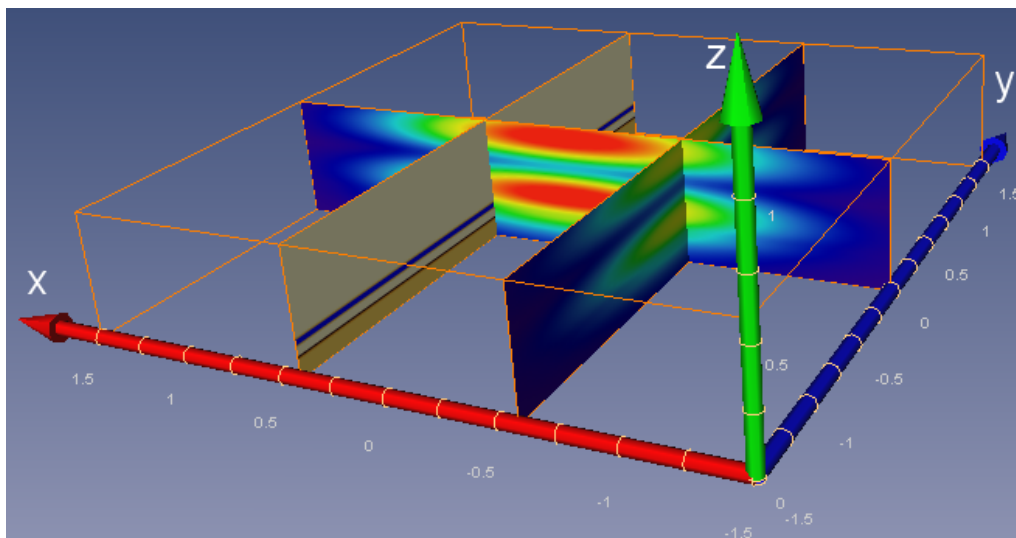


Figure 10.7: The modulus of  $E_y$  for the right-hand circular Gaussian spot that is focused on the center of the planar geometry, as described in the previous section. This geometry is visualized by the plane at  $x = 0.5$ . The darkest blue corresponds to approximately  $0 \text{ V/m}$  and the darkest red to the maximum field value.

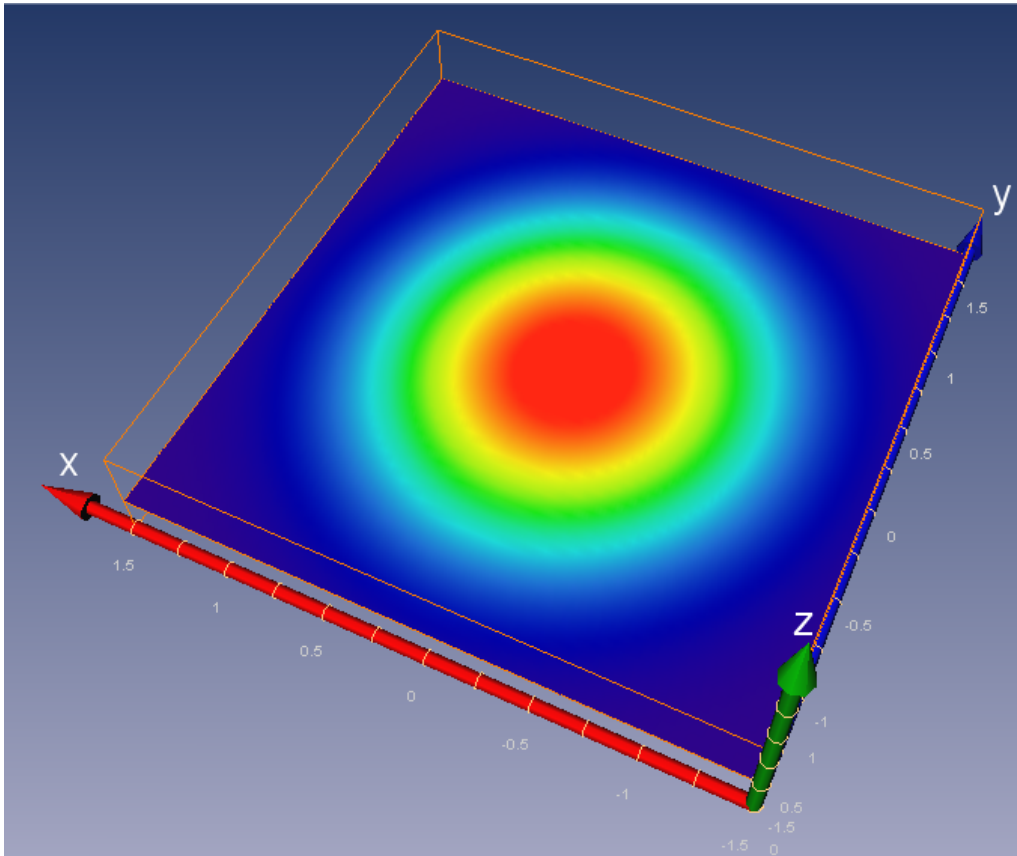


Figure 10.8: The modulus of  $E_y$  for the Gaussian spot in a plane  $z = \text{constant}$  through the bottom maximum as visible in Figures 10.6 and 10.7. The darkest blue corresponds to approximately  $0 \text{ V/m}$  and the darkest red to maximum field value.

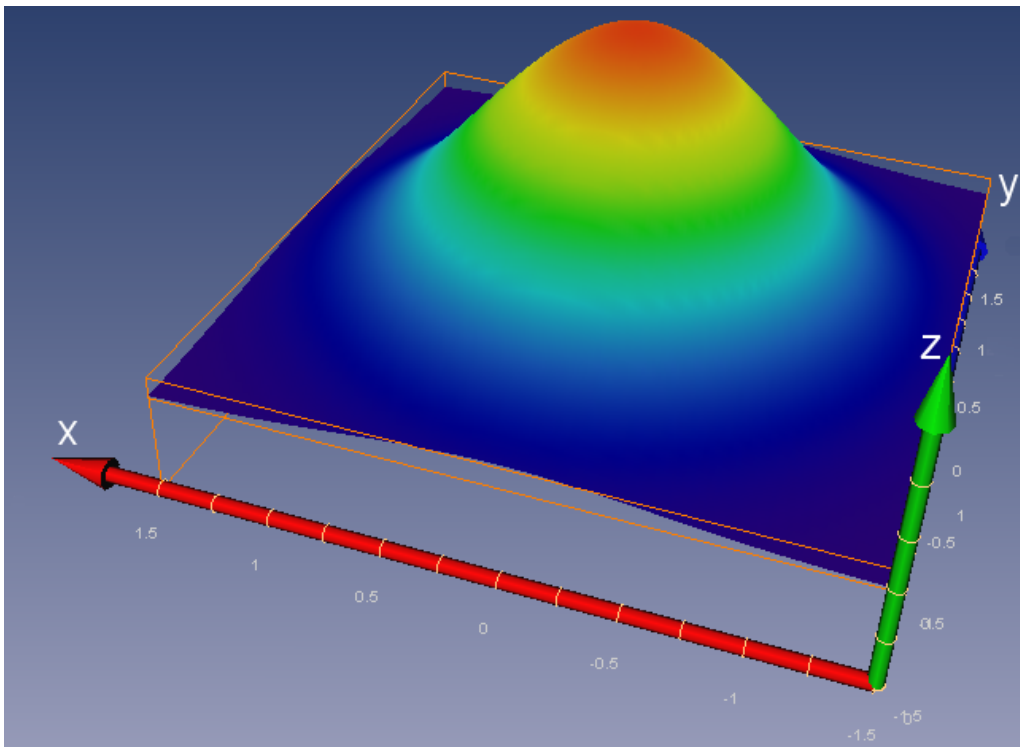


Figure 10.9: The modulus of  $E_y$  for the Gaussian spot a plane  $z = \text{constant}$  through the top maximum as visible in Figures 10.6 and 10.7. The field values have been scaled such that the highest elevation level corresponds to the highest value of the field. The darkest blue corresponds to approximately  $0 \text{ V/m}$  and the darkest red to the maximum field value.

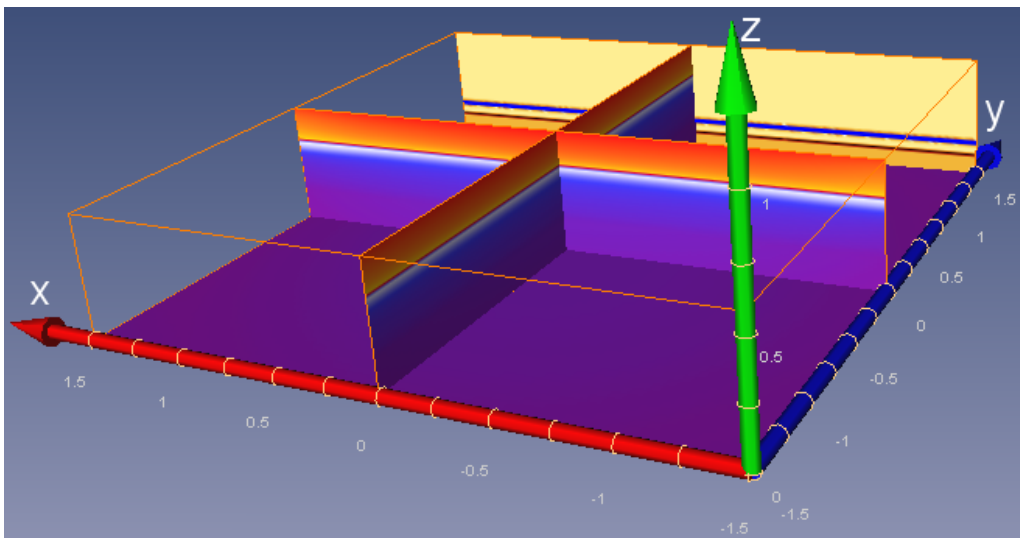


Figure 10.10: The phase of  $E_y$  for the Gaussian spot that is focused on the planar geometry, as described in the previous section. The plane at  $y = 1.5$  shows the layers of the geometry (see Figure 10.1). White corresponds to  $-\pi$  and yellow corresponds to  $\pi$ .

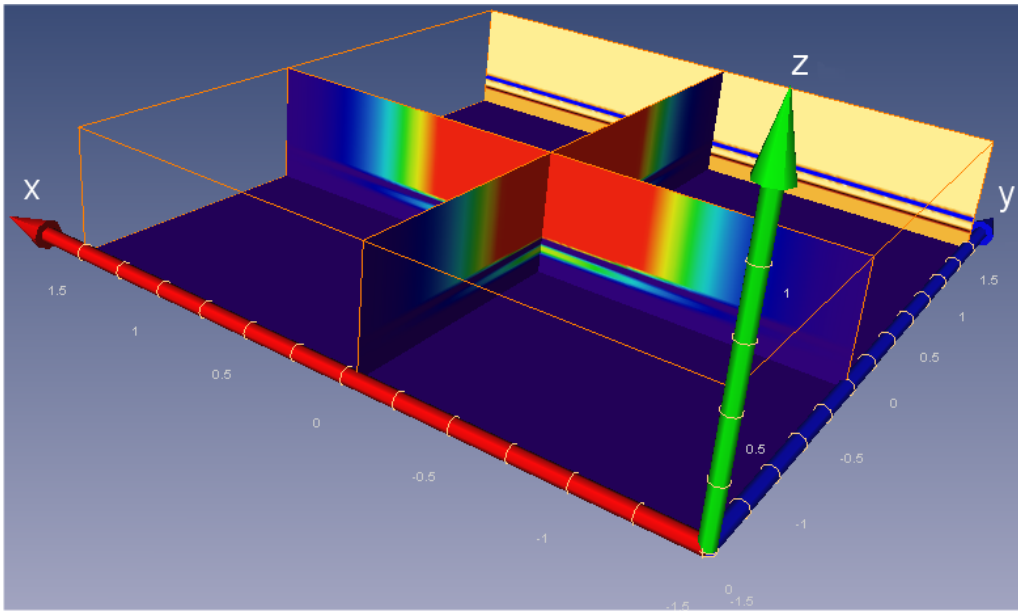


Figure 10.11: The total electromagnetic energy density for the Gaussian spot. The plane at  $y = 1.5$  shows the layers of the geometry (see Figure 10.1). The darkest blue represents an energy level of approximately  $0 \text{ J/m}^3$  and the darkest red represents the maximum energy level.

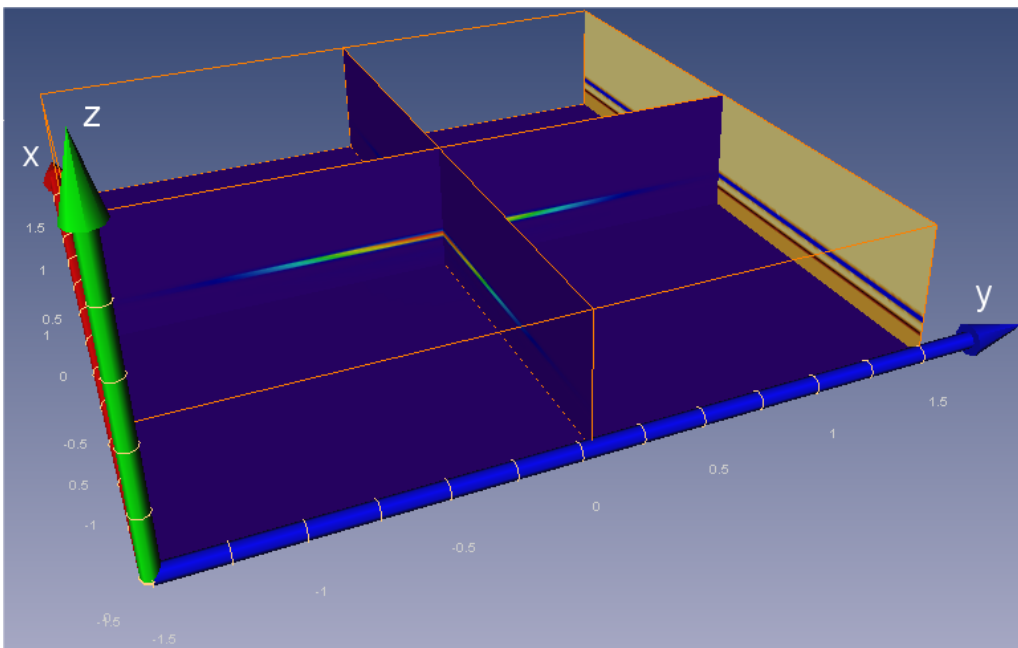


Figure 10.12: The absorbed energy for the Gaussian spot that is focused on the planar geometry, as described in the previous section. The plane at  $y = 1.5$  shows the layers of the geometry (see Figure 10.1). The darkest blue represents an energy level of approximately  $0 \text{ J/m}^3$  and the darkest red represents the maximum energy level.

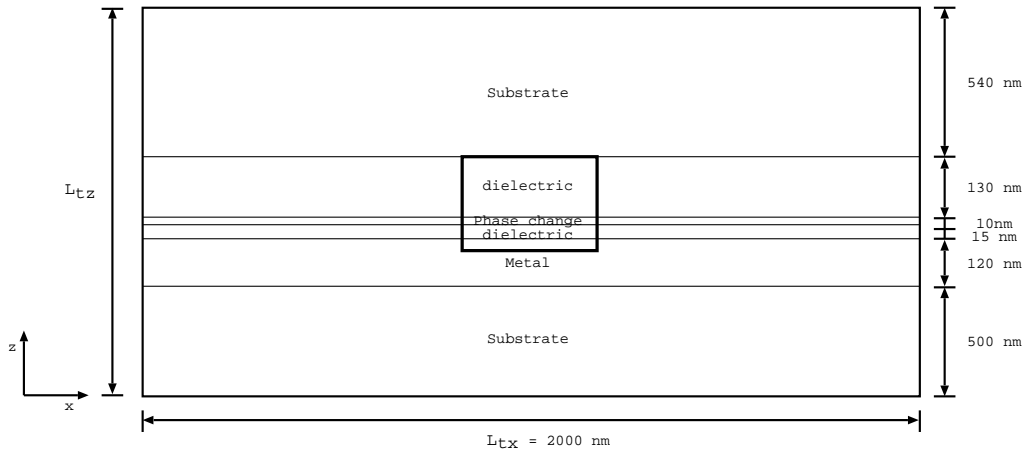


Figure 10.13: The planar geometry used to validate the integrated thermal model. The bounded box shows the position of the main cell (see Figure 10.1). The geometry is translation invariant in the  $y$ -direction.

### 10.3 Validation of the integrated thermal model

The heat source that is obtained rigorously by Cyclop has been integrated in the thermal model as explained in Section 9.3. In this section we will validate this integrated thermal model by comparing the values of the temperature distribution at  $t = 1 \text{ ns}$  and at  $t = 10 \text{ ns}$  with values computed by Media for a planar geometry. The geometry that is used for the validation is shown in Figure 10.13. The geometry is translation invariant in the  $y$ -direction. The dimensions of the thermal computational box are  $L_{tx} = 2 \mu\text{m}$ ,  $L_{ty} = 1.8 \mu\text{m}$  and  $L_{tz} = 1.315 \mu\text{m}$ . For the creation of the thermal mesh, the number of nodal point in  $x$ -,  $y$ - and  $z$ -direction are chosen to be as 50, 40 and 38, respectively. The numerical values of the thermal and optical parameters are listed in Table 10.3.

For the validation the normalized right-hand circular polarized Gaussian spot as specified in Section 10.1 is used. The spot is focused on the center of the geometry (the optical axis coincides with the  $z$ -axis) and is stationary (i.e.  $v = 0$ ). It is switched on for a time of  $100 \text{ ns}$  at constant level. Subsequently, in all thermal simulations the initial temperature is set to 0 in the whole computational box.

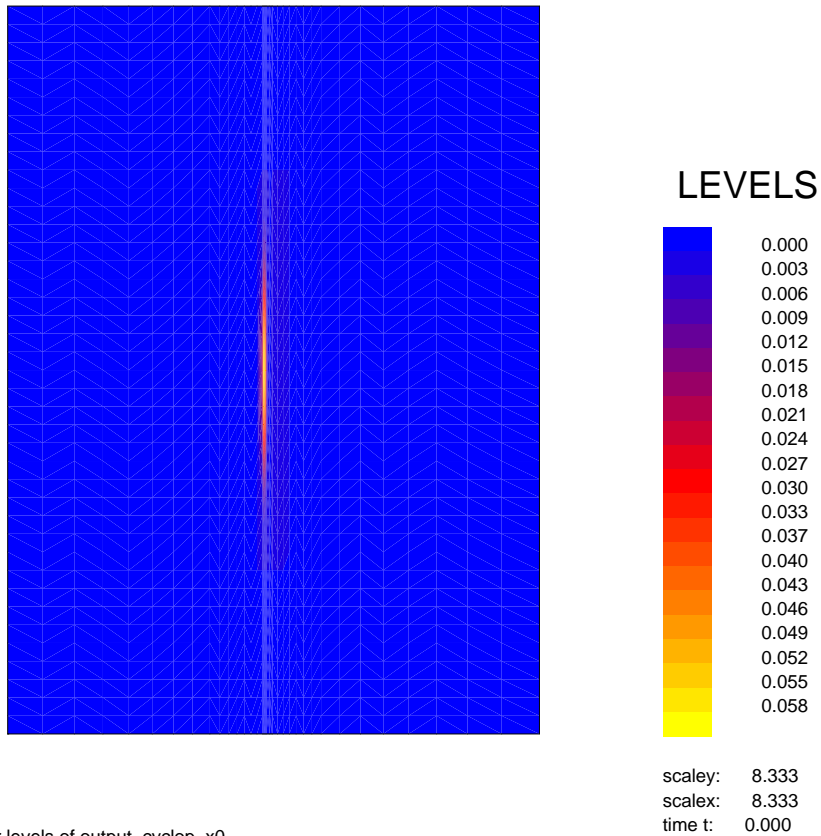
In Figures 10.14 and 10.15 the extended absorbed energy is shown (see also Figure 10.12) integrated into the thermal mesh (i.e. at  $t = 0$ ). Next, we calculate the temperature distribution between  $t = 0 \text{ ns}$  when the spot is turned on and at  $t = 100 \text{ ns}$  when the spot is turned off. In Figures 10.16- 10.18 the temperature distribution at  $t = 1 \text{ ns}$ ,  $t = 10 \text{ ns}$ ,  $t = 50 \text{ ns}$  and  $t = 99 \text{ ns}$  is shown in intersections in a plane  $z = \text{constant}$  halfway in the phase-change layer, the plane  $x = 0$  and the plane  $y = 0$ , respectively. The highest temperatures (yellow) and gradients can be seen in the metal in the center of the spot.

In Figure 10.19 shows cross sections of the temperature  $T(x, 0, z_{\text{half}})$ ,  $T(0, y, z_{\text{half}})$  and  $T(0, 0, z)$  at  $t = 1 \text{ ns}$  and  $t = 10 \text{ ns}$ , where  $z = z_{\text{half}}$  is the plane through the center of the phase-change layer. Notice the symmetry of the Figures 10.19(a)- 10.19(d).

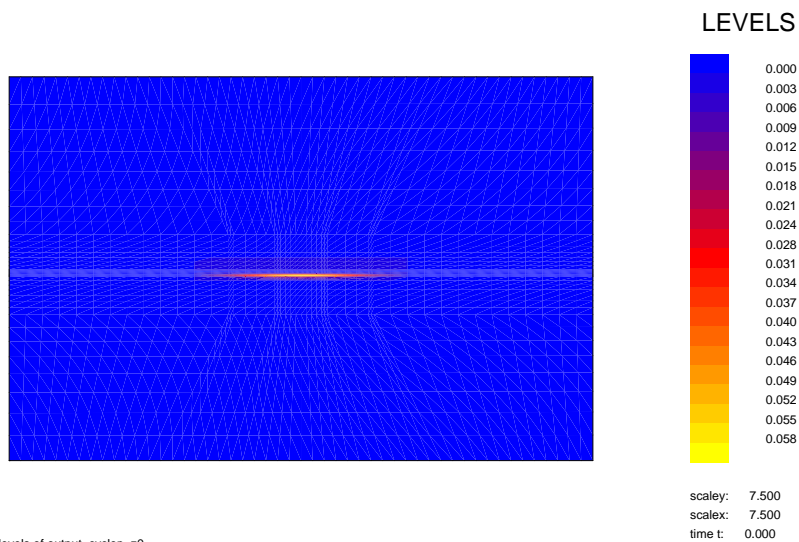
Table 10.3: The numerical values of the indices of refraction  $n$ , heat conductivity  $\kappa$  and the specific heat  $C_p$  of the materials that are used in the simulations. The wave length  $\lambda$  in air is  $405 \text{ nm}$ .

	Index of refraction $n$	$\kappa$ [ $\text{W}/\text{m}/^\circ\text{C}$ ]	$C_p$ [ $\text{J}/\text{kg}/^\circ\text{C}$ ]
Substrate	1.6	0.22	1.5
Metal (aluminium)	$0.17 + 2.04i$	100	2.45
Dielectric material	2.28	0.7	2.05
Phase-change material	$1.52 + 3.36i$	0.5	1.3

In order to validate the results of the integrated thermal model we compare the output with corresponding Media results. The normalized temperature  $T(x, 0, z_{half})$  for  $0 \leq x \leq 1000 \text{ nm}$  for  $t = 1 \text{ ns}$  and  $t = 10 \text{ ns}$  as computed by the integrated thermal model and Media are plotted in Figure 10.20. The temperature distribution at  $t = 1 \text{ ns}$  as computed by the thermal model and by Media match. After  $10 \text{ ns}$  the graph for the integrated thermal model lies clearly higher than that for the Media program. So far, no explanation has been found for this difference.



Contour levels of output\_cyclop\_x0



Contour levels of output\_cyclop\_z0

Figure 10.14: The absorbed energy at  $t = 0$  integrated into the thermal mesh for the circular polarized Gaussian spot that is focused on the center of the planar geometry as described in this section. The upper figure shows a contour plot of the absorbed energy in the plane  $y = 0$  and the spot is incident from the left. The bottom figure shows a contour plot of the absorbed energy in the plane  $x = 0$ . Here the spot is incident from below.

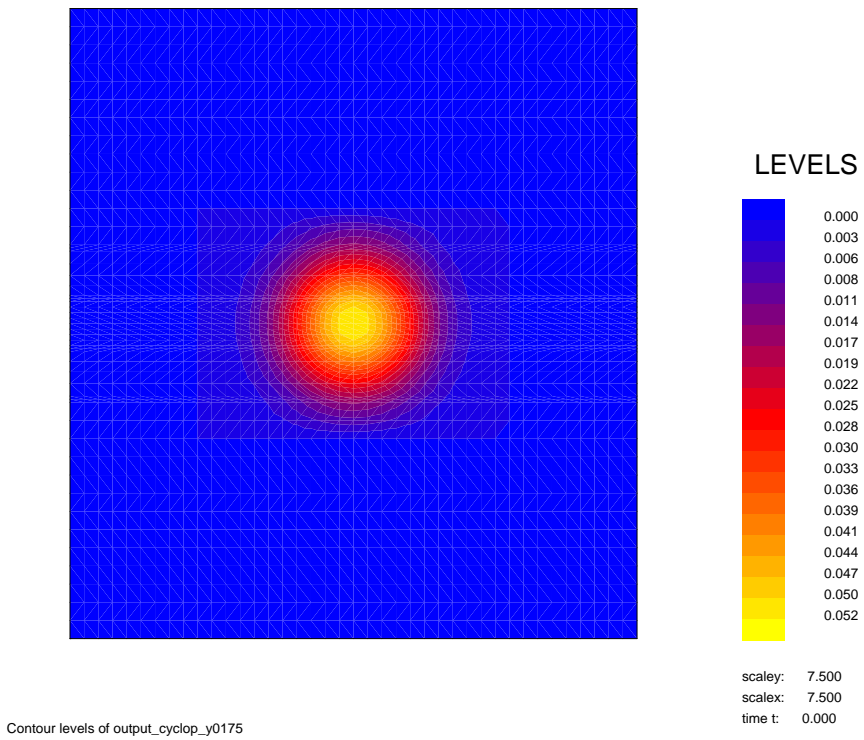


Figure 10.15: A contour plot of the absorbed energy in a plane  $z = \text{constant}$  halfway in the phase-change layer immediately after the beginning of the illumination.

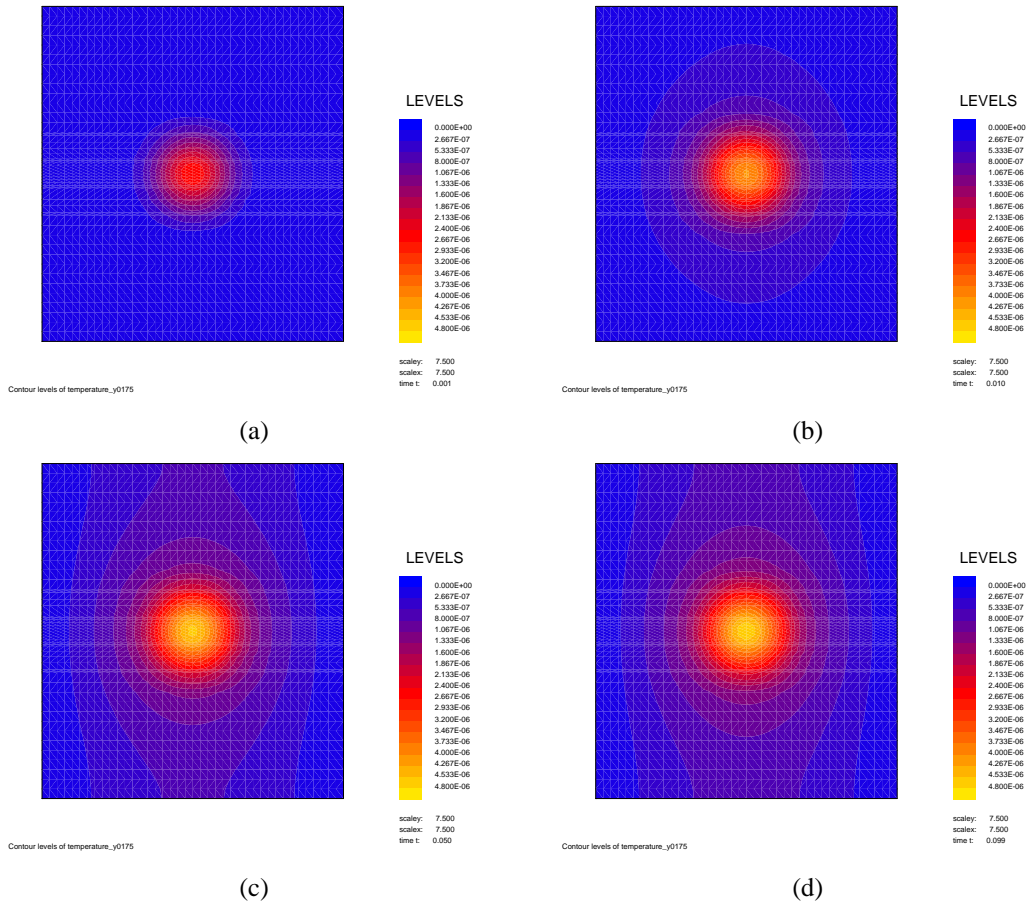


Figure 10.16: Contour plots of the temperature distribution in a plane  $z = \text{constant}$  halfway in the phase-change layer at  $t = 1 \text{ ns}$  (a),  $t = 10 \text{ ns}$  (b),  $t = 50 \text{ ns}$  (c) and  $t = 99 \text{ ns}$  (d).

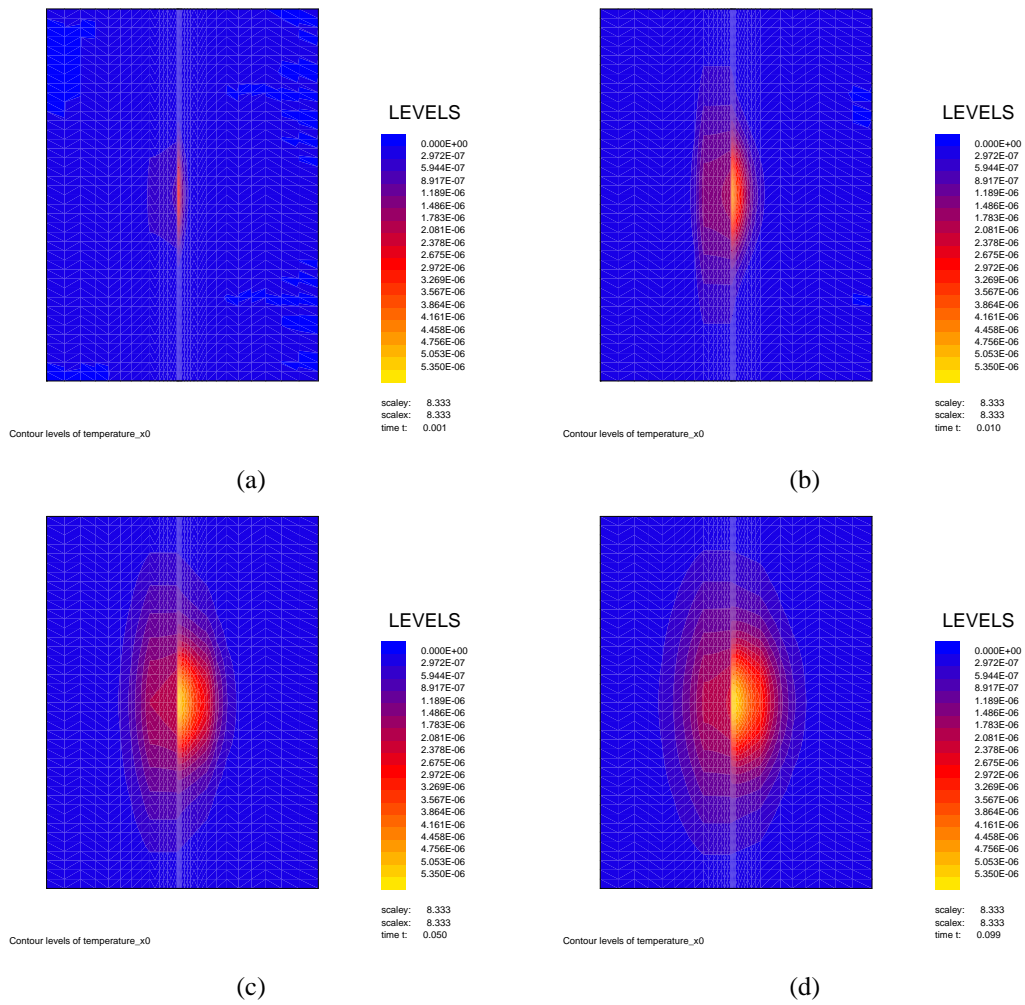


Figure 10.17: Contour plots of the temperature distribution in the plane  $x = 0$  at  $t = 1 \text{ ns}$  (a),  $t = 10 \text{ ns}$  (b),  $t = 50 \text{ ns}$  (c) and  $t = 99 \text{ ns}$  (d). The spot is incident from the left.

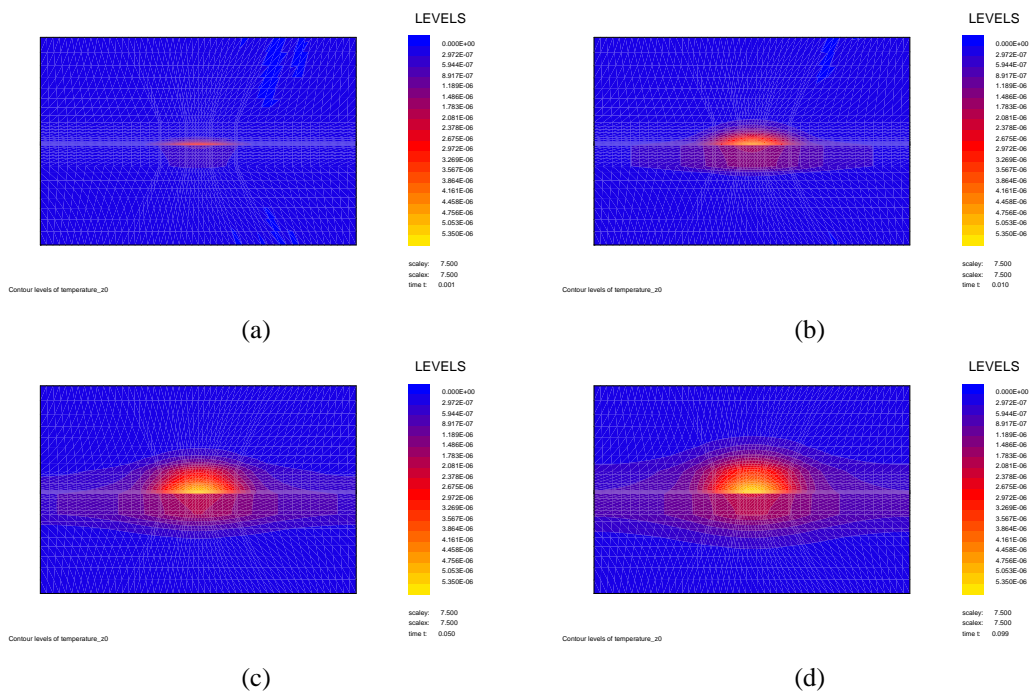


Figure 10.18: Contour plots of the temperature distribution in the plane  $y = 0$  at  $t = 1 \text{ ns}$  (a),  $t = 10 \text{ ns}$  (b),  $t = 50 \text{ ns}$  (c) and  $t = 99 \text{ ns}$  (d). The spot is incident from below.

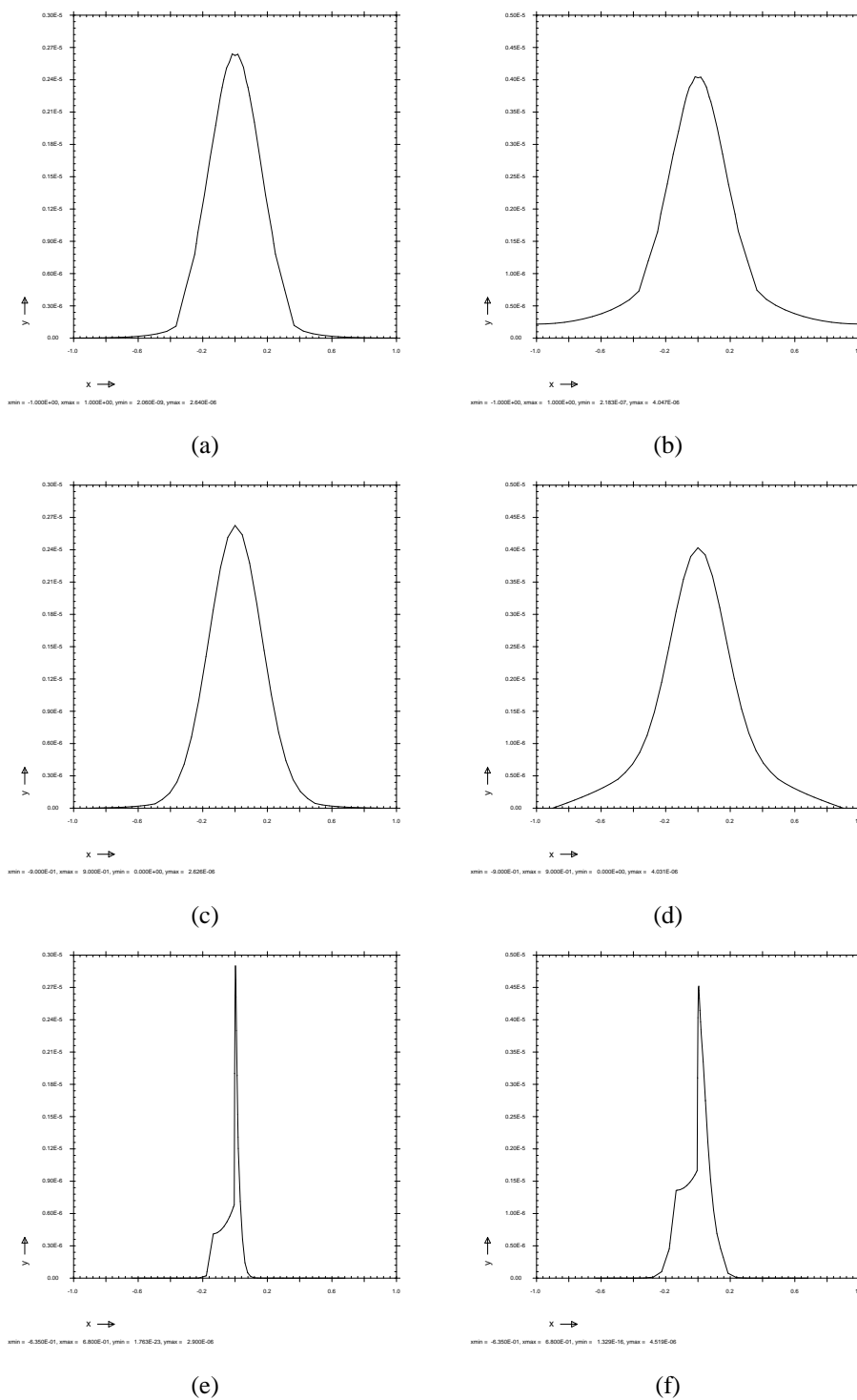


Figure 10.19: Cross sections of the temperature  $T(x, 0, z_{half})$ ,  $T(0, y, z_{half})$  and  $T(0, 0, z)$  at  $t = 1 \text{ ns}$ , (a, c, e) and at  $t = 10 \text{ ns}$ , (b, d, f). The plane  $z = z_{half}$  is the plane halfway in the phase-change layer.

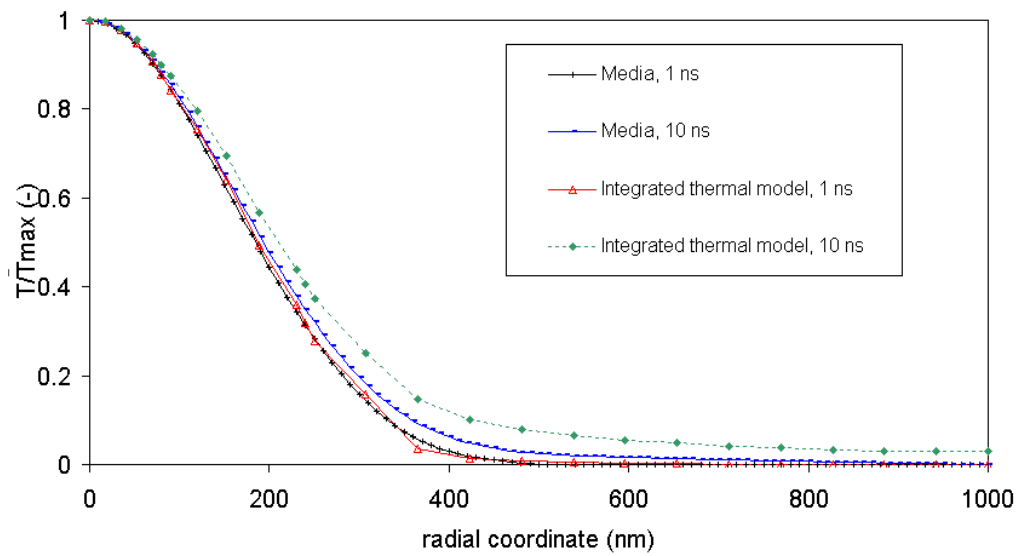


Figure 10.20: The normalized temperature distribution for  $0 \leq x \leq 1 \mu m$ ,  $y = 0$  and  $z = z_{half}$  at  $t = 1 ns$  and at  $t = 10 ns$  as computed by Media and the integrated thermal model.

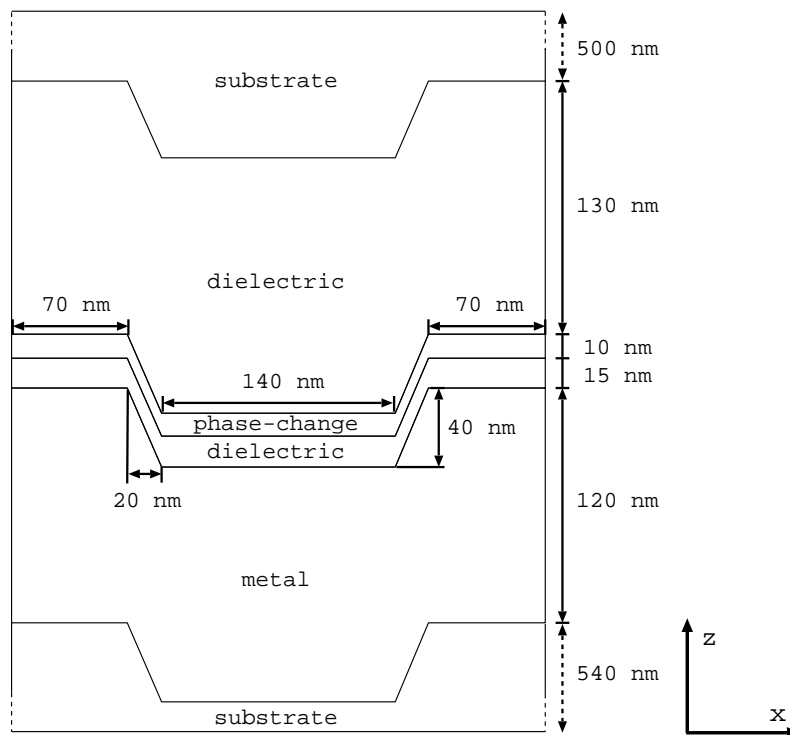


Figure 10.21: One period of the grooved geometry for a BD-disk recording stack. The geometry is translation invariant in the  $y$ -direction and the period width  $p$  is  $320 nm$ .

## 10.4 Stationary spots for a BD-disk recording stack

In this section will consider a normalized predominantly TE-polarized spot and a normalized predominantly TM-polarized spot that are focused on the center of thermal computational box on a groove of a BD-disk recording stack. The optical axis coincides with the  $z$ -axis. Both spots are created with Diffract. For the sampling of the spots, the number of points in  $x$ - and  $y$ -direction ( $N_x, N_y$ ) are both set equal to 384. The number of grid points contained in one period  $p$  of the grating  $K = 8$ . The spots are stationary, i.e.  $v = 0$  m/s.

One period of the geometry of the grooved BD-disk recording stack is shown in Figure 10.21. The optical and thermal properties of the materials are the same as for the planar geometry from the previous sections and are listed in Table 10.3. For the creation of the thermal mesh, the number of nodal point in  $x$ -,  $y$ - and  $z$ -direction are chosen to be as 60, 40 and 38, respectively.

The groove depth of 40 nm has purposely been chosen larger than the actual groove depth of the BD-disk format ( $\approx 23$  nm) in order to make the differences between the two polarizations more distinct. The same argument applies to the slope angle ( $\approx 63$  degrees with the  $z$ -axis instead of  $\approx 30$  degrees for a BD-disk) and the thermal properties that are also not equal to the values of the BD-disk standard.

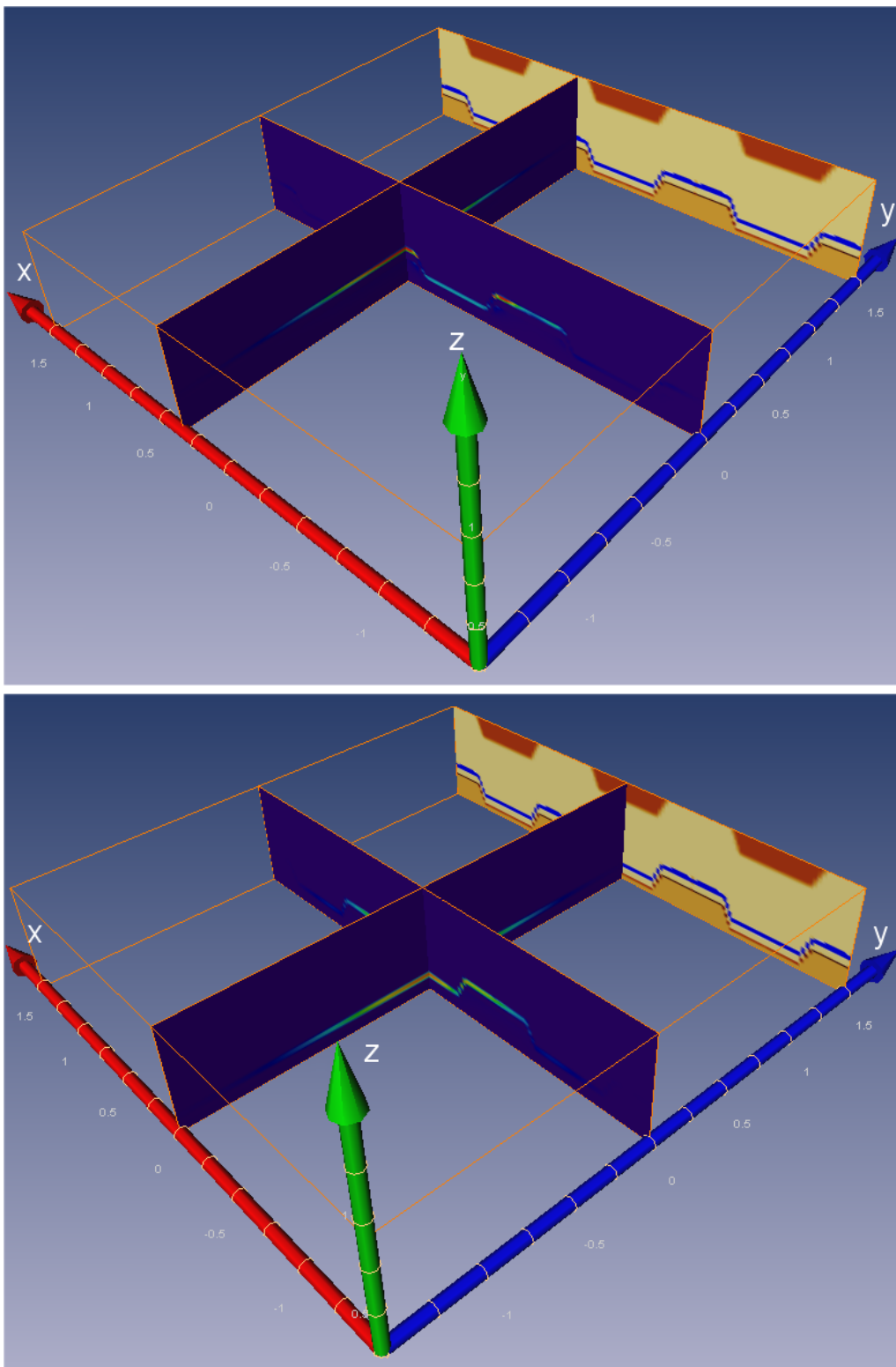


Figure 10.22: Absorbed energy for a normalized predominantly TE-polarized (top figure) and a normalized predominantly TM-polarized spot (bottom figure), focused on the center of the geometry on a groove. See also Figure 10.23. The plane at  $y = 1.5$  shows the grooved geometry. In both figures the darkest blue corresponds to approximately  $0 \text{ W/m}^3$ . The darkest red corresponds to the maximum energy level.

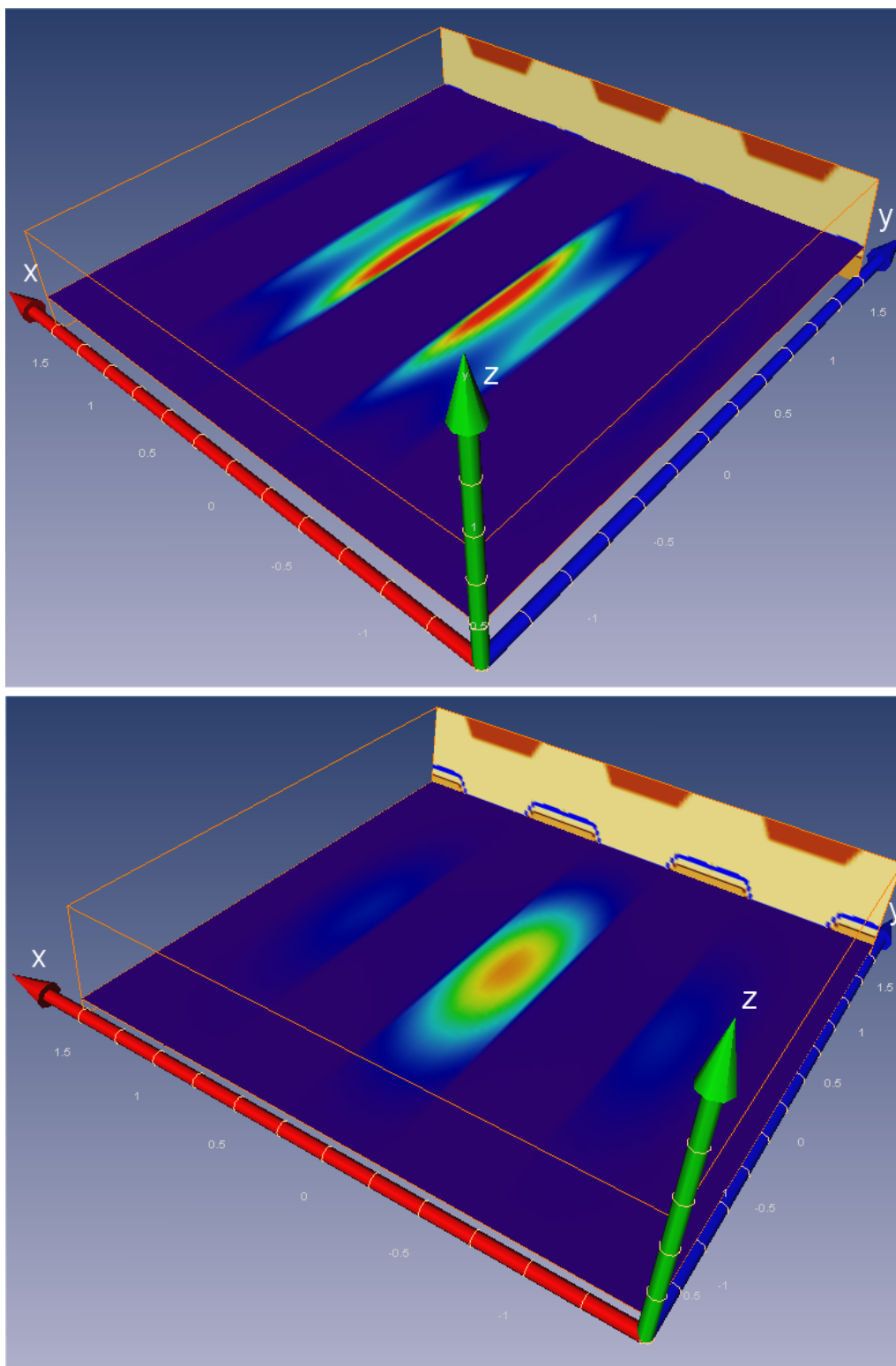


Figure 10.23: Absorbed energy for a normalized predominantly TE-polarized (top figure) and a normalized predominantly TM-polarized spot (bottom figure), focused on the center of the geometry on a groove. The plane at  $y = 1.5$  shows the grooved geometry. In both figures the darkest blue corresponds to approximately  $0 \text{ W/m}^3$ . The darkest red corresponds to the maximum energy level.

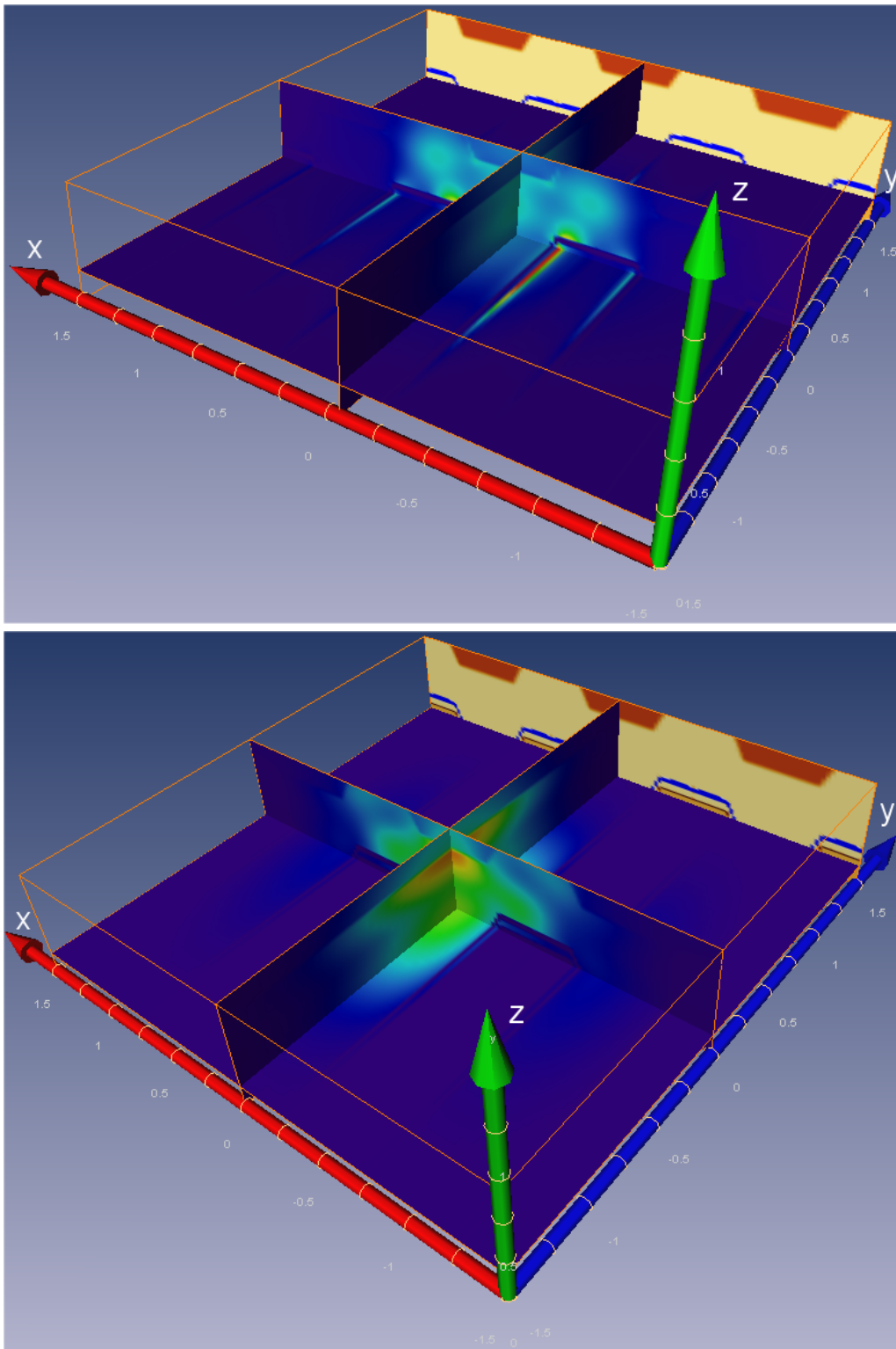


Figure 10.24: Total electromagnetic energy density for a normalized predominantly TE-polarized (top figure) and a normalized predominantly TM-polarized spot (bottom figure), focused on the center of the geometry on a groove. The plane at  $y = 1.5$  shows the grooved geometry. In both figures the darkest blue corresponds to approximately  $0 \text{ J/m}^3$ . The darkest red corresponds to the maximum energy level.

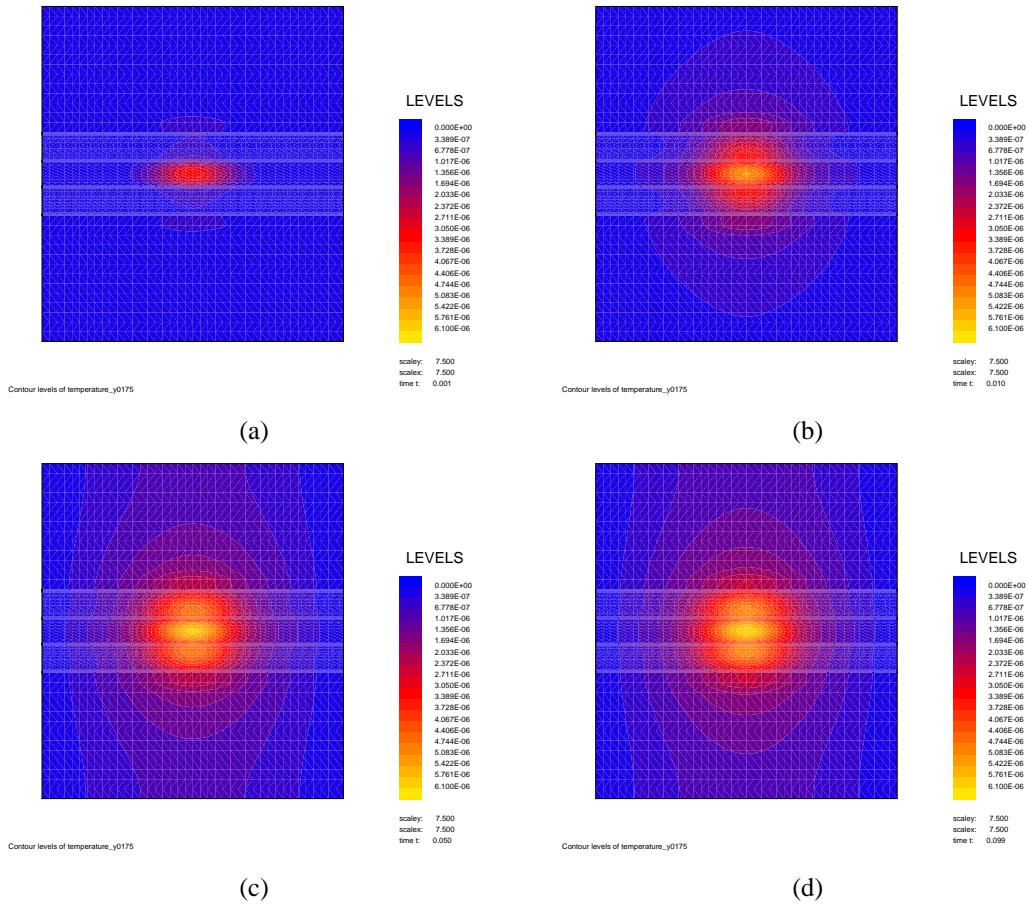


Figure 10.25: Contour plots of the temperature distribution in a plane  $z = \text{constant}$  halfway in the phase-change layer in the groove at  $t = 1 \text{ ns}$  (a),  $t = 10 \text{ ns}$  (b),  $t = 50 \text{ ns}$  (c) and  $t = 99 \text{ ns}$  (d). The spot is predominantly TM-polarized.

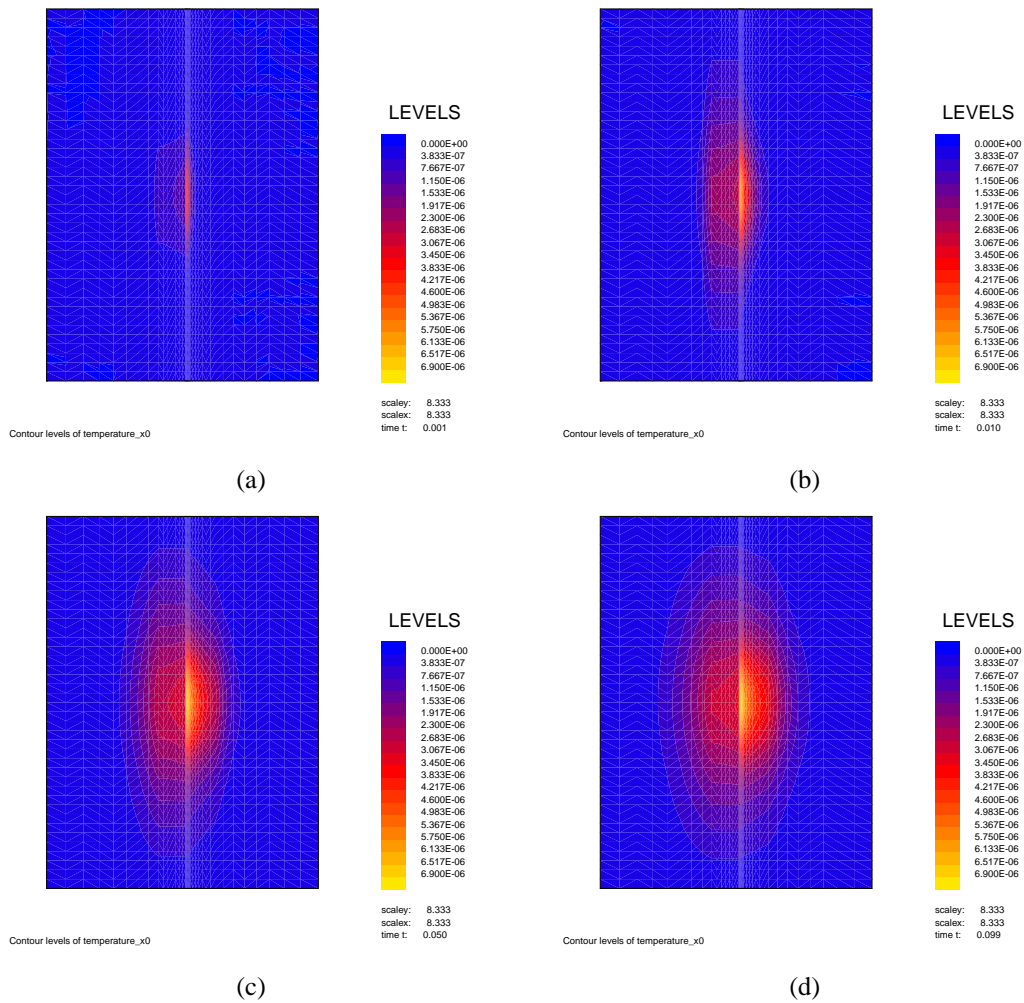


Figure 10.26: Contour plots of the temperature distribution in the plane  $x = 0$  at  $t = 1 \text{ ns}$  (a),  $t = 10 \text{ ns}$  (b),  $t = 50 \text{ ns}$  (c) and  $t = 99 \text{ ns}$  (d). The spot is predominantly TM-polarized.

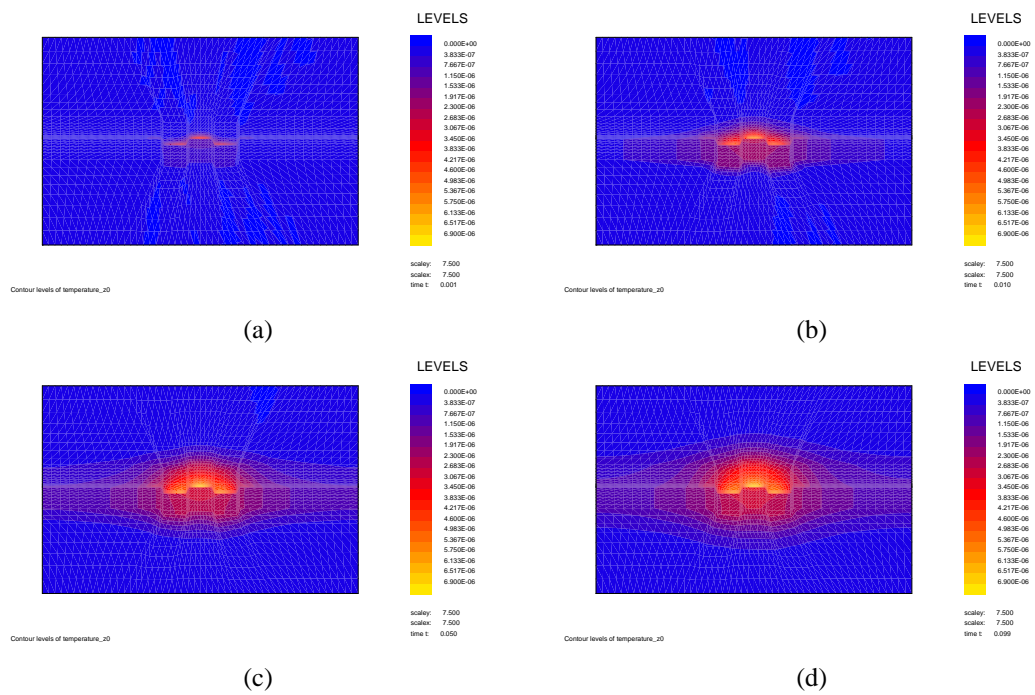


Figure 10.27: Contour plots of the temperature distribution in the plane  $y = 0$  at  $t = 1 \text{ ns}$  (a),  $t = 10 \text{ ns}$  (b),  $t = 50 \text{ ns}$  (c) and  $t = 99 \text{ ns}$  (d). The spot is predominantly TM-polarized.

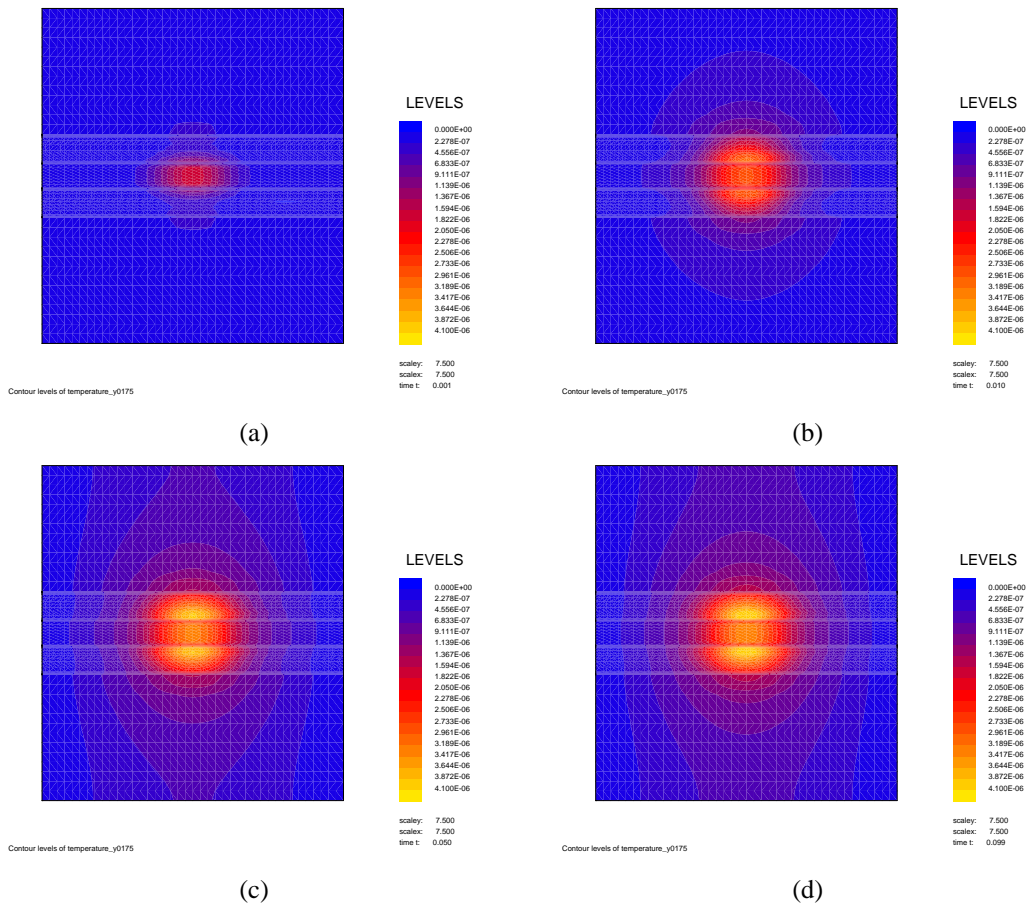


Figure 10.28: Contour plots of the temperature distribution in a plane  $z = \text{constant}$  halfway in the phase-change layer in the groove at  $t = 1 \text{ ns}$  (a),  $t = 10 \text{ ns}$  (b),  $t = 50 \text{ ns}$  (c) and  $t = 99 \text{ ns}$  (d). The spot is predominantly TE-polarized.

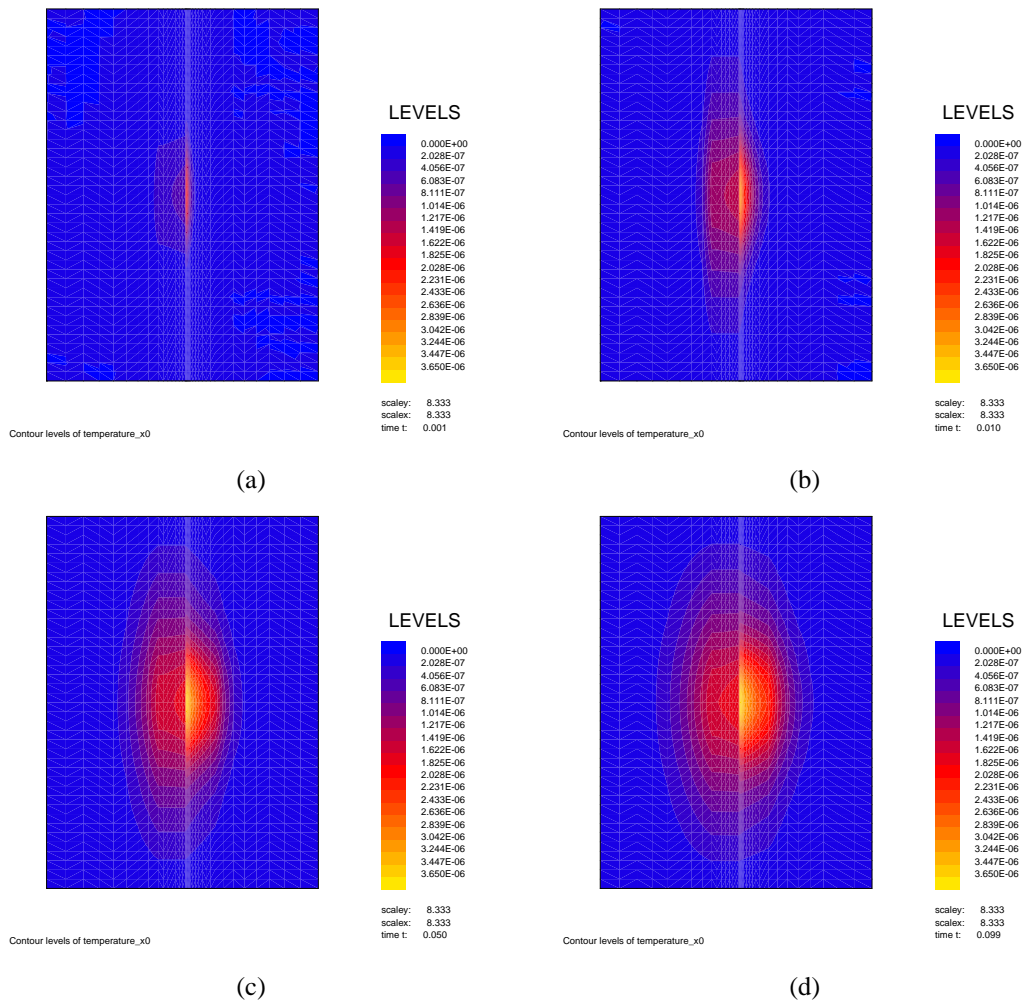


Figure 10.29: Contour plots of the temperature distribution in the plane  $x = 0$  at  $t = 1 \text{ ns}$  (a),  $t = 10 \text{ ns}$  (b),  $t = 50 \text{ ns}$  (c) and  $t = 99 \text{ ns}$  (d). The spot is predominantly TE-polarized.

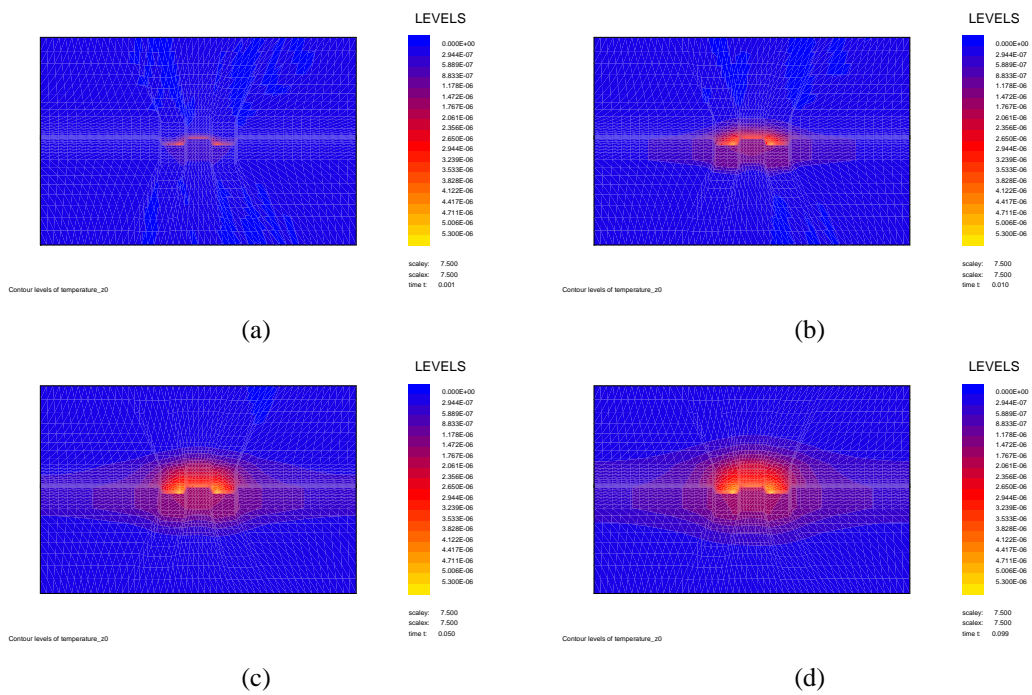


Figure 10.30: Contour plots of the temperature distribution in the plane  $y = 0$  at  $t = 1 \text{ ns}$  (a),  $t = 10 \text{ ns}$  (b),  $t = 50 \text{ ns}$  (c) and  $t = 99 \text{ ns}$  (d). The spot is predominantly TE-polarized.

## 10.5 Moving spots for a BD-stack

Let us now once again consider the predominantly TE- and TM-polarized spots from the previous section that are focused on the BD recording stack. At  $t = 0$  the extended Cyclop absorption data is mapped to the thermal mesh such that the front cluster of the Cyclop extension ( $N_c = -29$ ) coincides with the plane  $y = y_{min}$  of the thermal mesh. The origin of the thermal computational box is placed in the center of the spot at  $t = 0$ . The spots move at a speed  $v = 9.48 \text{ m/s}$  along the center groove of the geometry.

In Figures 10.31 - 10.33 contour plots of the temperature distribution are shown for the predominantly TM-polarized spot and in Figures 10.34 - 10.36 for the predominantly TE-polarized spot.

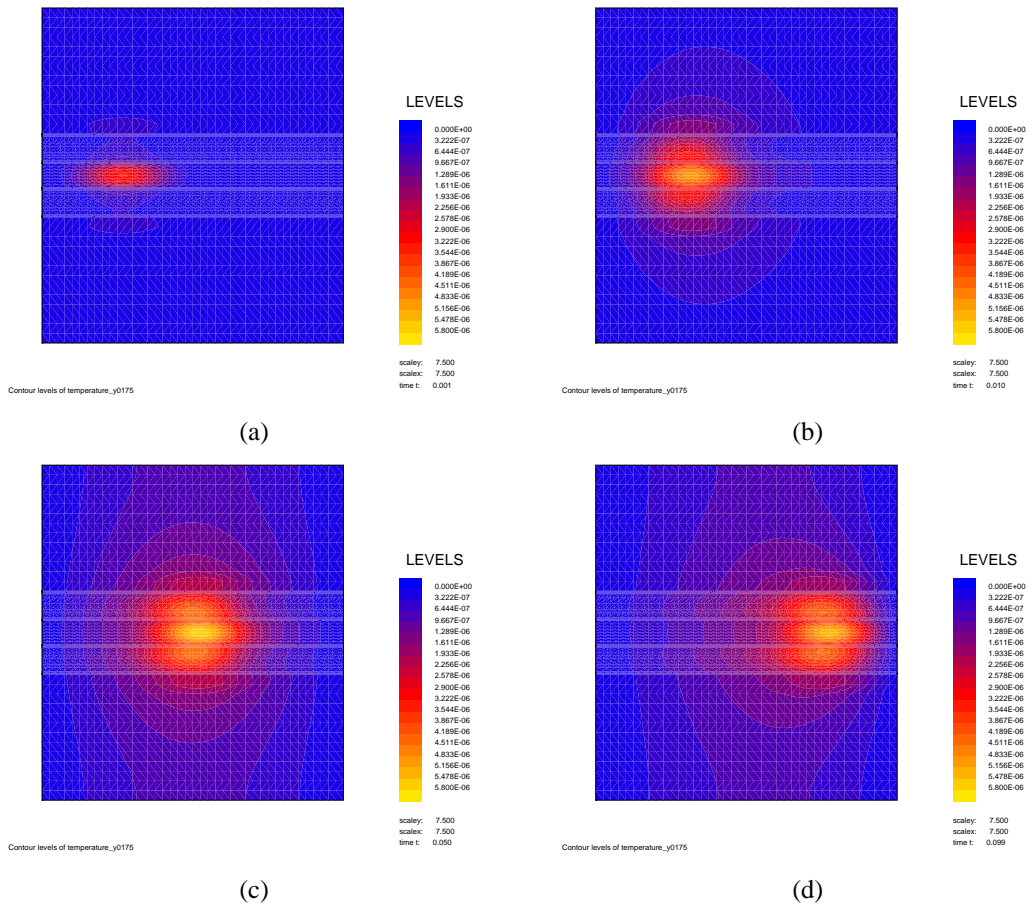


Figure 10.31: Contour plots of the temperature distribution in a plane  $z = \text{constant}$  through the center of the phase-change layer in the groove at  $t = 1 \text{ ns}$  (a),  $t = 10 \text{ ns}$  (b),  $t = 50 \text{ ns}$  (c) and  $t = 99 \text{ ns}$  (d). The spot is predominantly TM-polarized and moves at a speed of  $9.48 \text{ m/s}$ .

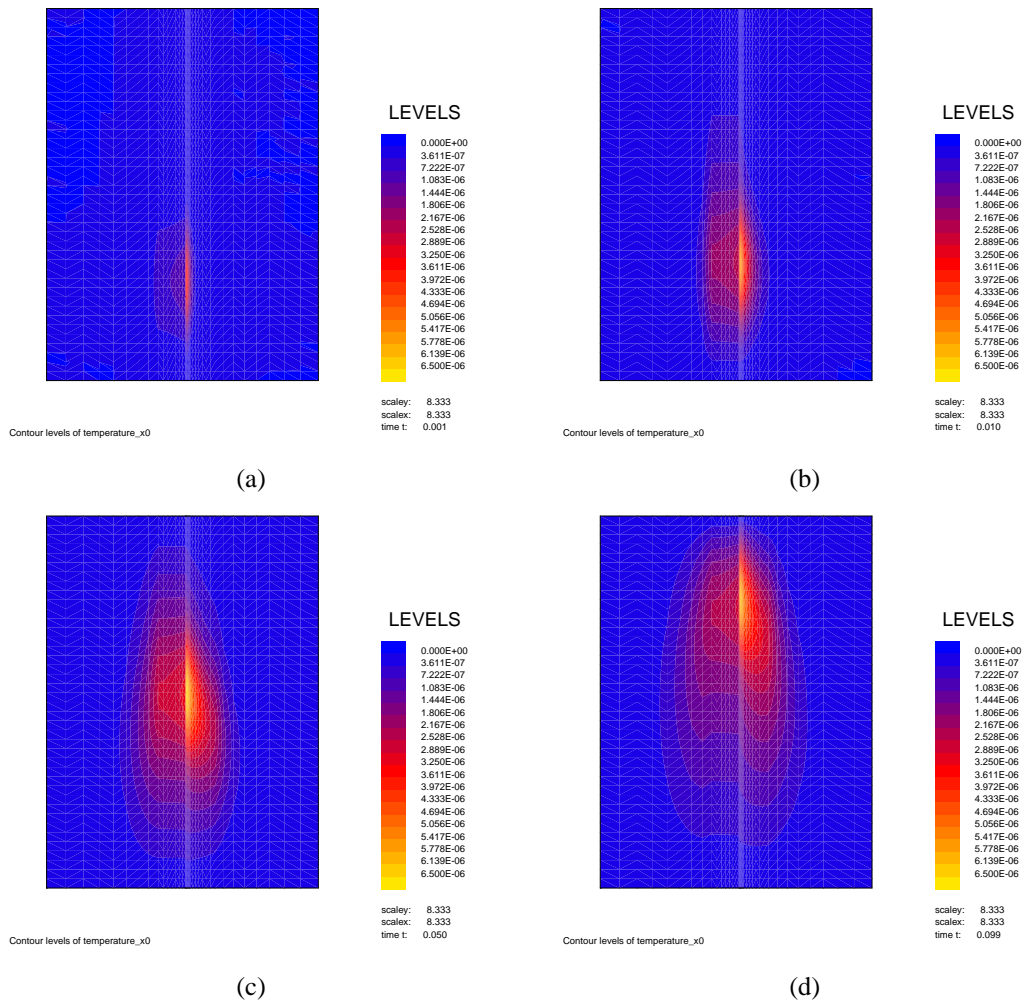


Figure 10.32: Contour plots of the temperature distribution in the plane  $x = 0$  at  $t = 1 \text{ ns}$  (a),  $t = 10 \text{ ns}$  (b),  $t = 50 \text{ ns}$  (c) and  $t = 99 \text{ ns}$  (d). The spot is predominantly TM-polarized and moves at a speed of  $9.48 \text{ m/s}$ .

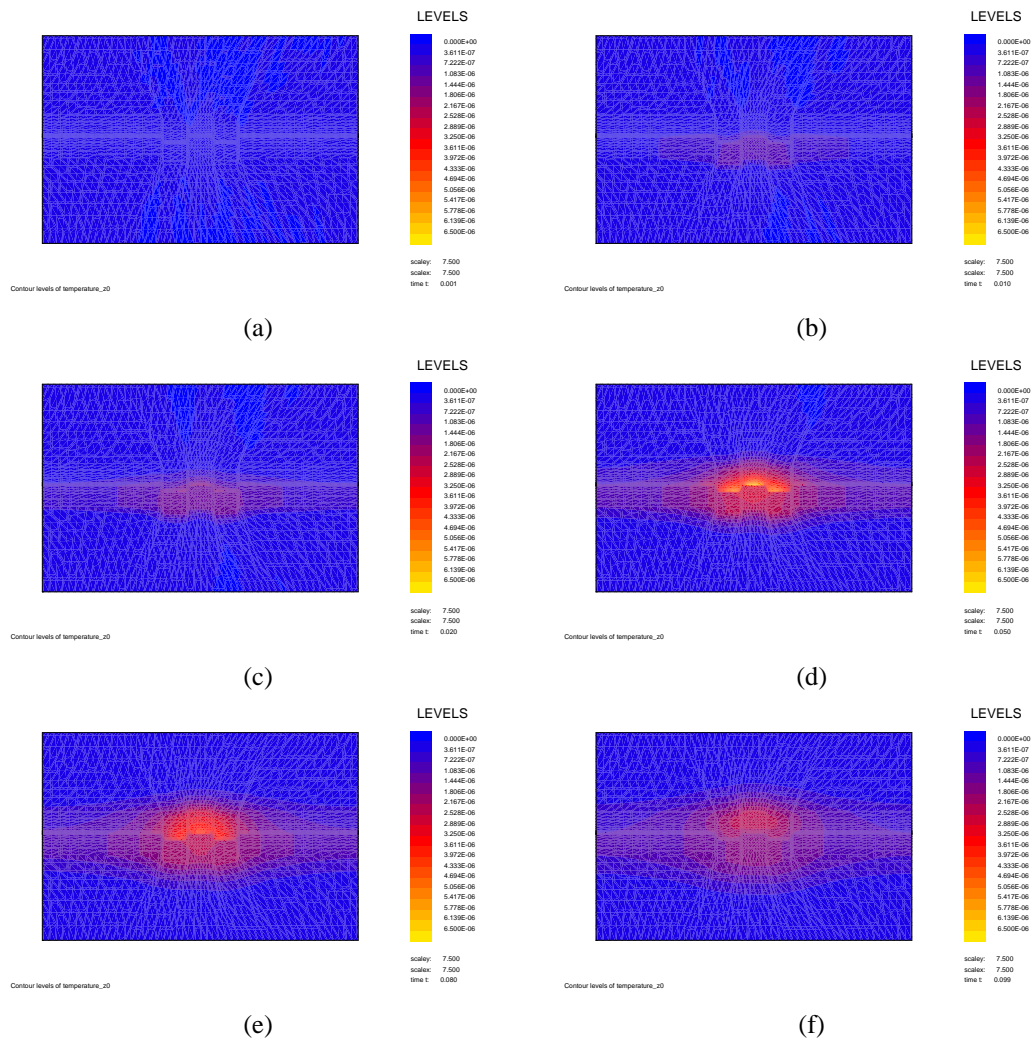


Figure 10.33: Contour plots of the temperature distribution in a plane  $y = \text{constant}$  through the middle of the computational box at  $t = 1 \text{ ns}$  (a),  $t = 10 \text{ ns}$  (b),  $t = 20 \text{ ns}$  (c),  $t = 50 \text{ ns}$  (d),  $t = 80 \text{ ns}$  (e) and  $t = 99 \text{ ns}$  (f). The spot is predominantly TM-polarized and moves at a speed of  $9.48 \text{ m/s}$ .

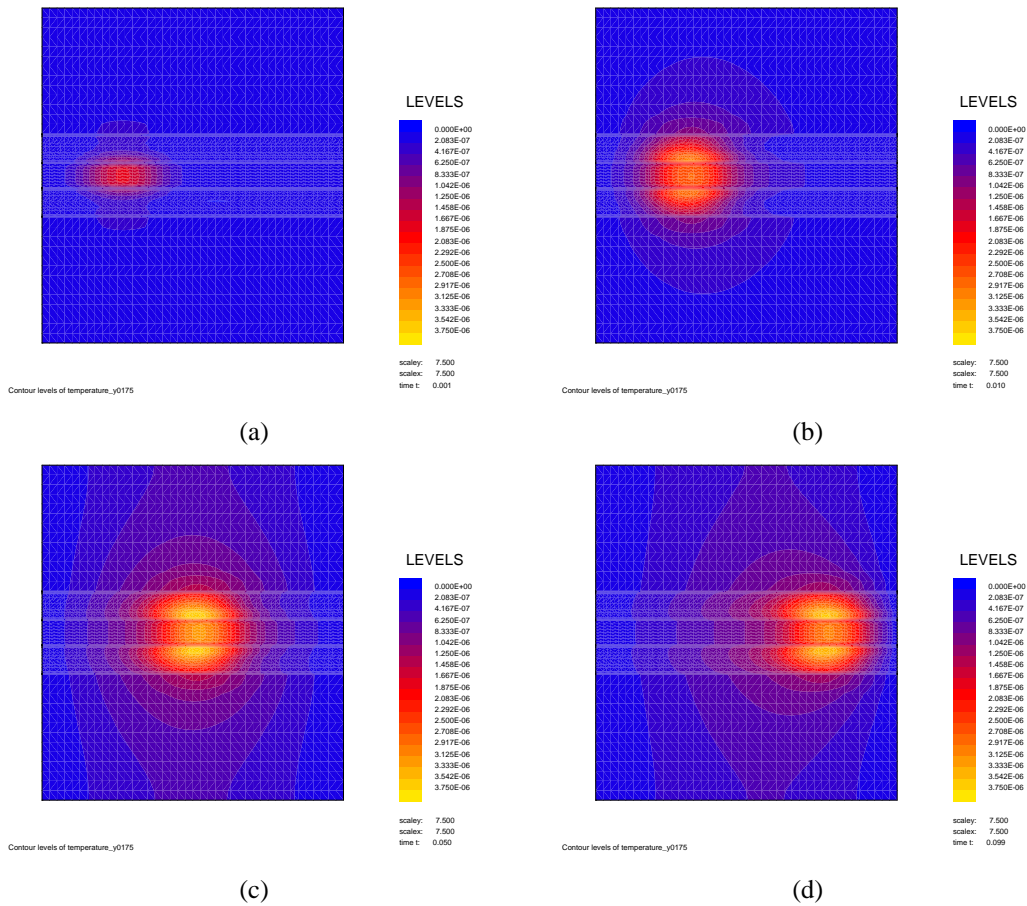


Figure 10.34: Contour plots of the temperature distribution in a plane  $z = \text{constant}$  through the center of the phase-change layer in the groove at  $t = 1 \text{ ns}$  (a),  $t = 10 \text{ ns}$  (b),  $t = 50 \text{ ns}$  (c) and  $t = 99 \text{ ns}$  (d). The spot is predominantly TE-polarized and moves at a speed of  $9.48 \text{ m/s}$ .

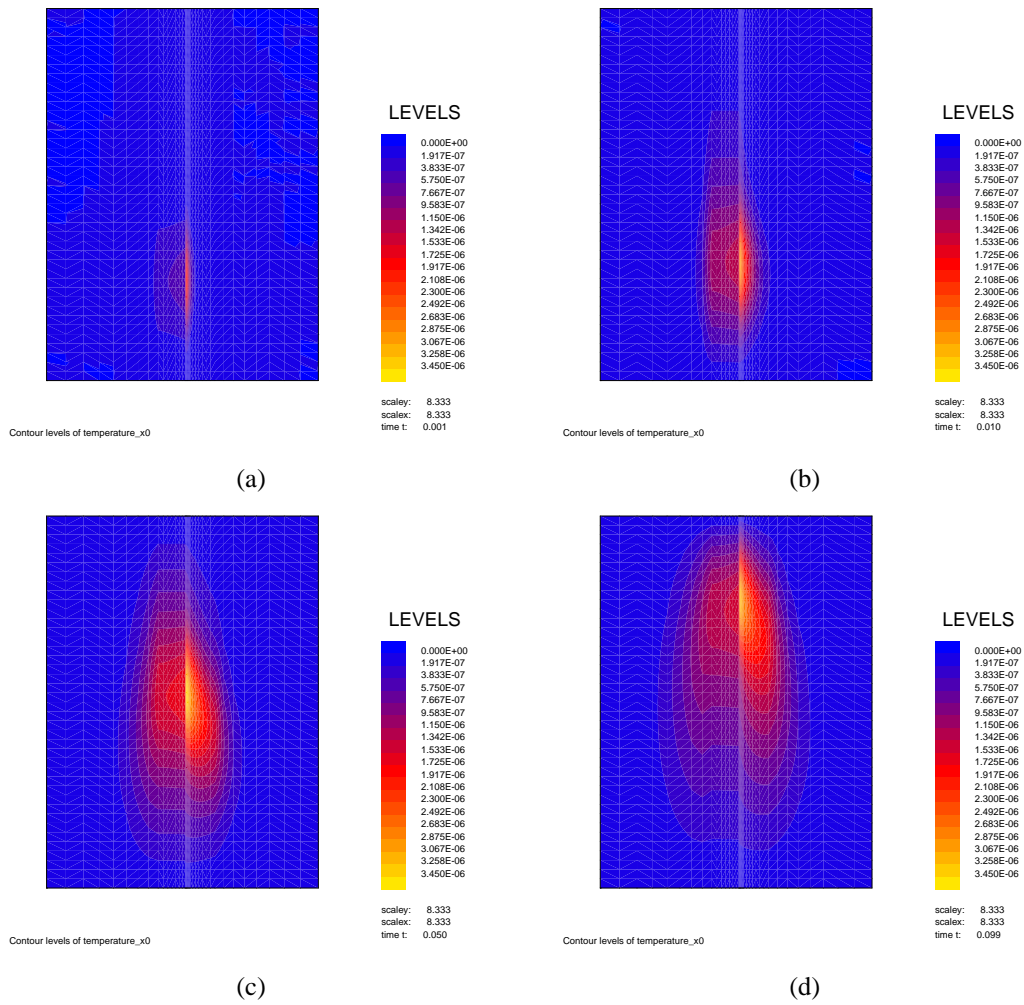


Figure 10.35: Contour plots of the temperature distribution in the plane  $x = 0$  at  $t = 1 \text{ ns}$  (a),  $t = 10 \text{ ns}$  (b),  $t = 50 \text{ ns}$  (c) and  $t = 99 \text{ ns}$  (d). The spot is predominantly TE-polarized and moves at a speed of  $9.48 \text{ m/s}$ .

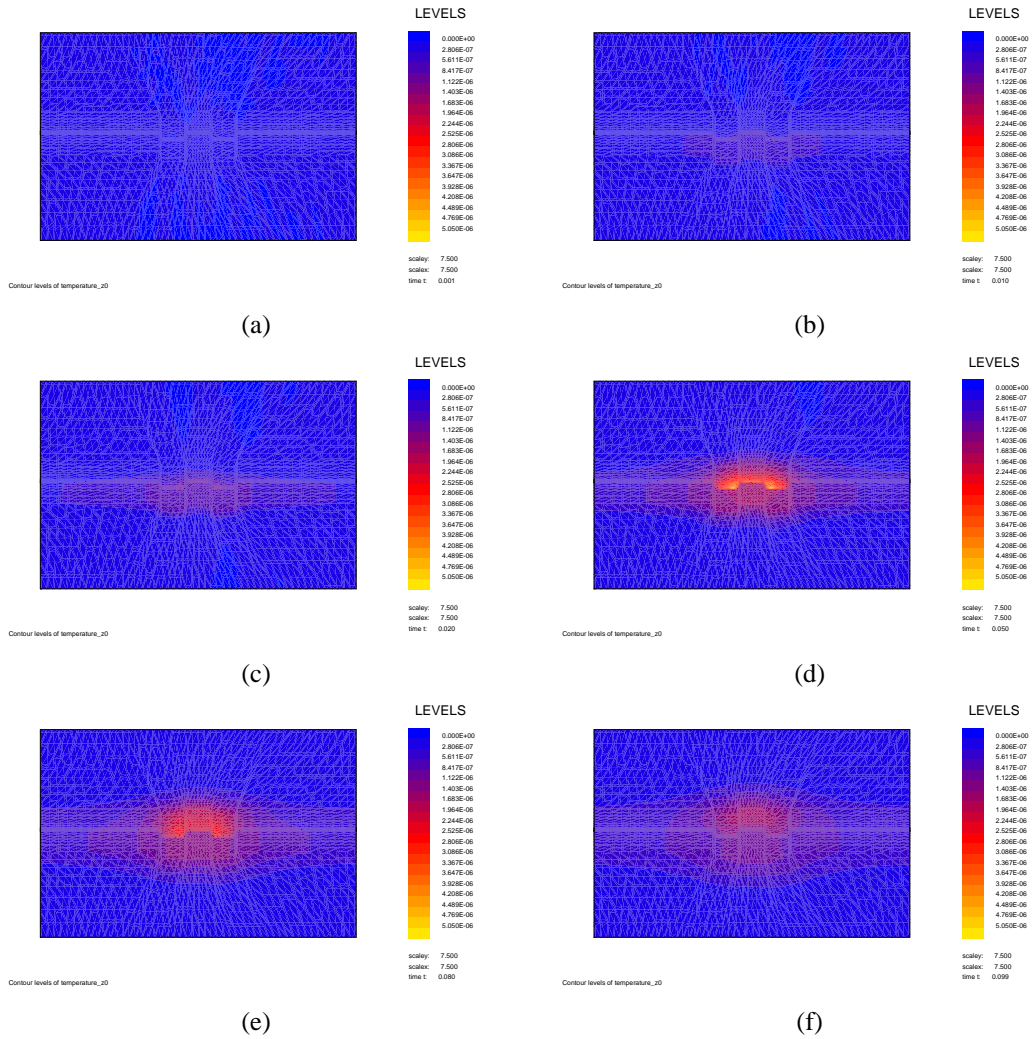


Figure 10.36: Contour plots of the temperature distribution in a plane  $y = \text{constant}$  through the middle of the computational box at  $t = 1 \text{ ns}$  (a),  $t = 10 \text{ ns}$  (b),  $t = 20 \text{ ns}$  (c),  $t = 50 \text{ ns}$  (d),  $t = 80 \text{ ns}$  (e) and  $t = 99 \text{ ns}$  (f). The spot is predominantly TE-polarized and moves at a speed of  $9.48 \text{ m/s}$ .

# Chapter 11

## Conclusions and recommendations

As a result of the study that has been described in the previous chapters, we can draw the following conclusions.

About the Cyclop program:

- In case the geometry in the unit cell consists of flat homogeneous regions with interfaces parallel to the  $(x,y)$ -plane, an analytical solution of the BVP can be calculated. In Cyclop the parameter *nelements* in the input file determines the fineness of the finite element mesh of the unit cell. The convergence of the numerical solution to the analytical solution is quadratical in the parameter *nelements*.
- The extension of the Cyclop solution from the two-dimensional unit cell to a larger three-dimensional region that is of interest for the thermal model has been successfully implemented. These extended field quantities are visualized in Amira.

About the integration of Cyclop and the thermal model:

- The mapping of the extended absorbed energy as computed by Cyclop to the three-dimensional thermal mesh is completed.
- The integrated thermal model has been validated for a normalized right-hand circular polarized spot that was focused on the center of the thermal computational box containing a planar geometry, by comparing the values of the temperature distribution at  $t = 1 \text{ ns}$  and at  $t = 10 \text{ ns}$  with values computed by Media. At  $t = 1 \text{ ns}$  the results of both models matched. The results at  $t = 10 \text{ ns}$  turned out to be slightly different, for which no explanation has been found so far.
- The integrated codes can be used as a tool to accurately simulate and research the following phenomena:
  - The effects of the polarization of the laser spot.
  - The effects of the spot size and the spot shape.
  - The differences between land-recording and groove-recording.
  - The effects of variation of the track pitch, the groove depth, the groove angle and the groove geometry.
  - The effects of varying the thermal and optical properties of the materials.

The results of such simulations will give insight in the optimization of groove geometry, stack design and the effects of for instance optical and thermal cross-track cross talk.

Recommendations for further research:

- In order to find an explanation for the differences in the temperature distribution at  $t > 1 \text{ ns}$  between the integrated thermal model and the Media program, further tests are needed.
- The geometries that were used for testing the Cyclop extension and the integrated thermal model are similar but in fact not identical to existing recording stacks. It will be useful to run simulations for existing geometries such that the numerical results can be compared with measured values.
- The modified Cyclop program, the integrated thermal model and the newly developed Cyclop post-processor Cycpost need to be made more robust. Furthermore, a user friendly interface should be developed. The alternative preprocessor should be further improved and will probably make the current Bicycle obsolete.

# Bibliography

- [1] Brok, J.M., and H.P. Urbach, *Vector diffraction on DVD disks*, Philips Research Laboratories, Eindhoven, the Netherlands, November 13, 2001.
- [2] Carriere, J., R. Narayan, W. Yeh, C. Peng, P. Khulbe, L. Li, R. Anderson, J. Choi and M. Mansuripur, *Principles of optical disk storage*, in: Progress in optics, volume 41 (editor: E. Wolf), Elsevier Science B.V., 2000.
- [3] Dekker, M.J., N. Pfeffer, M. Kuijper, I.P.D. Ubbens, W.M.J. Coene, E.R. Meinders and H.J. Borg, Proc. SPIE 4090, 28, 2000.
- [4] Feynman, R.P., R.B. Leighton and M. Sands, *The Feynmann lectures of physics, volume II*, Addison-Wesley, Reading, MA, 1964.
- [5] Goodman, J.W., *Introduction to Fourier optics*, second edition, McGraw-Hill, New York, 1998.
- [6] Hecht, E., *Optics, Third Edition*, Addison Wesley Longman, Inc. United States, 1998.
- [7] Mansuripur, M., G.A.N. Connell and J.W. Goodman, in: Applied Optics 21, 1106, 1982.
- [8] Mansuripur, M. and G.A.N. Connell, in: Applied Optics 22, 666, 1983.
- [9] Marcuse, D., *Theory of dielectric optical waveguides*, Academic press, 1991.
- [10] Meinders, E.R., H.J. Borg, H.R. Lankhorst, J.Hellmig and A.V.Mijiritskii, *Numerical simulation of mark formation in dual-stack phase-change recording*, in: Jpn. Journal of applied physics, volume 91, number 12, American Institute of Physics, 15 June 2002.
- [11] Meinders, E.R. et al. The FEM model....
- [12] Merkx, R.T.M., *Cyclop reference guide*, Nat. Lab. Technical Note Nr. 191/94, Eindhoven, the Netherlands.
- [13] Merkx, R.T.M., *Bicycle - a Cyclop pre-processor*, Nat. Lab. Technical Note Nr. 196/94, Eindhoven, the Netherlands.
- [14] Merkx, R.T.M., *Finite element implementation of electromagnetic plane wave diffraction at gratings for arbitrary angles of incidence*, Nat. Lab. Technical Note 161/93, Eindhoven, the Netherlands.
- [15] Merkx, R.T.M., and H.P. Urbach, *Finite element implementation of electromagnetic plane wave diffraction at gratings for arbitrary angles of incidence*, in: Mathematical and numerical aspects of wave propagation phenomena, SIAM, 1991.
- [16] Miyagawa, N., Y. Gotoh, E. Ohno, K. Nishiuchi and N. Akahira, Jpn. Journal of Applied Physics, Part 1 38, 5324, 1993.

- [17] Peng, C., and M. Mansuripur, *Thermal cross-track cross talk in phase-change optical disk data storage*, in: *Journal of Applied Physics*, volume 88, number 3, American Institute of Physics, August 1, 2000.
- [18] Petit, R., *Electromagnetic Theory of Gratings*, Springer-Verlag, Berlin, Heidelberg, New York, 1980.
- [19] Reitz, J., F. Milford and R. Christy, *Foundations of electromagnetic theory, Fourth Edition*. Addison-Wesley Publishing Company, Inc., United States of America, 1993.
- [20] Urbach, H.P., *Theoretical Optics*, Technische Universiteit Delft, Delft, 2002
- [21] H.P. Urbach, *On electromagnetic resonances in gratings*, ECCOMAS Computational Fluid Dynamics 2001, on CDROM.
- [22] H.P. Urbach, *Convergence of the Galerkin method for two-dimensional electromagnetic problems*, *SIAM J. Numer. Anal.*, **28**, No. 3 (1991), 697-710.
- [23] *Amira, Advanced visualization, data analysis and geometry reconstruction, User's guide and reference manual*, TGS Template Graphics Software, Inc., USA, 2000.
- [24] *Guide to Program DIFFRACT (7.7), Optical System Simulation Software from MM Research, Inc.*, MM Research, Inc., February 1998.
- [25] *Sepran reference guide*, 2002.
- [26] *User Manual for MEDIA (Version 1.0)*, November 27, 2000.



Thursday, July 11, 2002 at 4:04 pm



**Author(s)** J.H. Brusche

**Title** The integration of an optical and a thermal model for applications in optical recording

**Distribution**

Nat.Lab./PI	WB-5
PRB	Briarcliff Manor, USA
LEP	Limeil-Brévannes, France
PFL	Aachen, BRD
CIP	WAH

Director:	ing. F.M. Boekhorst	WY21
Department Head:	ir. C.J.L. van Driel	WY83

**Full report**

H.P. Urbach (10x)	Nat.Lab.	WY-81
J.H. Brusche (5x)	Nat.Lab.	WY-82
A.J.E. Janssen	Nat.Lab.	WY-81
T.J.J. Denteneer	Nat.Lab.	WY-81
W.J.J. Rey	Nat.Lab.	WY-81
H.D.L. Hollmann	Nat.Lab.	WY-81
J.A.C. Veerman	Nat.Lab.	WY-81
J.J. Rusch	Nat.Lab.	WY-82
E.R. Meinders	Nat.Lab.	WDC-01
J.A.C. Veerman	Nat.Lab.	WY-81
J.E. Schrader	Nat.Lab.	WY-82
D.J.H.C. Maas	Nat.Lab.	WY-71
M. Staring	Nat.Lab.	WY-71
S.M. Schimmel	Nat.Lab.	WY-71